MICRO-PATTERNED INTERFACES AFFECTING TRANSPORT THROUGH AND ALONG MEMBRANES

Ik hoor en vergeet
Ik zie en onthoud
Ik doe en begrijp

(Chinese zegswijze uit het Twents Techniek Museum HEIM)

Leden promotiecommissie

Prof. dr. G. van der Steenhoven (Voorzitter)	Universiteit Twente
Prof. dr.-ing. M. Wessling (Promotor)	Universiteit Twente
Dr. ir. R.G.H. Lammertink (Assistent-promotor)	Universiteit Twente
Prof. dr. D. Lohse	Universiteit Twente
Dr. ir. M. van Sint Annaland	Universiteit Twente
Prof. E.L. Cussler, Ph.D., M.S., B.E.	University of Minnesota
Prof. dr. ir. J.C. Schouten	Technische Universiteit Eindhoven
Dr. M. Crego-Calama	Stichting IMEC-NL / Holst Centre

Het onderzoek beschreven in dit proefschrift is uitgevoerd als speerpunt project in de vakgroep Membraan Technologie van de Universiteit Twente.

Micro-patterned interfaces affecting transport through and along membranes
Alisia M. Peters
Proefschrift, Universiteit Twente, Nederland
ISBN: 978-90-365-2758-3

Drukkerij: Gildeprint, Enschede, Nederland
Omslag: Dog Lake, Canada (2007).
Opgedragen aan: grandpa John, grandma Pat, opa Fons en oma Anna.

MICRO-PATTERNED INTERFACES AFFECTING TRANSPORT THROUGH AND ALONG MEMBRANES

PROEFSCHRIFT

ter verkrijging van
de graad van doctor aan de Universiteit Twente,
op gezag van de rector magnificus,
prof. dr. H. Brinksma,
volgens besluit van het College voor Promoties
in het openbaar te verdedigen
op vrijdag 9 januari 2009 om 15.00 uur

door

Alisia Mariska Peters

geboren op 5 augustus 1980
te Apeldoorn

Dit proefschrift is goedgekeurd door de promotor

Prof. dr.-ing M. Wessling

en de assistent promotor

Dr. ir. R.G.H. Lammertink

Table of contents

Summary

The central theme of the research described in this thesis is “micro-patterned interfaces”. The chapters provide experimental, numerical and theoretical results, which expand the present insights in mass transport processes through and along micro-patterned interfaces. The thesis also tries to provide the reader with a broader scope for future incorporation of micro-patterns in various membrane applications.

Besides a short general introduction of the thesis (chapter 1), a review chapter (chapter 2) provides background knowledge and highlights the current status of the research topics. Different patterning techniques are described, including the technique that is used to prepare the polymer films for this research. Micro-patterns can be easily replicated in polymer films using etched silicon substrates in combination with the casting technique developed in our group. A single silicon mold can generate multiple patterned replicas with precisely copied features. The preparation method can also tune the microscopic roughness of the surface. Dense polymer films have smooth interfaces, while porous polymer films have rough interfaces. Different patterns and the presence of a surface roughness lead to different wetting properties. Wetting phenomena and control of the wetting behavior are extensively discussed. A large amount of fundamental research has already been performed on the wetted states of micro-patterned films and on its practical applications in microfluidic devices. Membranes have also been patterned, mainly for flux enhancement via an increase in surface area. Some suggestions were made in literature that slip effects can enhance mass transport through membranes significantly. Membrane processes, polymeric membrane fabrication and concentration polarization are the final topics in the review chapter.

In the gas permeation experiments described in chapter 3, flat PDMS membranes have been replaced by (single-sided) micro-patterned membranes. The results of membranes with a line pattern on the feed side are compared to flat membranes with the same polymer volumes. Several researchers have reported the flux increase through patterned membranes as a result of surface area increase. Here, it is shown that the diffusion paths are also affected by micro-patterns, which can enhance mass transfer through the membrane even more. Compared to a flat sheet membrane with the same polymer volume, a pattern generates thicker and thinner cross-sectional areas and additional interfaces. These geometrical alterations cause lateral diffusion paths through the thicker parts of the membrane.

The experimental flux is enhanced up to 59% for a micro-patterned membrane with a 50% larger surface area compared to a flat membrane. To confirm the experimental results, they were compared with a simple analytical solution without lateral diffusion and with finite element simulations with lateral diffusion. Uniaxial calculations generate significantly lower flux enhancements compared to the experiments, whereas incorporation of lateral diffusion paths via simulations results in similar values.
During preparation it was noticed that the membranes with a micro-pattern could be handled easily, even if the thinnest cross-sectional thicknesses were only 5 µm. Flat films with this thickness tore easily upon handling. Tensile measurements have been performed to determine the strength of micro-patterned membranes. A tensile stress decrease of 28% for line patterned membranes under longitudinal strain is measured, although the origin of the decrease is not clear.
In commercial composite membranes, the thickness of the separating layer has to be very thin. With the casting method it is practically not possible to fabricate micro-patterned films that thin. It is interesting, though, to compare micro-patterned membranes with composite membranes. The similarity that they have is the geometry of a permeation layer and a support layer, but the advantage of the micro-patterned membrane is that its support layer is also permeable. Simulations show that a micro-pattern can generate higher fluxes if comparable dimensions are chosen for the composite material. Micro-patterning standard gas permeation membranes has lead to different insights of mass transfer in diffusion driven processes, which may lead to various membrane geometries in future.

Flux through a membrane is also largely influenced by transport to its interface. A micro-pattern can lead to a different interaction of a liquid with a solid, e.g. a hydrophobic material becomes more hydrophobic by patterning. Liquid drops can create a composite interface by partly floating on air pockets between the pattern (Cassie-Baxter state) or the liquid can fill the volume between the pattern and wet the complete solid surface (Wenzel state).
When the energy barrier between the Cassie-Baxter state and the Wenzel state is overcome, a transition from a composite to a wetted interface occurs. Experiments and numerical simulations have shown that the geometry and the material of the micro-pattern influence the wetting dynamics during this transition (chapter 4). Micro-patterned films with square micro-pillars in a square array are prepared from two different polymers. Various gap sizes between the pillars and pillar heights were investigated. The transition is viewed from the bottom with an inverted microscope and the velocity of the wetting liquid is determined through high-speed imaging. The results are compared to lattice Boltzmann simula-

tions. When the pillars are too close together the liquid does not spread and a stable Cassie-Baxter state is maintained. After passing a critical point the transition takes place. This critical point is determined by geometry (pillar height and gap size between the pillars) and material properties (intrinsic contact angle). The front velocity of the liquid during the transition increases with increasing gap size and decreasing hydrophobicity and pillar height. The shape of the wetted area is also influenced by these parameters. When the front velocity is slow (near the critical point), the fast lateral movement of the liquid fills the row, before the liquid advances to the next (zipping motion). This causes a square-shaped wetted area.
All these conclusions are backed-up by theoretical equations in chapter 5. Energy balances determine the critical point for the transition and also confirm the critical slowing down of the liquid around this critical point. Scaling arguments are derived to be able to predict the front velocity for micro-patterned films with different geometries or material properties. The experimental results scale nicely with the relationship derived for the zipping regime. These findings can be used to tune the velocity and even direction of the liquid during a Cassie-Baxter state to Wenzel state transition.

The usefulness of control over the Cassie-Baxter state is explained in chapter 6, when the experiments in a microfluidic channel show that slip conditions are generated at the liquid-gas interface. Velocity profiles above micro-patterned surfaces are determined with micro-particle image velocimetry. Micro-grooves with three different widths and created in two different polymers (dense PDMS and porous PVDF) are examined. Near the patterned surface, the velocity is clearly higher above the liquid-gas interface than above the liquid-solid interface. At larger distances from the patterned surface, this difference disappears.
The flow velocity is determined at different heights in the micro-channel to obtain the velocity profile and from that a slip length. Two methods are used to determine the slip length: plotting the velocities above the center of a groove (locally) and for a unit cell with one groove and one line (globally). The local slip lengths are higher than the global slip lengths as the liquid above the solid surface experiences a no-slip boundary. In both cases the slip length increases with increasing liquid-gas interface. More hydrophobic materials and additional surface roughness also increase the slip length.
The resulting velocity profiles are compared with an analytical approach to determine the impact of slip on concentration polarization at a membrane surface. According to literature, a slip coefficient of 0.05 should decrease the boundary layer thickness by a factor 2. Some of the slip lengths in this chapter are large enough to meet this number, which shows that

these patterns could affect concentration polarization at membrane surfaces. Processes like pervaporation could therefore benefit from micro-patterns.

To conclude this thesis the main results are summed up in chapter 7 and an outlook is provided for future applications of micro-patterned interfaces. The suggestions are especially focused on other diffusion driven processes and hydrodynamic applications. Food packaging, clothing, microfluidics, gas-liquid contactors and bioanalytical research are a few areas, which can definitely benefit from the research described in this thesis. A major concern for many applications still is the long-term stability of the Cassie-Baxter state.

This thesis provides the reader with the possibilities and drawbacks of micro-patterned interfaces for several membrane and non-membrane related topics. Hopefully it will inspire to new applications in a wide variety of (research) fields.

Samenvatting

Het hoofdthema van het onderzoek beschreven in dit proefschrift is “micro-gestructureerde oppervlakken”. De hoofdstukken geven experimentele, numerieke en theoretische resultaten, die de huidige inzichten op het gebied van massatransport door en langs micro-gestructureerde oppervlakken aanvullen. Het proefschrift probeert de lezer tevens een bredere kijk te geven op het toekomstige gebruik van micro-structuren in verschillende membraan toepassingen.

Na een korte algemene introductie van het proefschrift (hoofdstuk 1) beschrijft een overzichtshoofdstuk (hoofdstuk 2) achtergrondkennis en benadrukt het de huidige status van de onderzoeksonderwerpen. Verschillende structureringstechnieken, inclusief de techniek die gebruikt is om de polymere films te bereiden voor dit onderzoek, zijn beschreven. Micro-structuren kunnen gemakkelijk worden gerepliceerd in polymere films met behulp van geëtste silicium substraten in combinatie met de strijktechniek die in onze groep is ontwikkeld. Met een enkele silicium mal kunnen meerdere gestructureerde films geproduceerd worden met nauwkeurig gekopieerde karakteristieken. Met de bereidings-methode kan tevens de microscopische ruwheid van het oppervlak bepaald worden. Dichte polymere films hebben gladde oppervlakken, terwijl poreuze polymere films ruwe oppervlakken hebben. Verschillende patronen en de aanwezigheid van een oppervlakte-ruwheid leidt tot verschillende bevochtigingseigenschappen. Bevochtigingsfenomenen en controle over het bevochtigingsgedrag zijn uitgebreid bediscussiëerd. Een grote hoeveelheid fundamenteel onderzoek naar de bevochtiging van micro-gestructureerde films en de praktische toepassingen in microfluïdische instrumenten heeft al plaats-gevonden. Ook gestructureerde membranen zijn al beschreven, voornamelijk voor verhoging van de flux door een vergroting van het oppervlak. In de literatuur wordt gesuggereerd dat slipeffecten massatransport door membranen significant kunnen vergroten. Membraanprocessen, bereidingswijzen van polymere membranen en concentratiepolarisatie zijn de laatste onderwerpen in het overzichtshoofdstuk.

In de gaspermeatie experimenten beschreven in hoofdstuk 3 zijn vlakke PDMS membranen vervangen door (enkelzijdig) micro-gestructureerde membranen. De resultaten van de membranen met een lijnenpatroon aan de voedingskant zijn vergeleken met die van vlakke membranen met hetzelfde polymeervolume. Verscheidene onderzoekers hebben de fluxverhoging door gestructureerde membranen toegeschreven

aan de oppervlaktevergroting. Hier wordt aangetoond dat micro-structuren ook de diffusiepaden beïnvloeden, waardoor het massatransport door membranen nog meer verhoogd kan worden. Vergeleken met een vlak membraan met hetzelfde polymeervolume genereert een patroon dikkere en dunnere dwarsdoorsnedes en additionele oppervlakken. Deze geometrische veranderingen zorgen voor laterale diffusiepaden door de dikkere delen van het membraan. Vergeleken met een vlak membraan is de experimentele flux voor een micro-gestructureerd membraan met een 50% groter oppervlak verhoogd tot 59%. Om de experimentele resultaten te valideren zijn ze vergeleken met een simpele analytische oplossing zonder laterale diffusie en met eindige elementen simulaties met laterale diffusie. De uniaxiale berekeningen genereren significant lagere fluxverhogingen vergeleken met de experimenten, terwijl de toevoeging van laterale diffusiepaden via simulaties resulteren in soortgelijke waarden.
Tijdens de bereiding viel het op dat de membranen met een micro-structuur gemakkelijk gebruikt konden worden, zelfs als de dunste dwarsdoorsnede slechts 5 µm was. Vlakke films met deze dikte scheurden makkelijk tijdens gebruik. Er zijn trek-rek metingen gedaan om de sterkte van micro-gestructureerde membranen te bepalen. Voor de membranen met lijnen tijdens een longitudinale belasting werd een verlaging van de trekspanning van 28% gemeten, alhoewel de origine van de verlaging onbekend is.
De dikte van de scheidingslaag van commerciële composiet-membranen moet erg dun zijn. Met de strijktechniek is het praktisch niet mogelijk om micro-gestructureerde films van deze dikte te maken. Het is toch interessant om de micro-gestructureerde membranen met composiete membranen te vergelijken. De overeenkomst die zij hebben is de geometrie van een permeatie laag en een ondersteuningslaag, maar het voordeel van het micro-gestructureerde membraan is dat de ondersteuningslaag ook permeabel is. Simulaties tonen dat een micro-patroon een hogere flux kan genereren als vergelijkbare dimensies worden gekozen voor een composiet materiaal. Het micro-structureren van standaard gaspermeatie membranen heeft tot verschillende inzichten geleid met betrekking tot het massatransport tijdens diffusie-gedreven processen, die in de toekomst wellicht zullen leiden tot verschillende membraan geometriën.

Flux door een membraan wordt tevens grotendeels beïnvloed door transport naar zijn oppervlak. Een micro-patroon kan leiden tot een andere interactie van een vloeistof met een vaste stof, bijvoorbeeld een hydrofoob materiaal dat meer hydrofoob wordt door structurering. Vloeistof-druppels kunnen een composiet raakvlak creëren door deels op de lucht tussen de structuren te rusten (Cassie-Baxter toestand) of de vloeistof kan de ruimte

tussen de structuren vullen en het complete vaste oppervlak bevochtigen (Wenzel toestand).

Wanneer de energiebarrière tussen de Cassie-Baxter toestand en de Wenzel toestand wordt overwonnen, vindt een overgang van een composiet naar een bevochtigd raakvlak plaats. Experimenten en numerieke simulaties hebben aangetoond dat de geometrie en het materiaal van het micro-patroon de bevochtingingsdynamiek tijdens deze overgang beïnvloeden (hoofdstuk 4). Micro-gestructureerde films met vierkante micro-pilaren in een vierkante matrix zijn bereid van twee verschillende polymeren. Verschillende afstanden tussen de pilaren en pilaarhoogtes zijn onderzocht. De overgang is van onderaf bekeken met een omgekeerde microscoop en de snelheid van de bevochtigende vloeistof is bepaald door hoge snelheidsopnames. De resultaten zijn vergeleken met rooster Boltzmann simulaties. Wanneer de pilaren te dicht bij elkaar staan, spreidt de vloeistof niet en wordt een stabiele Cassie-Baxter toestand behouden. De overgang vindt plaats na het passeren van een kritisch punt. Dit kritische punt wordt bepaald door geometrie (pilaarhoogte en ruimte tussen de pilaren) en materiaal eigenschappen (intrinsieke contacthoek). De snelheid van het front van de vloeistof tijdens de overgang wordt hoger met grotere ruimtes en lagere hydrofobiciteit en pilaarhoogte. De vorm van het bevochtigde opperblak wordt ook beïnvloed door deze parameters. Wanneer de front snelheid laag is (vlak bij het kritische punt) vult een snelle laterale beweging van de vloeistof de rij voordat de vloeistof de volgende rij bereikt (“zipping” beweging). Dit veroorzaakt een vierkant bevochtigd oppervlak.

Al deze conclusies worden onderbouwd door theoretische vergelijkingen in hoofdstuk 5. Energiebalansen bepalen het kritische punt voor de overgang en bevestigen ook de kritische vertraging van de vloeistof rond het kritische punt. Om de frontsnelheid voor micro-gestructureerde films met verschillende geometriën of materiaaleigenschappen te kunnen voorspellen, zijn schalingsargumenten afgeleid. De experimentele resultaten schalen goed met de vergelijking, die afgeleid is voor het “zipping” regime. Deze bevindingen kunnen worden gebruikt om de snelheid en zelfs richting van de vloeistof tijdens een overgang van een Cassie-Baxter toestand naar een Wenzel toestand te bepalen.

De bruikbaarheid van controle over de Cassie-Baxter toestand wordt uitgelegd in hoofdstuk 6, wanneer de experimenten in een microfluïdisch kanaal aantonen dat slip-condities bestaan boven het vloeistof-gas raakvlak. Snelheidsprofielen boven micro-gestructureerde oppervlakken zijn bepaald met “micro-particle image velocimetry”. Er is

onderzoek gedaan naar micro-groeven met drie verschillende breedtes en twee verschillende polymeren (dicht PDMS en poreus PVDF). In de nabijheid van het gestructureerde oppervlak is de snelheid boven het vloeistof-gas raakvlak duidelijk hoger dan boven het vloeistof-vast raakvlak. Op grotere afstanden van het gestructureerde oppervlak verdwijnt dit verschil.
De doorstroomsnelheid werd bepaald op verschillende hoogtes in het micro-kanaal om de snelheidsprofielen te verkijgen en daaruit de sliplengte te halen. Twee methoden zijn gebruikt om de sliplengte te bepalen: het uitzetten van de snelheden boven het midden van een groef (lokaal) en voor een eenheidscel bestaande uit een groef en een lijn (globaal). De lokale sliplengtes zijn hoger dan de globale slip lengtes, omdat de vloeistof boven het vaste oppervlak een no-slip grenslaag ervaart. In beide gevallen wordt de sliplengte vergroot met een vergroot vloeistof-gas raakvlak. Hydrofober materiaal en extra oppervlakteruwheid vergroten ook de sliplengte.
De uiteindelijke snelheidsprofielen zijn vergeleken met een analytische methode om de impact van de slip op concentratiepolarisatie aan een membraan oppervlak te bepalen. Volgens de literatuur zou een slipcoëfficiënt van 0.05 de grenslaagdikte verminderen met een factor 2. Sommige sliplengtes in dit hoofdstuk zijn vergelijkbaar met dit getal, wat laat zien dat deze patronen de concentratiepolarisatie aan membraan oppervlakken kunnen beïnvloeden. Processen zoals pervaporatie kunnen daarom profiteren van micro-patronen.

Om dit proefschift af te sluiten zijn in hoofdstuk 7 de belangrijkste resultaten opgesomd en wordt een perspectief geboden voor toekomstige toepassingen van micro-gestructureerde oppervlakken. De suggesties zijn speciaal gefocussed op andere diffusie-gedreven processen en hydrodynamische toepassingen. Voedselverpakkingen, kleding, microfluïdica, gas-vloeistof contactoren en bioanalytisch onderzoek zijn een aantal gebieden die zeker kunnen profiteren van het onderzoek dat beschreven is in dit proefschrift. Een groot aandachtspunt voor veel toepassingen is nog steeds de langetermijnstabiliteit van de Cassie-Baxter toestand.

Dit proefschrift voorziet de lezer van de mogelijkheden en schaduwzijdes van micro-gestructureerde oppervlakken voor verschillende membraan- en niet-membraan-gerelateerde onderwerpen. Hopelijk zal het inspireren tot nieuwe toepassingen in een grote verscheidenheid aan (onderzoeks)-gebieden.

Chapter 1

Introduction to this thesis

This chapter briefly introduces the scope of this thesis, leading to the overall research question. A short outline per chapter is given to highlight the content.

1.1 Scope and thesis outline

Materials science has often focused on the composition of a material rather than its surface. More than ever, researchers are embracing the idea that surface properties are as important as bulk properties. With present technology, interfacial processes, which are often limiting transport processes, can be investigated to the nano-scale. As a result of the research on these small length scales, various methods were developed to design and manufacture surface topography accurately [1-5]. Top-down approaches like lithographic techniques and etching can create the desired micro-pattern on a flat material precisely. Bottom-up techniques, such as self-assembly, are standard design tools as well nowadays. A couple of years ago, a single-step technique to micro-pattern dense and porous polymeric surfaces was developed in our laboratory [6,7]. The beauty of this replication technique is that it is able to generate many surfaces with micrometer sized features from a single mold. Micro-patterning is often seen as a way to increase surface area, but this thesis will show that a micro-patterned surface can lead to other advantages as well. The thesis aims to answer the following question:

How can mass transport through a polymeric membrane benefit from surface micro-patterning?

The experiments, theory and simulations in the following chapters combine two topics to answer this question: transport through and along micro-patterned membranes. A general introduction to these topics is given in **chapter 2**. It covers the basic knowledge and current status of patterning techniques, wetting issues, membrane processes and film preparation.

Chapter 3 describes the advantages of mass transfer through micro-patterned dense membranes compared to flat membranes with the same polymer volume. Gas permeation measurements were performed to characterize the transport and compared with simple analytical calculations of the flux and finite element simulations in COMSOL. Tensile stress measurements had to determine if the mechanical stability of the membranes was sufficient.

The interaction of a liquid with a solid surface is also affected by the presence of a micro-pattern. It can increase the water-solid contact area (Wenzel state), but also reduce it by creating a composite interface (Cassie-Baxter state). Micro-pattern geometry and material surface properties define which superhydrophobic state a liquid prefers. Two chapters are

devoted to fundamental research on the hydrodynamic behavior of liquid filling the volume between micro-pillars. The focus of **chapter 4** is on the experimental investigation of this Cassie-Baxter state to the Wenzel state transition. The liquid front is followed with a high speed camera and compared to lattice Boltzmann simulations. The theoretical background on this transition and scaling arguments for the resulting front velocities are described in **chapter 5**.

In **chapter 6** the research on hydrodynamics along a surface and transport through a membrane are combined. The slip properties of (porous) micro-patterned membranes are measured with micro-particle image velocimetry. The resulting velocity profiles are compared with an analytical approach to determine the impact of slip on concentration polarization at a membrane surface.

Chapter 7 gives the overall conclusions of this thesis and provides an outlook on the practical application of micro-patterning in other (membrane) processes. The suggestions for future work are especially focused on other diffusion driven processes, hydrodynamic applications and stability issues of the Cassie-Baxter state.

1.2 References

1. Becker, H.; Gartner, C. *Electrophoresis* **2000**, *21*, 12-26.
2. Becker, H.; Gartner, C. *Analytical and Bioanalytical Chemistry* **2008**, *390*, 89-111.
3. Li, X. M.; Reinhoudt, D.; Crego-Calama, M. *Chemical Society Reviews* **2007**, *36*, 1350-1368.
4. Li, X. M.; Reinhoudt, D.; Crego-Calama, M. *Chemical Society Reviews* **2007**, *36*, 1529-1529.
5. Roach, P.; Shirtcliffe, N. J.; Newton, M. I. *Soft Matter* **2008**, *4*, 224-240.
6. Vogelaar, L.; Barsema, J. N.; van Rijn, C. J. M.; Nijdam, W.; Wessling, M. *Advanced Materials* **2003**, *15*, 1385-+.
7. Vogelaar, L.; Lammertink, R. G. H.; Barsema, J. N.; Nijdam, W.; Bolhuis-Versteeg, L. A. M.; van Rijn, C. J. M.; Wessling, M. *Small* **2005**, *1*, 645-655.

Chapter 2

Patterning: design in membrane technology and fluid dynamic research

Surface modifications, either molecular or geometrical, are widely examined in literature to affect the fluid-solid interaction. One of the key words in wetting research at the moment is superhydrophobicity. There are numerous publications on the development of 'new' superhydrophobic surfaces for wetting and hydrodynamic purposes. Systematic research often uses well-defined surfaces with (geometrical) patterns. Properties as water repellency and slip make these surfaces industrially applicable in many ways. The work described in the next chapters of this thesis provides insight in the benefits of geometrically designed surfaces in membrane technology. As a general introduction, this chapter gives the basic principles of patterning, wetting (mainly focusing on the superhydrophobicity), membrane technology and polymers.

2.1 Introduction on patterning

All surfaces investigated in this thesis are designed with geometrical features. Polymeric materials can be easily molded into films with (micro-)pillars and (micro-)lines, from now on called patterns. The word 'pattern' is not a trivial choice. In literature, three synonyms are often used to describe designed surfaces: 'structured', 'patterned' or 'textured' surfaces. Although this terminology has been accepted in literature, the use of the words 'structured' and 'textured' for geometrically designed surfaces is less appropriate. In the Cambridge advanced learner's dictionary [1] their definitions (among others) are:

Structure, *noun*: the way in which the parts of a system or object are arranged or organized, or a system arranged in this way.
Pattern, *noun*: any regularly repeated arrangement, especially a design made from repeated lines, shapes or colors on a surface.
Texture, *noun*: the quality of something that can be decided by touch; the degree to which something is rough or smooth, or soft or hard.

In the context of geometrically designed surfaces, the word '(micro-)structure' could even be confusing as it is also used to depict the natural outline of a surface, such as porosity and pore size or bulk morphology [2-4]. Grafted surfaces are also called 'structured surfaces' [5,6].
Designing a specific surface can be done on a wide range of length scales. A few examples of frequently used design techniques [3,7-25] are listed in figure 1. Detailed descriptions of these and many more processes are given in a review by Geissler and Xia [26]. In a very recent publication, chemical (micro-scale) and geometrical (nano-scale) patterning techniques are used on one surface to create a mixed effect [27].

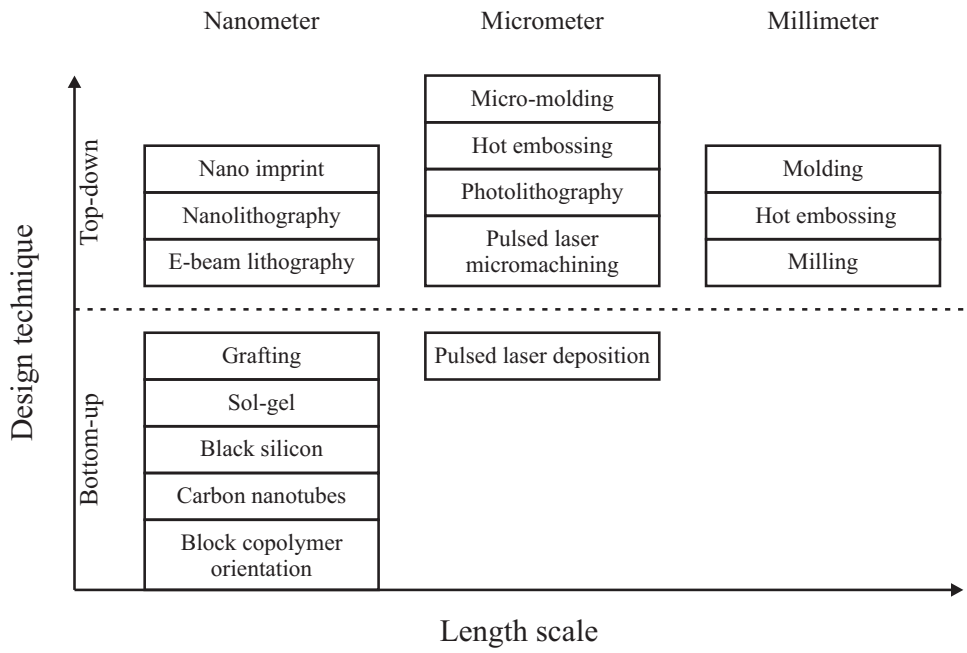

Figure 1. A few design techniques (split into bottom-up and top-down) arranged by length scale of the resulting pattern.

The surfaces for the research described in this thesis are prepared via a micro-patterning technique. The negative of the pattern is outlined with a lithographic technique and etched in a silicon wafer. This is used to prepare the patterned polymer films as in figure 2a. Apart from its good replicating reproducibility, a great feature of the micro-patterning technique is that it is applicable to many materials. As long as a material is solvable or a surface is moldable the technique can be applied. A black silicon surface with nano-scale roughness is shown in figure 2b. The polypropylene surface in figure 2c combines both scales as the features are micrometer size and with a nanometer size roughness. This film is a replication of a negative metal surface made with pulsed laser micromachining.

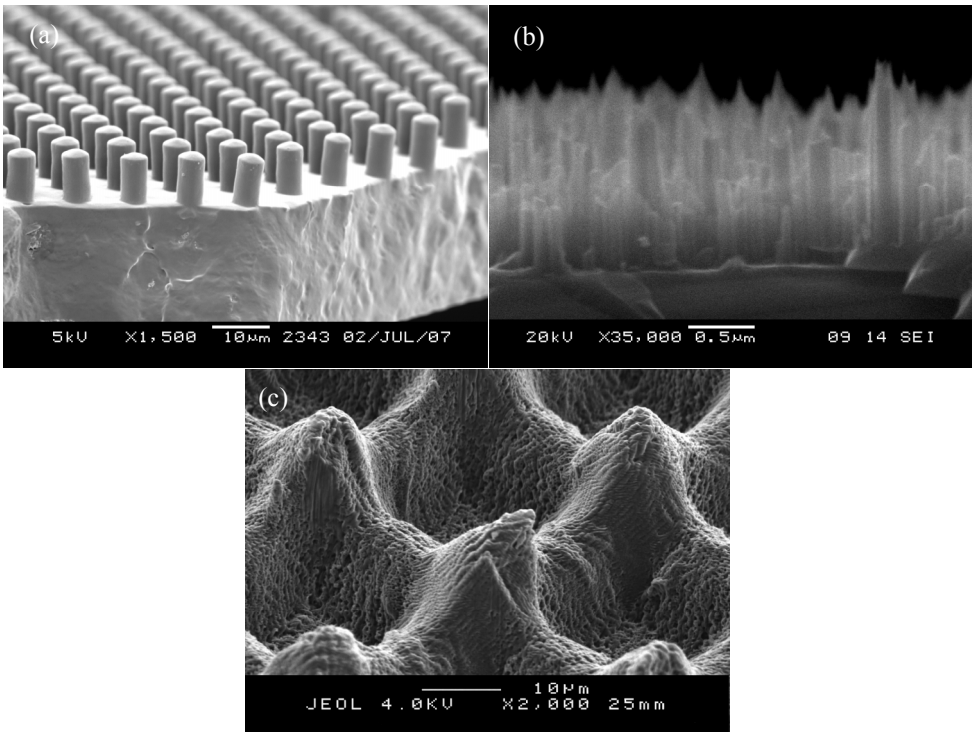

Figure 2. Scanning electron microscope pictures of three different superhydrophobic surfaces: (a) a micro-patterned polymer film, (b) a black silicon surface (kindly supplied by Bram Borkent) and (c) polypropylene replicated from a pulsed laser micromachined surface (kindly supplied by Max Groenendijk).

Nowadays, one of the main research topics dealing with micro-scale surface patterns is superhydrophobicity. As described more elaborately in paragraph 2.2.2, nature has some great surfaces to repel water and remove dirt. An artificially micro-patterned surface can mimic these features. Wetting conditions also have an impact on flow. To investigate issues such as slip and bouncing droplets, nano- and micro-patterned surfaces are used as well. This field is explored in paragraph 2.4. Two specific publications, one on membrane patterning on the macro-scale [25] and one on minimizing concentration polarization by creating slip [28], led to the belief that the field of membrane technology could benefit from the micro-patterning technique. Experiments to enhance gas permeation and transport via pervaporation are described in chapters 3 and 6. To introduce these chapters some basic knowledge of membrane technology and polymers is provided in paragraph 2.5.

2.2 Wetting phenomena

2.2.1 Hydrophilic and hydrophobic surfaces

Surfaces can be either hydrophilic or hydrophobic and in some cases even both. These terms can be quantified by the intrinsic contact angle θ, the angle between the liquid-solid interface and the liquid-gas interface. A hydrophilic surface has a contact angle of $0° < \theta < 90°$ (figure 3a), while a hydrophobic surface has higher contact angles $90° < \theta < 180°$ (figure 3b).

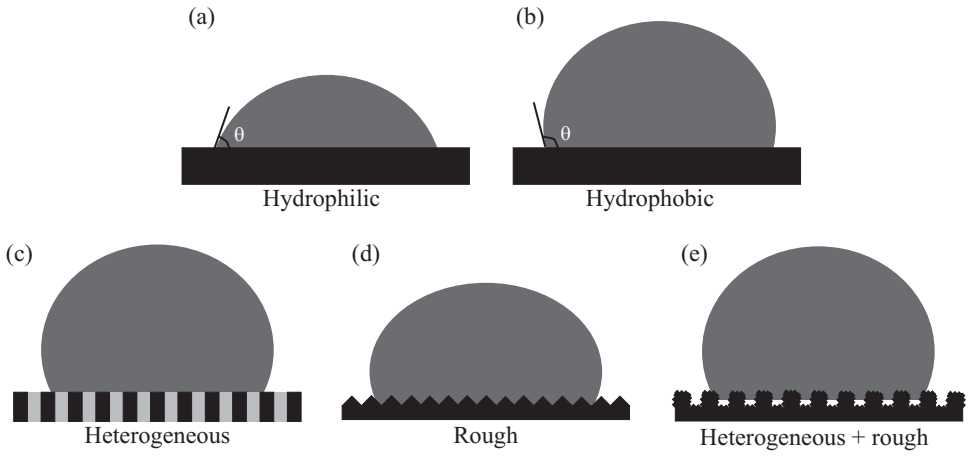

Figure 3. Liquid on: (a) a flat hydrophilic surface, (b) a flat hydrophobic surface, (c) a heterogeneous surface, (d) a rough surface and (e) a rough, heterogeneous surface.

The physical origin of the difference in wetting behavior is interfacial tensions [29]. Molecules attract one another and 'sense' the presence of other molecules around them. Compared to a liquid molecule in the bulk, a liquid molecule at an interface loses half of its cohesive interactions. This is the reason for liquids to adjust their shape to the smallest possible surface area. The interaction between two phases is expressed as the interfacial tension.

In the beginning of the 19th century Young discovered the relationship (equation 1) between the contact angle of a liquid on a flat and homogeneous material θ and the three interfacial tensions γ_{gs} (gas-solid), γ_{ls} (liquid-solid) and γ_{lg} (liquid-gas) [29]. The contact angle can also be measured directly at the three-phase line of a liquid drop on a solid surface.

$$\cos\theta = \frac{\gamma_{gs} - \gamma_{ls}}{\gamma_{lg}} \quad (1)$$

The basic ideas for describing the liquid behavior on composite or rough surfaces were later on posed by Wenzel [30] and Cassie and Baxter [31]. When liquid is deposited on a heterogeneous surface (figure 3c), the intrinsic contact angle of both materials influences the so called apparent contact angle θ^*. The contact fractions f_1 and f_2 determine the weight of both material properties θ_1 and θ_2 in the final contact angle (the Cassie-Baxter equation 2).

$$\cos\theta^* = f_1 \cos\theta_1 + f_2 \cos\theta_2 \quad (2)$$

This equation yields θ^* as a value in between the intrinsic contact angles of two materials. A special example is when one of the 'materials' is air as the liquid starts bridging the gaps left by the solid material. In this case equation 2 can be simplified into equation 3 by substituting the following properties: the liquid-air contact angle θ_2 is 180°, the liquid-solid contact angle θ_1 is written as the intrinsic contact angle θ, the fractions f_1 and f_2 add up to 1 with f_1 now as the fraction of solid in contact with the liquid φ_s.

$$\cos\theta^* = \varphi_s \cos\theta + \varphi_s - 1 \quad (3)$$

Surface roughness also affects the contact angle (figure 3d). The apparent contact angle can be calculated by multiplying the intrinsic contact angle with a roughness factor r (the Wenzel equation 4).

$$\cos\theta^* = r\cos\theta \quad (4)$$

with $r > 1$ as it is defined as the ratio of the true solid surface area to its projected surface area. This way, a hydrophilic material will become more hydrophilic if the surface is rough, whereas a hydrophobic material will become more hydrophobic.
In special cases, e.g. for a heterogeneous surface that is also rough (figure 3e), equations 3 and 4 can be combined to describe the wetting. The liquid is still floating on air pockets, but can wet more surface area than on a flat surface. Marmur describes that this behavior can also happen on surfaces with a single roughness as long as the liquid is only partly

wetting the vertical walls [32]. The contact angle of a liquid drop on such surfaces is described by equation 5 [32,33].

$$\cos\theta^* = \varphi_s r \cos\theta + \varphi_s - 1 \quad (5)$$

A special class within the field of tunable surfaces is the switchable materials [34]. They have the ability to switch between a hydrophilic and a hydrophobic surface. Several oxides change their wetting properties under (UV) light [35]. With a change of temperature, switchable polymers change conformation, leading to major differences in wettability [36,37].

2.2.2 Superhydrophobicity

The contact angle for any liquid-solid combination can run from 0° to 180°. The wetting extremes are called superhydrophilicity ($\theta \sim 0°$) and superhydrophobicity ($150° < \theta < 180°$). In the first case the liquid spreads as a thin layer across the surface. In this thesis, the focus is on superhydrophobic surfaces on which liquid barely touches the surface.

Already early on in the 20th century a highly water repelling surface was reported in literature with the remark that water deposited on lycopodium (powdery spores of a club moss) “rolls itself up into perfect little balls” [38]. Still, most insight on the origin of this behavior was gained 20 years ago. Botanists Barthlott and Neinhuis investigated many plant surfaces [39-41] and discovered that an extremely rough surface covered with wax is the key to their water repellency. This, together with the research on fractal surfaces by Onda et al. in 1996 [42], led to an explosion of publications on hydrophobic surfaces. One specific publication about the self-cleaning mechanism of the lotus leaf set an example as the superhydrophobic phenomenon was named the ‘lotus effect™, [43].

The term, recently registered as a trade mark [44,45], describes a state in which a liquid is partly in contact with air and partly with the solid of a rough or micro-patterned solids surface. The static contact angle for this Cassie-Baxter state (equation 3 and figure 4a) is high and in most cases the contact angle hysteresis for a dynamic drop (definition in paragraph 2.3.2) is low. These features make it possible for a droplet to easily roll off a surface and even take dirt along in the process (self-cleaning). There are many practical applications for artificial surfaces containing these water repelling qualities. It can be used to waterproof textiles [46] or create water-diverting surfaces for clear views through glass, drop-free solar collectors or anti-icing and anti-corrosive purposes [44,45].

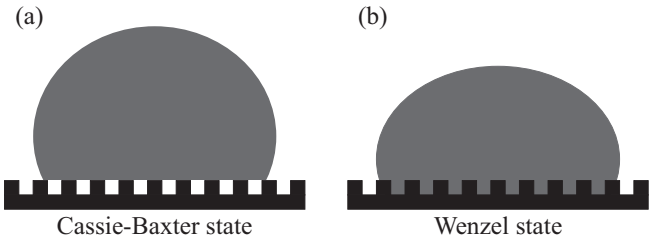

Figure 4. (a) Cassie-Baxter state. (b) Wenzel state.

2.2.3 Cassie-Baxter to Wenzel transition

The Cassie-Baxter state is not a stable state in all cases. Under certain conditions, liquid could replace the air and come in contact with the complete surface (the Wenzel state, equation 4 and figure 4b). Theoretical research has determined the height of the energy barrier of this transition from a local energy minimum to the global minimum. A sketch of the energy barrier for the Cassie-Baxter state to Wenzel state transition is given in figure 5. During this transition the observed contact angle is lowered. The resistance for the transition depends on the intrinsic contact angle of a material and the distance between and shape of the features [33]. For a regular micro-pillar pattern the barrier is also directly proportional to the height of the pillar as this distance defines the difference in wetted area between the two states [47]. Many experimental reports have proven as well that design of geometrical parameters and material properties can influence the superhydrophobic state (paragraph 2.2.4). Electric fields can induce the transition as well by switching the liquid surface tension (electrowetting) [48,49].

The reverse transition (from Wenzel to Cassie-Baxter) has only been observed in situations where the liquid is first forced into the Wenzel state: examples are bouncing droplets [50] and condensation [51].

2.2.4 Review articles on superhydrophobicity

As the number of publications on the superhydrophobic phenomenon is so large, mentioning the main reviews in each category would do more justice to this chapter than listing publications individually. The basic principles of superhydrophobicity are extensively discussed in a book chapter [29]. Most review articles describe the mechanisms of the lotus effect™ and the preparation of superhydrophobic surfaces [33,52-61]. They may overlap in content, but also give their individual perspective on topics such as disordered hydrophobic materials [53], bioinspired surfaces [55,56,62] and switchable materials [55,56,58]. The

theoretical aspects of superhydrophobicity are often briefly discussed in articles, but mainly highlighted in books [29,63].

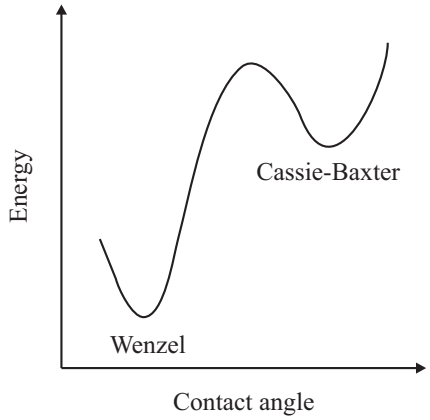

Figure 5. Sketch of the energies involved in the superhydrophobic Cassie-Baxter state to Wenzel state transition.

2.3 Terminology

2.3.1 Hydro or hygro?

As Marmur posed recently [64], the terms hydrophilic and hydrophobic are not comprehending the complete research on wetting properties. These words only describe the interaction of water (from the Greek *hydro*) with a solid. The behavior of other liquids like solvents and oils on solids is also investigated [65-68]. These researchers use the terms solvophilic / solvophobic and oleophilic / oleophobic surfaces. To biomedical engineers the interaction between solid surfaces and cells or proteins is also a topic of interest [69,70]. To generalize the discussion, Marmur states that these terms could be replaced by hygrophilic and hygrophobic as *hygro* means liquid in Greek. Although this change in terminology does justice to the topic, the word (super)hydrophobic is still appropriate in this thesis as water is the only liquid used.

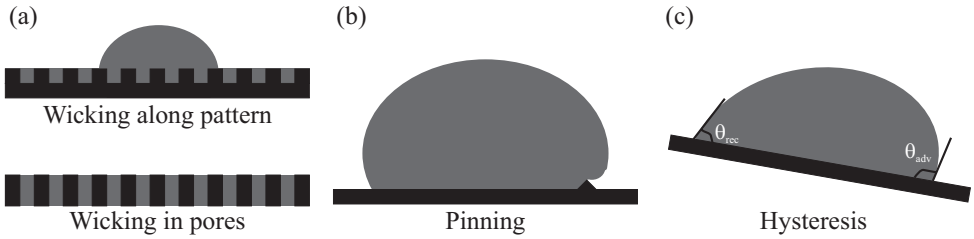

F**igure 6.** (a) Wicking (in pores and along a pattern). (b) Pinning. (c) Contact angle hysteresis.

2.3.2 Wicking, pinning and contact angle hysteresis

Many authors also discuss phenomena such as wicking, pinning and contact angle hysteresis [33,71,72]. Although this thesis does not cover these topics, a few lines are written here to explain each term. Figure 6 provides a visual representation of these phenomena.

Wicking is a term used to describe the liquid that is drawn along a surface by capillary force and implies that one interface is replaced by another [72]. It causes the liquid to form a meniscus and in some cases a liquid film that covers the complete surface. An example is a sponge absorbing liquid. The term is also used for a liquid film drawn along a rough or micro-patterned surface [73]. Patterning can even speed up thin film propagation.

Pinning is the effect of the moving contact line withheld by a physical barrier (such as roughness on a surface). The liquid contact line and its adjacent surface have to deform before it can overcome this barrier [72].

Contact angle hysteresis is the difference between the advancing and receding contact angles (θ_{adv} and θ_{rec}, respectively) [74-77]. The angles are measured by placing a drop on a slope or by increasing / decreasing the drop volume. Common values lie between 20° and 50° [72]. Often only the static contact angle is described [52]. For a truly superhydrophobic surface (Cassie-Baxter state) the hysteresis should be low (< 10°). Roach et al. [33] state that hysteresis is not always suitable as a measure of the wetting state of a surface as the combined Cassie-Baxter / Wenzel state (as in figure 3e) can have a large hysteresis as the interfacial area between solid and liquid can be at least as large as on a flat surface.

2.4 Superhydrophobicity applied

Superhydrophobicity is also a favorite topic in (fundamental) hydrodynamic research. Flows along composite surfaces create partial slip conditions and the impact of droplets on superhydrophobic surfaces leads to very different dynamic behavior.

2.4.1 Slip

Despite the lack of a universally accepted, complete analytical method to predict interfacial slip, a multitude of experiments and simulations prove the existence of slip at (patterned) superhydrophobic surfaces [78]. To define slip, a distinction can be made between “true slip” and “apparent slip” (figure 7). When experiencing true slip, the fluid close to the wall moves with a different velocity than the wall itself. In the case of apparent slip, a low-viscosity phase in the fluid creates a larger velocity gradient near the wall. The slip occurs at the fluid-fluid interface instead of the fluid-solid interface, although it seems that the fluid slips at the wall.

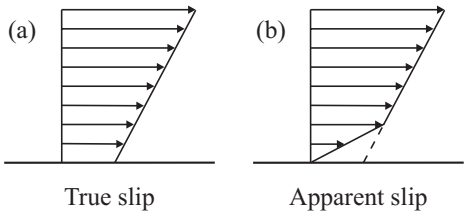

Figure 7. Illustrations of (a) true slip and (b) apparent slip profiles at a solid surface.

The amount of slip depends largely on the absolute amount of liquid-solid contact area. For planar Couette flow (one moving wall), the slip length is defined as the distance inside the wall at which the extrapolated fluid velocity would equal the velocity of the wall [78]. For forced-flow along stagnant walls, the same definition for the slip length is valid and it can be related to the external force driving the flow. Research has proven that slip also occurs at micro-patterned surfaces. By keeping a liquid in the Cassie-Baxter state, it is in constant contact with air pockets. Navier’s slip boundary condition [79] is valid there, resulting in a friction or drag reduction at this composite liquid-solid / liquid-air interface [13,14,80-84]. The slip effects disappear when the liquid enters the Wenzel state.

Slip can also occur on flat hydrophobic surfaces. It is believed that the presence of surface nanobubbles or a layer of low density fluid causes this slip [85,86]. The experimental evi-

dence of slip caused by surface nanobubbles and their stability is still under debate [87-89]. Simulations have predicted that stable surface nanobubbles can results into slip along the surface [90].

Tailored hydrodynamic properties can be useful to minimize friction in many practical applications. Slip generating surfaces can potentially be applied on boat hulls, in industrial pipes or in microfluidic devices. A comprehensive general review on the subject slip and its measuring techniques was given by Lauga, Brenner and Stone in 2005 [91,92], which was updated by Eijkel in 2007 [91,92]. In the same year (2005), also an extensive review on experimental studies of slip by Newtonian liquids on solid surfaces was published [85]. Many of these publications wrote implicitly about the relationship between slip and contact angle (hydrophobicity), but these properties were not coupled explicitly until a very recent review [78]. The authors warn that creating high-contact angle surfaces does not always lead to friction-reducing surfaces. Slip varies from one fluid-solid pair to another, even if the contact angle is the same for both of them.

2.4.2 Bouncing droplets

Additional to nature's self-cleaning properties, some animal makes use of superhydrophobicity to propel on water. A water strider is a remarkable animal that is not only able float on water because of its hairy legs, but can also jump [93]. These impacts are investigated fundamentally in research labs with bouncing droplets [29,57,94]. Most publications observe the shape of the liquid upon impact from the side. Viewing the impact of a droplet on a micro-patterned surface from above led to additional information on its behavior [50,95]. The center of the drop-base can transition into the Wenzel state, while the rest of the liquid rests on air pockets (Cassie-Baxter state). Depending on parameters described below, it is possible that the liquid retracts fully and releases from the surface (bounce).

Upon impact on a dry solid surface the droplet can be sticky (resonating on the surface after impact), have a partial or complete rebound or spread completely [29,72]. The drop morphologies are categorized in six regimes [96]: deposition, prompt splash, corona splash, receding brake-up, partial rebound and complete rebound. When droplets collide with another liquid or a wetted surface they cause waves, splashes and jets [94]. The most important dimensionless numbers to characterize these dynamics are the Weber, Reynolds and Ohnesorge numbers (equations 6-8). They describe the relationships between a fluid's inertial, surface tension and viscous forces.

$$We = \frac{\rho d {v_0}^2}{\sigma_{lg}} \tag{6}$$

$$Re = \frac{\rho d v_0}{\mu} \tag{7}$$

$$Oh = \frac{We^{0.5}}{Re} = \frac{\mu}{\left(\rho \sigma_{lg} d\right)^{0.5}} \tag{8}$$

ρ Is the liquid density, d the drop diameter, v_0 the impact velocity, σ_{lg} the surface tension and μ the dynamic viscosity of the liquid. Often the drop shape regimes are quantified by these dimensionless groups (*We*, *Re* and their ratio *Oh*) [94]. Rioboo et al. [96] claim that the thresholds between the regimes are better described by the individual physical parameters as the groups are insensitive to wettability and roughness effects. The thresholds between deposition and splash regimes are influenced by changing v_0, d, σ_{lg}, μ, roughness amplitude R_a and roughness wavelength R_w. For the break-up and rebound regimes the v_0, σ_{lg}, μ and receding contact angle θ_{rec} are influential. A complete overview of the influence is given in a review by Yarin [94].

2.5 Membranes and polymers

The purpose of this paragraph is to link the field of patterning for superhydrophobic purposes with the field of membrane technology. To understand how membrane processes can benefit from (micro-)patterning, some basic knowledge on membranes and polymers is presented here. Topics may be limited to the necessary information for this thesis.

2.5.1 Membrane technology: the basics

A membrane can be considered as a selective barrier between two phases (called feed and permeate side) [97]. The driving force for mass transport through the membrane can be a difference in concentration, pressure, temperature, electric potential between the two phases or a combination thereof. Membranes can handle gas, liquid and solid separations depending on its material and morphology. A schematic representation of a membrane separation process is given in figure 8.

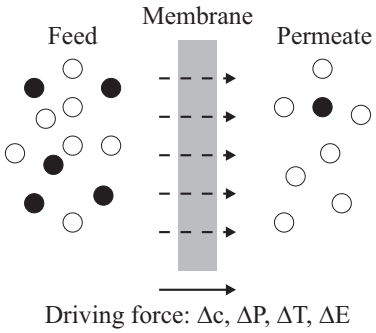

Figure 8. Illustration of a membrane separation process (adapted from [97]).

Each process needs membranes with specific properties. A small overview of the different processes including their driving forces is given here [97].

Gas permeation. Dense membranes (non-porous) can separate a gas from a gaseous flow when a concentration gradient over the membrane is present. Often, a porous membrane with a dense skin or coated top layer is used to minimize resistance. The material needs to be more selective for one component than the other. The mechanism for transport is described by the solution-diffusion model. The component absorbs into the membrane and moves in the direction of lower concentration via molecular diffusion. Gas separation through small pores is also possible (Knudsen and/or surface flow).

Vapor permeation / pervaporation. Liquids and vapors can be transported through dense or porous membranes following the solution-diffusion mechanism. The transport processes are called vapor permeation and pervaporation. In vapor permeation the feed is vaporized prior to coming in contact with the membrane, whereas in pervaporation the feed is a liquid. In both cases the driving force is a chemical potential difference stemming from differences in vapor pressure.

Liquid filtration. Membranes for liquid-solid/solute separations are (mainly) porous with pore sizes ranging from the (sub)nanometer to ten micrometer scale. Microfiltration, ultrafiltration, nanofiltration and reverse osmosis are pressure driven membrane processes for different size solutes and particles.

Membrane distillation. A thermally driven separation process like membrane distillation, a process in which two liquids or solutions at different temperatures are separated by a porous membrane, can also transport liquid caused by a vapor pressure difference. The vapor will only go through the pores if the liquid does not wet the pore walls.

Electrodialysis. Ions can be removed from aqueous solutions by electrically charged membranes. Membranes with a negative and positive charge, called cation- and anion-exchange membranes, respectively, are placed alternately between a cathode and anode to separate the ions. Similar ion transport processes occur in membrane electrolysis and fuel cells.

Facilitated transport. A carrier present inside the membrane selectively complexes one component to transport it to the permeate side of the membrane. The carrier phase can also be a liquid film separating the two phases. The separation also occurs because of differences in solubility and diffusivity in the liquid film.

Membrane contactors. A special kind of membrane is one that only functions as a contactor between two phases (gas-liquid or liquid-liquid). In general, the membrane is not selective, but it can generate a large area per volume and fixes the contact area in space.

2.5.2 Membrane transport

To characterize the performance of a membrane a few general formulas can be applied. The flux through a membrane *J* (equation 9) is determined to characterize the speed of the process. The coefficient *A* and gradient in driving force *dX* / *dx* are values, which vary for different membranes and operating procedures. For dense, defect-free membranes *A* is called permeability and is determined by the solubility and diffusivity of a component in a membrane. For porous membranes it is not the membrane material itself that determines *A*, but its porosity and tortuosity. The driving force *dX* / *dx* is the difference in chemical potential or pressure over a membrane with thickness *x*. A well-performing membrane not only has a high flux, but also obtains good separation. For dense membranes the term selectivity α is used (equation 10), while for porous membranes the retention *R* is used (equation 11). In both equations the concentration on the permeate side is compared to the concentration on the feed side. The separation factor of component A over component B $\alpha_{A/B}$ depends on the concentrations of the two components in the permeate y_A and y_B and their concentrations in the feed x_A and x_B. The parameters to calculate the retention are the solute concentration in the feed c_f and the solute concentration in the permeate c_p.

$$J = -A\frac{dX}{dx} \tag{9}$$

$$\alpha_{A/B} = \frac{y_A / y_B}{x_A / x_B} \tag{10}$$

$$R = \frac{c_f - c_p}{c_f} = 1 - \frac{c_p}{c_f} \tag{11}$$

In general, the flux is increased by reducing resistance (thin films) or increasing the surface to volume ratio. A good retention or selectivity is the result of a choice of the right material and preparation method. The bulk and surface morphology are just as important as the membrane material.

2.5.3 Concentration polarization

A common problem in membrane technology is concentration polarization [97,98]. Concentration polarization is the formation of a boundary layer at the membrane surface with increased or depleted solute concentration c_m (figure 9a and b, respectively). The magnitude of concentration polarization depends on the boundary layer thickness δ, the membrane's intrinsic enrichment $E_0 = c_p / c_m$, the volume flux through the membrane J_v and the diffusion coefficient of the solute in the boundary layer D_i according to the following equation [98]:

$$\frac{c_m}{c_f} = \frac{\exp\left(J_v \delta / D_i\right)}{1 + E_0\left[\exp\left(J_v \delta / D_i\right) - 1\right]} \tag{12}$$

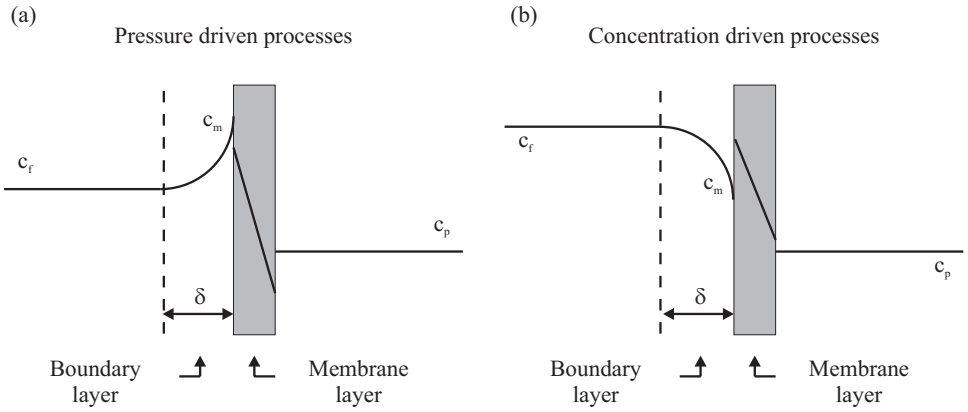

Figure 9. Illustrations of boundary layer formation with a gradient with at the surface: (a) increased and (b) depleted concentration at the membrane surface c_m compared to its feed concentration c_f. Adapted from [97,98].

An easy way to influence concentration polarization is to promote turbulence in the feed flow. An increase in turbulence will decrease the boundary layer thickness δ. The shape of the concentration gradient at the surface is influenced by changes in E_0, J_v or D_i. Changing these parameters may not be possible as the desired permeate quality and quantity is affected. Concentration polarization lowers permeation though the membrane. The retention can be lower, because of increased solute concentration at the membrane surface. The retention can also be higher when it affects the selectivity in a mixture of solutes.

2.5.4 Polymeric films: choice of polymer and preparation

Membrane materials can be either organic (biological or polymeric) or inorganic (ceramic). They are still largely considered as separate research fields, but examples of cross-over research with hybrid materials are increasingly seen [99-101]. In this thesis only experiments with polymeric membranes are discussed. For patterning techniques, polymers are an easy material to work with. Most are thermally moldable (for hot pressing and embossing) or dissolve in common solvents (for film casting). Their flexibility is also a positive feature for easy mold release.

Three polymers were used for the research in this thesis: polydimethylsiloxane (PDMS), a styrene-butadiene-styrene block copolymer (Kraton™ D-1102CS) and polyvinylidene fluoride (PVDF). PDMS and PVDF are very common membrane materials and have been used as (patterned) superhydrophobic surfaces before. PDMS is also a well-known polymer in the field of microfluidics and micro-contact printing. Some other polymers that have been used to create patterned superhydrophobic surfaces are polytetrafluoroethylene (PTFE or Teflon®) [102-104], nitrocellulose [105], cellulose acetate [106], polysulfone [107], Nafion® [108] and hyflon® [109]. Without patterning, polymers can also be made superhydrophobic via preparation techniques that create porous films (surface roughness). Some examples are liquid, vapor or thermally induced phase separated polypropylene [110], polyvinyl chloride (PVC) [111], polycarbonate [112] and polystyrene [113] films.

All polymeric films in this thesis are cast from solution on a (micro-patterned) wafer. Each of these polymers has its own preparation route to obtain the desired bulk and surface properties. PDMS and Kraton™ are rubbery polymers and have only been used in the dense (non-porous) form, whereas PVDF is a semicrystalline polymer with a rubbery amorphous phase, which has been prepared as porous films. The preparation routes are illustrated in figure 10 and described below.

A dense film is usually prepared by a solvent evaporation step after casting (route (a) in figure 10). This is an easy method, as the solvent evaporates slowly, leaving a smooth,

transparent and non-porous film on the wafer. Attention should be paid to humidity in the air as the water vapor can induce phase separation. As PDMS is not a solvent-polymer mixture, but a precursor and curing agent mixture, the polymeric film has to be cured/crosslinked to give it rigidity (route (b) in figure 10). To shorten the curing time this is performed at elevated temperatures. The amount of curing agent determines the elasticity of the film and its membrane properties.

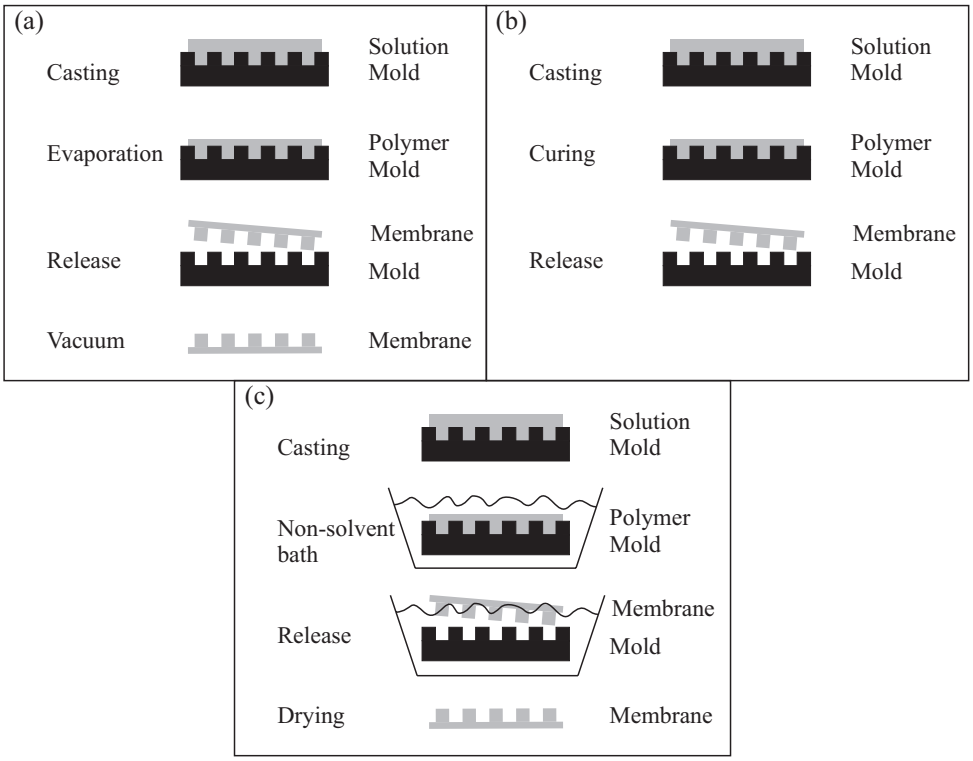

Figure 10. Illustration of the steps in three routes for preparing polymeric films: (a) evaporation, (b) thermal curing and (c) liquid induced phase separation.

Porous films are obtained when applying liquid or vapor induced phase separation (route (c) in figure 10). The wet polymer film is placed in a non-solvent bath or in a non-solvent vapor chamber. The solvent in the polymer solution is exchanged by non-solvent. This induces phase separation in polymer rich and polymer lean phases. The polymer rich phase subsequently solidifies (vitrifies), leaving a porous morphology after drying out the non-solvent. PVDF films were prepared via this method. The optimal porosity and pore size

is tuned by parameters such as polymer concentration, solvent – non-solvent affinity and temperature. Using vapor instead of liquid slows down the phase separation process and will also create a more homogeneous bulk porosity without macrovoids. A combination of an evaporation / vapor chamber step and a liquid bath is often used to create an integrally skinned membrane (a dense top-layer and a porous support in one). Porous films are usually easy to release from a micro-patterned mold as the materials shrinks. The technique does replicate the features well [114,115].

2.5.5 Patterned membranes: current status

In the field of membrane technology little research has been performed on micro-patterned membranes. However, macrocorrugated membranes date back to 1986 [116] when Racz et al. pressed corrugations into a polymeric film on a non-woven support to enhance mass transfer. Since then, a multitude of publications have been published on the use of corrugations in filtration experiments. Also related topics, such as hydrodynamics along corrugated membranes, have been researched. Turbulent flow patterns near the corrugations are the reason for enhanced transport to the surface [117].

In 2000, the first publication about pervaporation with macrocorrugated membranes appeared [25] followed by a few more [118-120]. Applying a pattern is a simple technique to increase surface area with respect to volume for the purpose of flux increase. Gronda et al. show an increase of flux in pervaporation experiments for less permeable solutes. No increase was found for highly permeable solutes as the corrugations led to a depleted surface concentration. The paper also describes a model for flux enhancement in membranes with nanocorrugations. This was very recently investigated experimentally [121]. A surface-modified membrane led to a solute flux increase of 14% during pervaporation experiments. The increase in surface area was only 4%, which is not enough to explain the higher flux increase. The additional enhancement is attributed to improved fluid dynamic conditions due to micro-turbulence at the membrane surface. The authors state that soft rubber materials (as PDMS) could also benefit from micro- and nano-patterning. Chapter 3 describes this topic for gas permeation through micro-patterned PDMS membranes.

From an industrial point of view, patterning hollow fibers is interesting as well. As has been revealed in 2005 [122], it is possible to pattern fibers with a spinneret containing a micro-pattern both on the outside and on the inside. Gas permeation experiments were performed and the results were compared to circular fibers with the same diameter. The increase of gas flow of 19% was solely attributed to the increase in surface area.

In electrodialysis processes the existance of the limiting current density is a direct result of concentration polarization [123]. Rubinstein et al. proposed a theory of electro-convection that predicts a shortening of the plateau length in the current-voltage curve for membranes with increased conductive or geometrical heterogeneity [124-130]. Experimental research with micro-patterned electrodialysis membranes confirms this theory as the plateau length is indeed shortened [123].
Another theoretical publication on flow along a porous wall states that slip can minimize concentration polarization [28]. If enough slip is generated by patterned polymeric surfaces, membrane technology could benefit hugely from the micro-patterning technique. Experiments to confirm this statement are described in chapter 6.

2.6 Conclusions

Surface design (both chemical and geometrical) can largely influence the wetting properties of a solid. Hydrophilic materials can become superhydrophilic and hydrophobic materials superhydrophobic. A geometrical design technique such as micro-patterning is often used in superhydrophobic research.
Fundamental research on the design of these surfaces is mainly geared towards the development of liquid repelling surfaces. Liquid in the Cassie-Baxter state is floating on air pockets and can easily roll off a tilted surface, whereas liquid in the Wenzel state is wetting the whole solid area and pinned on the features when tilted. Another phenomenon that uses the presence of liquid-air interfaces is liquid slip along a solid surface. Improved hydrodynamics serve many practical applications, often in the field of microfluidics. A research area that has not made much use of slip so far is the field of membrane technology. Transport in filtration and pervaporation processes could also benefit from slip if it is large enough to influence the concentration polarization layer. Micro-patterning can furthermore lead to enhanced gas permeation due to increase of surface area and to the introduction of lateral flux.
The forthcoming chapters in this thesis all have the micro-patterning technique as the common feature, but with the various applications as described above in mind. This chapter has given the basic knowledge for the use and preparation of micro-patterned polymers to enhance membrane performance (chapter 3), tune wetting properties (chapter 4 and 5) or hydrodynamics (chapter 6).

2.7 References

1. http://dictionary.cambridge.org **24-9-2008**.
2. Cai, W. S.; Gupta, R. B. *Journal of Applied Polymer Science* **2002**, *83*, 169-178.
3. Pilotek, S.; Schmidt, H. K. *Journal of Sol-Gel Science and Technology* **2003**, *26*, 789-792.
4. Tang, F. Q.; Fudouzi, H.; Uchikoshi, T.; Sakka, Y. *Journal of the European Ceramic Society* **2004**, *24*, 341-344.
5. Wang, T.; Kang, E. T.; Neoh, K. G.; Tan, K. L.; Liaw, D. J. *Langmuir* **1998**, *14*, 921-927.
6. Alem, H.; Duwez, A. S.; Lussis, P.; Lipnik, P.; Jonas, A. M.; Demoustier-Champagne, S. *Journal of Membrane Science* **2008**, *308*, 75-86.
7. Joseph, P.; Tabeling, P. *Physical Review E* **2005**, *71*.
8. Kim, S. H.; Misner, M. J.; Xu, T.; Kimura, M.; Russell, T. P. *Advanced Materials* **2004**, *16*, 226-231.
9. Han, J. T.; Xu, X. R.; Cho, K. W. *Langmuir* **2005**, *21*, 6662-6665.
10. Peinemann, K.-V.; Konrad, M.; Abetz, V. *Desalination* **2006**, *199*, 124-126.
11. Peinemann, K. V.; Abetz, V.; Simon, P. F. W. *Nature Materials* **2007**, *6*, 992-996.
12. Lau, K. K. S.; Bico, J.; Teo, K. B. K.; Chhowalla, M.; Amaratunga, G. A. J.; Milne, W. I.; McKinley, G. H.; Gleason, K. K. *Nano Letters* **2003**, *3*, 1701-1705.
13. Joseph, P.; Cottin-Bizonne, C.; Benoit, J. M.; Ybert, C.; Journet, C.; Tabeling, P.; Bocquet, L. *Physical Review Letters* **2006**, *97*.
14. Choi, C. H.; Kim, C. J. *Physical Review Letters* **2006**, *96*.
15. Choi, C. H.; Kim, C. J. *Physical Review Letters* **2006**, *97*.
16. Brandon, S.; Haimovich, N.; Yeger, E.; Marmur, A. *Journal of Colloid and Interface Science* **2003**, *263*, 237-243.
17. Cubaud, T.; Fermigier, M. *Journal of Colloid and Interface Science* **2004**, *269*, 171-177.
18. Kusumaatmaja, H.; Leopoldes, J.; Dupuis, A.; Yeomans, J. M. *Europhysics Letters* **2006**, *73*, 740-746.
19. Kusumaatmaja, H.; Yeomans, J. M. *Langmuir* **2007**, *23*, 6019-6032.
20. Becker, H.; Gartner, C. *Electrophoresis* **2000**, *21*, 12-26.
21. Becker, H.; Gartner, C. *Analytical and Bioanalytical Chemistry* **2008**, *390*, 89-111.
22. Groenendijk, M.; Meijer, J. *Journal of Laser Applications* **2006**, *18*, 227-235.
23. Bico, J.; Marzolin, C.; Quere, D. *Europhysics Letters* **1999**, *47*, 220-226.

24. Bico, J.; Marzolin, C.; Quere, D. *Europhysics Letters* **1999**, *47*, 743-744.
25. Gronda, A. M.; Buechel, S.; Cussler, E. L. *Journal of Membrane Science* **2000**, *165*, 177-187.
26. Geissler, M.; Xia, Y. N. *Advanced Materials* **2004**, *16*, 1249-1269.
27. Jokinen, V.; Sainiemi, L.; Franssila, S. *Advanced Materials* **2008**, *early view*.
28. Chellam, S.; Wiesner, M. R.; Dawson, C. *Journal of Engineering Mathematics* **1992**, *26*, 481-492.
29. de Gennes, P.-G.; Brochard-Wyart, F.; Quere, D. *Capillarity and wetting phenomena: Drops, bubbles, pearls, waves*; 1st ed.; Springer Science & Business Media, Inc.: New York, 2003.
30. Wenzel, R. N. *Industrial & Engineering Chemistry* **1936**, *28*, 988-994.
31. Cassie, A. B. D.; Baxter, S. *Transactions of the Faraday society* **1944**, *40*, 546-551.
32. Marmur, A. *Langmuir* **2003**, *19*, 8343-8348.
33. Roach, P.; Shirtcliffe, N. J.; Newton, M. I. *Soft Matter* **2008**, *4*, 224-240.
34. Xia, F.; Jiang, L. *Advanced Materials* **2008**, *20*, 2842-2858.
35. Feng, X. J.; Feng, L.; Jin, M. H.; Zhai, J.; Jiang, L.; Zhu, D. B. *Journal of the American Chemical Society* **2004**, *126*, 62-63.
36. Sun, T. L.; Wang, G. J.; Feng, L.; Liu, B. Q.; Ma, Y. M.; Jiang, L.; Zhu, D. B. *Angewandte Chemie-International Edition* **2004**, *43*, 357-360.
37. Shirtcliffe, N. J.; McHale, G.; Newton, M. I.; Perry, C. C.; Roach, P. *Chemical Communications* **2005**, 3135-3137.
38. Boys, C. V. *Soap bubbles and the forces which mould them*; 1st ed.; Society for Promoting Christian Knowledge, 1902.
39. Barthlott, W. In *Scanning electron microscopy in taxonomy and functional morphology*; Claugher, D., Ed.; Clarendon Press: Oxford, 1990.
40. Barthlott, W. In *Evolution and systematics of the Caryophyllales*; Behnke, H. D., Mabry, T. J., Eds.; Springer: Berlin, 1993.
41. Neinhuis, C.; Barthlott, W. *Annals of Botany* **1997**, *79*, 667-677.
42. Onda, T.; Shibuichi, S.; Satoh, N.; Tsujii, K. *Langmuir* **1996**, *12*, 2125-2127.
43. Barthlott, W.; Neinhuis, C. *Planta* **1997**, *202*, 1-8.
44. *US trademark 2613850* **1999**.
45. *German trademark 39958441.2* **1999**.
46. Li, S. H.; Zhang, S. B.; Wang, X. H. *Langmuir* **2008**, *24*, 5585-5590.

47. Quere, D.; Reyssat, M. *Philosophical Transactions of the Royal Society a-Mathematical Physical and Engineering Sciences* **2008**, *366*, 1539-1556.
48. Krupenkin, T. N.; Taylor, J. A.; Schneider, T. M.; Yang, S. *Langmuir* **2004**, *20*, 3824-3827.
49. Bahadur, V.; Garimella, S. V. *Langmuir* **2008**, *24*, 8338-8345.
50. Reyssat, M.; Pepin, A.; Marty, F.; Chen, Y.; Quere, D. *Europhysics Letters* **2006**, *74*, 306-312.
51. Dorrer, C.; Ruhe, J. *Langmuir* **2007**, *23*, 3820-3824.
52. Chen, W.; Fadeev, A. Y.; Hsieh, M. C.; Oner, D.; Youngblood, J.; McCarthy, T. J. *Langmuir* **1999**, *15*, 3395-3399.
53. Nakajima, A.; Hashimoto, K.; Watanabe, T. *Monatshefte Fur Chemie* **2001**, *132*, 31-41.
54. Blossey, R. *Nature Materials* **2003**, *2*, 301-306.
55. Sun, T. L.; Feng, L.; Gao, X. F.; Jiang, L. *Accounts of Chemical Research* **2005**, *38*, 644-652.
56. Sun, T. L.; Feng, L.; Gao, X. F.; Jiang, L. *Accounts of Chemical Research* **2006**, *39*, 487-487.
57. Callies, M.; Quere, D. *Soft Matter* **2005**, *1*, 55-61.
58. Feng, X.; Jiang, L. *Advanced Materials* **2006**, *18*, 3063-3078.
59. Ma, M.; Hill, R. M. *Current Opinion in Colloid & Interface Science* **2006**, *11*, 193-202.
60. Li, X. M.; Reinhoudt, D.; Crego-Calama, M. *Chemical Society Reviews* **2007**, *36*, 1350-1368.
61. Li, X. M.; Reinhoudt, D.; Crego-Calama, M. *Chemical Society Reviews* **2007**, *36*, 1529-1529.
62. Feng, L.; Li, S. H.; Li, Y. S.; Li, H. J.; Zhang, L. J.; Zhai, J.; Song, Y. L.; Liu, B. Q.; Jiang, L.; Zhu, D. B. *Advanced Materials* **2002**, *14*, 1857-1860.
63. Extrand, C. W. In *Encyclopedia of surface and colloid science*; 2nd ed.; Somasundaran, P., Ed.; Taylor & Francis: New York, 2006.
64. Marmur, A. *Langmuir* **2008**, *24*, 7573-7579.
65. Fabbri, P.; Messori, M.; Pilati, F.; Taurino, R.; Tonelli, C.; Toselli, M. *Advances in Polymer Technology* **2007**, *26*, 182-190.
66. Hoefnagels, H. F.; Wu, D.; de With, G.; Ming, W. *Langmuir* **2007**, *23*, 13158-13163.

67. Yan, L. H.; Chi, F. T.; Jiang, X. D.; Lu, H. B.; Yuan, X. D.; Jiang, B. *Journal of Inorganic Materials* **2007**, *22*, 1247-1250.
68. Tuteja, A.; Choi, W.; Ma, M. L.; Mabry, J. M.; Mazzella, S. A.; Rutledge, G. C.; McKinley, G. H.; Cohen, R. E. *Science* **2007**, *318*, 1618-1622.
69. Wang, Y.; Bachman, M.; Sims, C. E.; Li, G. P.; Allbritton, N. L. *Analytical Chemistry* **2007**, *79*, 7104-7109.
70. Koc, Y.; de Mello, A. J.; McHale, G.; Newton, M. I.; Roach, P.; Shirtcliffe, N. J. *Lab on a Chip* **2008**, *8*, 582-586.
71. Spori, D. M.; Drobek, T.; Zurcher, S.; Ochsner, M.; Sprecher, C.; Muehlebach, A.; Spencer, N. D. *Langmuir* **2008**, *24*, 5411-5417.
72. Quere, D. *Reports on Progress in Physics* **2005**, *68*, 2495-2532.
73. Ishino, C.; Reyssat, M.; Reyssat, E.; Okumura, K.; Quere, D. *Europhysics Letters* **2007**, *79*, 56005.
74. Johnson, R. E.; Dettre, R. H. *Advances in Chemistry Series* **1964**, *43*, 112-135.
75. Johnson, R. E.; Dettre, R. H. *Advances in Chemistry Series* **1964**, *43*, 136-144.
76. Wang, X. D.; Peng, X. F.; Lu, J. F.; Liu, T.; Wang, B. X. *Heat transfer - Asian Research* **2004**, *33*, 201-210.
77. He, B.; Lee, J.; Patankar, N. A. *Colloids and Surfaces A: Physicochemical and Engineering Aspects* **2004**, *248*, 101-104.
78. Voronov, R. S.; Papavassiliou, D. V.; Lee, L. L. *Industrial & Engineering Chemistry Research* **2008**, *47*, 2455-2477.
79. Navier, C. L. M. H. In *Memoires de l'Academie des Sciences de l'Institut de France*, 1827; Vol. 6.
80. Cottin-Bizonne, C.; Barrat, J. L.; Bocquet, L.; Charlaix, E. *Nature Materials* **2003**, *2*, 237-240.
81. Choi, C. H.; Westin, K. J. A.; Breuer, K. S. *Physics of Fluids* **2003**, *15*, 2897-2902.
82. Lauga, E.; Stone, H. A. *Journal of Fluid Mechanics* **2003**, *489*, 55-77.
83. Roach, P.; McHale, G.; Evans, C. R.; Shirtcliffe, N. J.; Newton, M. I. *Langmuir* **2007**, *23*, 9823-9830.
84. Ybert, C.; Barentin, C.; Cottin-Bizonne, C.; Joseph, P.; Bocquet, L. *Physics of Fluids* **2007**, *19*.
85. Neto, C.; Evans, D. R.; Bonaccurso, E.; Butt, H. J.; Craig, V. S. J. *Reports on Progress in Physics* **2005**, *68*, 2859-2897.
86. Tretheway, D. C.; Meinhart, C. D. *Physics of Fluids* **2004**, *16*, 1509-1515.
87. Zhang, X. H.; Khan, A.; Ducker, W. A. *Physical Review Letters* **2007**, *98*.

88. Zhang, X. H.; Quinn, A.; Ducker, W. A. *Langmuir* **2008**, *24*, 4756-4764.
89. Brenner, M. P.; Lohse, D. **2008**, *submitted*.
90. Steinberger, A.; Cottin-Bizonne, C.; Kleimann, P.; Charlaix, E. *Nature Materials* **2007**, *6*, 665-668.
91. Lauga, E.; Brenner, M. P.; Stone, H. A. In *Handbook of Experimental Fluid Dynamics*; Foss, J., Tropea, C., Yarin, A., Eds.; Springer: New-York, 2007.
92. Eijkel, J. *Lab on a Chip* **2007**, *7*, 299-301.
93. Hu, D. L.; Chan, B.; Bush, J. W. M. *Nature* **2003**, *424*, 663-666.
94. Yarin, A. L. *Annual Review of Fluid Mechanics* **2006**, *38*, 159-192.
95. Bartolo, D.; Bouamrirene, F.; Verneuil, E.; Buguin, A.; Silberzan, P.; Moulinet, S. *Europhysics Letters* **2006**, *74*, 299-305.
96. Rioboo, R.; Tropea, C.; Marengo, M. *Atomization and Sprays* **2001**, *11*, 155-165.
97. Mulder, M. *Basic principles of membrane technology*; 2nd ed.; Kluwer Academic Publishers: Dordrecht, 1997.
98. Baker, R. W. *Membrane technology and applications*; 2nd ed.; John Wiley & Sons, Ltd: Chichester, England, 2004.
99. Mahajan, R.; Vu, D. Q.; Koros, W. J. *Journal of the Chinese Institute of Chemical Engineers* **2002**, *33*, 77-86.
100. Yoshida, W.; Cohen, Y. *Journal of Membrane Science* **2003**, *213*, 145-157.
101. de Jong, J.; Benes, N. E.; Koops, G. H.; Wessling, M. *Journal of Membrane Science* **2004**, *239*, 265-269.
102. Scott, K.; Mahmood, A. J.; Jachuck, R. J.; Hu, B. *Journal of Membrane Science* **2000**, *173*, 1-16.
103. Kim, D.; Kim, J.; Park, H. C.; Lee, K. H.; Hwang, W. *Journal of Micromechanics and Microengineering* **2008**, *18*.
104. Scott, K.; Jachuck, R. J.; Hall, D. *Separation and Purification Technology* **2001**, *22-3*, 431-441.
105. Hu, B.; Scott, K. *Journal of Membrane Science* **2007**, *294*, 30-39.
106. Vanderwaal, M. J.; Racz, I. G. *Journal of Membrane Science* **1989**, *40*, 243-260.
107. Vanderwaal, M. J.; Stevanovic, S.; Racz, I. G. *Journal of Membrane Science* **1989**, *40*, 261-275.
108. Tzanetakis, N.; Taama, W. M.; Scott, K.; Jachuck, R. J. J. *Journal of Applied Electrochemistry* **2003**, *33*, 411-417.
109. Vogelaar, L.; Lammertink, R. G. H.; Wessling, M. *Langmuir* **2006**, *22*, 3125-3130.
110. Erbil, H. Y.; Demirel, A. L.; Avci, Y.; Mert, O. *Science* **2003**, *299*, 1377-1380.

111. Li, X. H.; Chen, G. M.; Ma, Y. M.; Feng, L.; Zhao, H. Z.; Jiang, L.; Wang, F. S. *Polymer* **2006**, *47*, 506-509.
112. Zhao, N.; Xu, J.; Xie, Q. D.; Weng, L. H.; Guo, X. L.; Zhang, X. L.; Shi, L. H. *Macromolecular Rapid Communications* **2005**, *26*, 1075-1080.
113. Yuan, Z. Q.; Chen, H.; Tang, J. X.; Chen, X.; Zhao, D. J.; Wang, Z. X. *Surface & Coatings Technology* **2007**, *201*, 7138-7142.
114. Vogelaar, L.; Barsema, J. N.; van Rijn, C. J. M.; Nijdam, W.; Wessling, M. *Advanced Materials* **2003**, *15*, 1385-+.
115. Vogelaar, L.; Lammertink, R. G. H.; Barsema, J. N.; Nijdam, W.; Bolhuis-Versteeg, L. A. M.; van Rijn, C. J. M.; Wessling, M. *Small* **2005**, *1*, 645-655.
116. Racz, I. G.; Wassink, J. G.; Klaassen, R. *Desalination* **1986**, *60*, 213-222.
117. Zhang, L. Z. *Journal of Membrane Science* **2005**, *260*, 75-83.
118. Quinones-Bolanos, E.; Zhou, H. D.; Parkin, G. *Journal of Environmental Engineering-Asce* **2005**, *131*, 1633-1643.
119. Quinones-Bolanos, E.; Zhou, H. D.; Soundararajan, R.; Otten, L. *Journal of Membrane Science* **2005**, *252*, 19-28.
120. Quinones-Bolanos, E.; Zhou, H. D. *Journal of Environmental Engineering-Asce* **2006**, *132*, 1011-1018.
121. Izák, P.; Godinho, M. H.; Brogueira, P.; Figueirinhas, J. L.; Crespo, J. G. *Journal of Membrane Science* **in press**.
122. Nijdam, W.; de Jong, J.; van Rijn, C. J. M.; Visser, T.; Versteeg, L.; Kapantaidakis, G.; Koops, G. H.; Wessling, M. *Journal of Membrane Science* **2005**, *256*, 209-215.
123. Balster, J., University of Twente, 2006.
124. Rubinstein, I.; Maletzki, F. *Journal of the Chemical Society-Faraday Transactions* **1991**, *87*, 2079-2087.
125. Rubinstein, I.; Zaltzman, B.; Kedem, O. *Journal of Membrane Science* **1997**, *125*, 17-21.
126. Rubinstein, I.; Zaltzman, B. *Physical Review E* **2000**, *62*, 2238-2251.
127. Rubinstein, I.; Zaltzman, B. *Mathematical Models & Methods in Applied Sciences* **2001**, *11*, 263-300.
128. Rubinstein, I.; Zaltzman, B.; Pundik, T. *Physical Review E* **2002**, *65*.
129. Rubinstein, I.; Zaltzman, B. *Physical Review E* **2003**, *68*.
130. Rubinstein, I.; Zaltzman, B.; Lerman, I. *Physical Review E* **2005**, *72*.

Chapter 3

Comparing flat and micro-patterned surfaces: gas permeation and tensile stress measurements

Micro-patterning is a suitable method to produce patterned membranes that display increased flux compared to flat membranes. In this work we studied the permeation of four different gases (nitrogen, helium, oxygen and carbon dioxide) through Kraton^{TM} polymer (SBS) membranes. It is possible to cast a micro-patterned membrane with 25 μm high and 30 μm wide lines that has a thickness of 5 μm at its thinnest point. Using this micro-pattern, the experimental diffusive gas flux was increased up to 59% compared to non-patterned membranes with the same polymer volume. Finite-element simulations confirm this enhancement. Selectivities are similar for both flat and micro-patterned membranes and in accordance with literature. Tensile stress measurements confirm that the micro-patterned membranes yield only limited loss in mechanical strength. Although only one material and geometry is explored here, this principle is generally applicable to all diffusion driven processes.

This chapter has also been published as a paper:

- A.M. Peters, R.G.H. Lammertink and M. Wessling, Comparing flat and micro-patterned surfaces: Gas permeation and tensile stress measurements, Journal of Membrane Science, 320 (2008) 173.

3.1 Introduction

Selectivity and permeability are material properties that characterize the membrane performance. By adapting the geometry of a membrane the flux can be improved without loss in selectivity. Thinner films lead to higher fluxes, but also a lower mechanical strength. This problem is overcome by creating composite membranes. The membrane is coated as a very thin layer onto a support which provides the mechanical strength [1].

Another possibility to increase flux is to increase the effective membrane surface. Gronda et al. [2] used a double mold to create macrocorrugations (mm range) on both sides. Although theory predicts a 5-fold flux increase for pervaporation, the maximal experimental increase was 2-fold. For high permeable solutes there was no increase observed at all due to depletion of the solute at the surface. It was also stated that macrocorrugated membranes do not have a future in industrial applications, because they are too large to fit into industrial modules. Theory, however, predicts that smaller geometries (nanocorrugated membranes) could also yield similar enhancements.

Nijdam et al. [3] demonstrated a method to increase the flux through a hollow fiber by changing its geometry. The outer surface area of the hollow fiber was increased by 19% due to patterning using a spinneret insert. Gas permeation measurements proved that the membrane properties such as the selectivity, normalized permeability and skin thickness were comparable to the circular fibers. Not only the outer surface, but also the inner surface could be micro-patterned.

These researchers have shown us that patterning a surface can be advantageous in terms of enhancing flux while maintaining selectivity. However, surface enhancement is not the only mechanism playing a role. By reshaping a given amount of polymer as a micro-pattern the diffusion paths through the membrane are altered. Its flux increases compared to a flat membrane with the same amount of polymer. This mechanism is presented in this paper by comparing patterned and non-patterned dense membranes for gas permeation. The research is also extended to composite membranes by comparing a fully permeable micro-patterned membrane with a partly non-permeable membrane (composite) of the same geometry.

3.2 Experimental

All materials were used as received. The block copolymer Kraton^{TM} D-1102CS (styrene-butadiene-styrene, Kraton polymers) was dissolved in toluene (Merck, analysis grade) to

make 30 wt% solutions. This polymer is linear containing 29.5 wt% styrene, which results in a cylindrical morphology on the nanoscale. These materials were chosen to ensure easy release of thin films from silicon wafers.

3.2.1 Membrane preparation

Dense flat sheet membranes are obtained by casting a polymer solution on a substrate [4] and removing the film after evaporation of the solvent (figure 1). The substrate is either a flat 4 inch silicon wafer or a silicon mold with a line pattern. The mold was produced in a clean room by standard photolithography, followed by deep reactive ion etching. The dimensions of the pattern on the mold are: depth of channel = 25 µm, width of channel = 30 µm, width between channels = 20 µm. The evaporation occurred overnight and the membrane was released by using ethanol and gentle pulling. The membrane was then dried overnight in a vacuum oven at 303 K. The result is a continuous polymer film with ridges (25 µm high and 30 µm wide), a perfect replica of the mold-pattern. The thickness of the continuous film can easily be varied by changing the casting thickness.

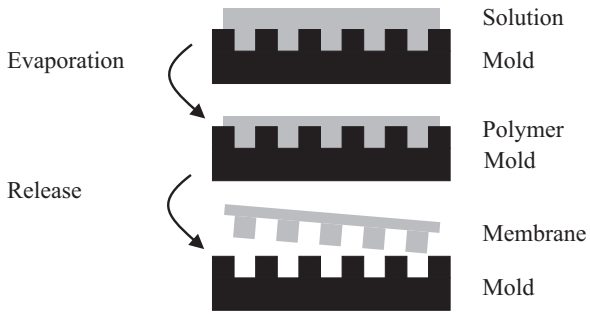

Figure 1. Schematic representation of the membrane micro-patterning method (side view).

3.2.2 SEM

A scanning electron microscope (SEM, JSM 5600LV, JEOL) was used to determine the morphology and dimensions of the membranes. The membranes were broken in liquid nitrogen and sputtered with a 30 nm gold layer (SCD 040, Balzers Union). Pictures were taken at 5kV.

3.2.3 Gas permeation

Gas permeation measurements were done in a home-built low pressure set-up with a permeation area of 11.95 cm^2 per cell [5]. The measurements are performed at a constant volume and variable pressure. The four gases nitrogen, helium, oxygen and carbon dioxide were always measured in the same order. The applied pressure was 2.5 bar on the feed side and initial vacuum on the permeate side. During measurements the permeate gas was collected. The operating temperature was 308 K. The micro-patterned side of the membranes faced the feed side. The orientation of the pattern is important as the pattern will be deformed when pressed against the membrane support when it is facing the permeate side.

3.2.4 Tensile stress

The tensile stress was calculated from measurements with a tensiometer (Z020, Zwick). The ISO37 standard was used for sample preparation. The preload was set at 0.05 N. The membranes were stretched at a velocity of 10 mm/min. The force to reach a certain strain was measured and the effective membrane thickness was used to calculate the average stress within the whole membrane. The tensile stress was evaluated at 5% strain to compare each membrane equally. Their effective thicknesses vary from 13.5 to 47.7 µm. Hysteresis measurements have revealed that 5% strain is within the elastic regime for these membranes.

3.2.5 Simulations

Gas permeation simulations were performed based on a finite element method in the convection and diffusion module of COMSOL Multiphysics 3.3. The micro-patterned membrane was represented by a 25 µm wide cross-section containing half of the ridge and half of the continuous film. The vertical walls can be regarded as symmetry boundaries. The thickness of the continuous film was varied to simulate different effective membrane thicknesses. The calculations were simplified by assuming isotropic diffusion without convection. At the feed side an initial gas concentration c_0 = 4 mol/m^3 and at the permeate side a vacuum (c_0 = 0 mol/m^3) was applied. All other boundaries were assumed insulating/symmetrical. The diffusion coefficient D was set at 2.8 x 10^{-11} m^2/s, the experimentally determined value for nitrogen permeation. These values were used in all simulations as the final enhancement results are independent of the concentration gradient and diffusion constant. To verify this, the constants were varied up to two orders of magnitude. The mesh size was decreased until the result was constant. A typical mesh size is 10^{-7} m. A station-

ary nonlinear direct (UMFPACK) solver was used. The diffusive flux was determined by integrating over the permeate boundary of the membrane.

3.3 Results and discussion

3.3.1 Membrane preparation

Micro-patterned and flat membranes of equal volume are compared. Figure 2 shows that a micro-patterned membrane with a continuous layer of 15 µm and 25 µm high ridges is comparable to a flat membrane with an effective membrane thickness (Δx) of 30 µm.

If a flat dense membrane is too thin (< 30 µm), it is very difficult to remove it from a wafer without rupturing the film. Micro-patterning membranes, however, can create much thinner sections, while maintaining sufficient mechanical strength. Figure 3 shows SEM pictures of two micro-patterned membranes, one with a relatively thick continuous film of ~ 50 µm (A) and one with a thinner continuous film of ~ 5 µm (B). The waviness of this membrane is due to the shrinkage during drying on the mold. There is a solvent concentration gradient towards the mold substrate during evaporation. When the thin continuous film is mostly dried, the membrane ridges still contain solvent. Further evaporation of solvent from these ridges results in further shrinkage and a deformation of the continuous film.

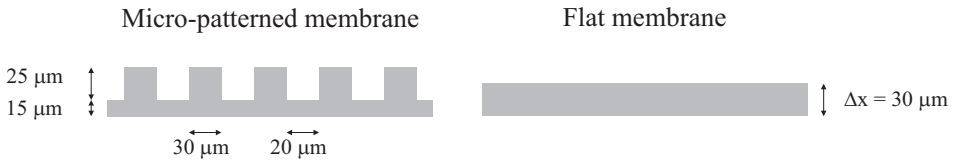

Figure 2. Schematic representation of the cross-section of a micro-patterned membrane (left) and a flat membrane (right) with the same polymer volume.

3.3.2 Gas permeation

Gas permeation experiments on flat and micro-patterned films were performed and compared with analytical calculations and finite element simulations. Equations 1 and 2 show the one-dimensional flux-equations (for this particular line pattern) based on Fick's first law of diffusion [6]. This approach neglects any lateral diffusion in the membrane. It can be used to quickly estimate the advantage of micro-patterning.

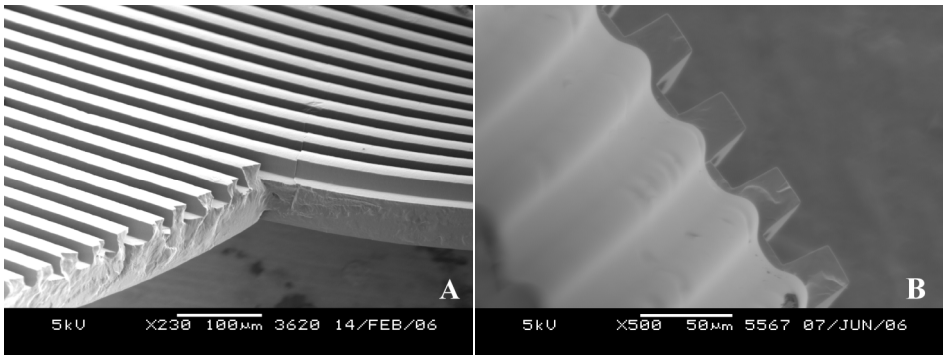

Figure 3. SEM pictures of micro-patterned membranes: (A) cross-section / top surface with a thick (~ 50 µm) continuous film and (B) cross-section / bottom surface with a thin (~ 5 µm) continuous film.

For the micro-patterned membrane, the flux-equation is divided into two parts: the flux through the thicker part and the flux through the thinner part of the membrane. Equation 3 gives the theoretical advantage (*T*) of micro-patterning a membrane. *J*, *D* and *Δc* are, respectively, the flux, diffusion coefficient and concentration difference over a membrane of effective thickness *Δx*.

$$J_{flat}^{theory} = -D\frac{\Delta c}{\Delta x} \tag{1}$$

$$J_{patterned}^{theory} = \frac{30}{50}\left(-D\frac{\Delta c}{\Delta x + 10}\right) + \frac{20}{50}\left(-D\frac{\Delta c}{\Delta x - 15}\right) \tag{2}$$

$$T = \frac{J_{patterned}^{theory} - J_{flat}^{theory}}{J_{flat}^{theory}} \times 100\% \tag{3}$$

Simulations were done to take the lateral gas diffusion into account that occurs in the micro-patterned membrane. Figure 4 shows the concentration profile of gas permeating through a cross-section of the micro-patterned membrane. The diffusion coefficient was considered constant for this simulation. The concentration profile changes from high concentration (red) to zero concentration (blue).

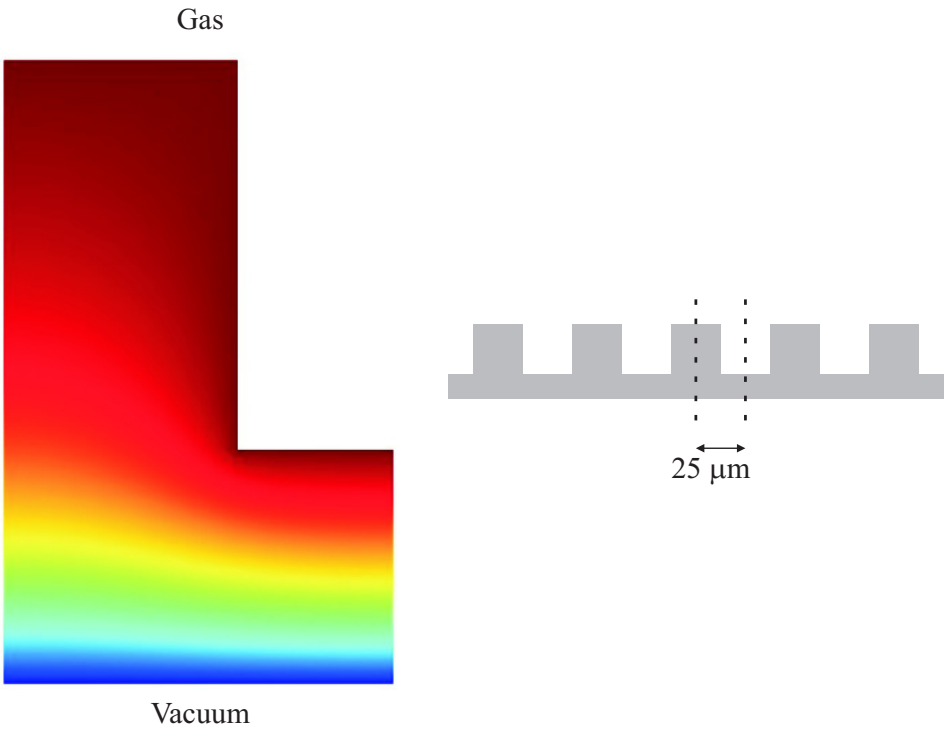

Figure 4. Concentration profile (left) of gas diffusing through a section of a micro-patterned membrane (right).

The effect of the micro-pattern on the concentration profile is clearly visible in this figure. Mass transfer through the thinner continuous film is faster than through the thicker ridges due to the increased concentration gradient. Compared to the analytical calculations, lateral transport enhances the average concentration in the ridge and thus diffusion through the ridges. The micro-patterned membrane can be compared to a composite membrane: a thin selective layer and a thicker pattern for mechanical stability.

Gas permeation measurements were performed to verify the theoretical expectations and simulation results. The flux of a micro-patterned membrane was normalized against its effective thickness (equation 4). Equation 5 gives the average permeability (P) of multiple flat membranes (n). These individual permeabilities are calculated the same way as in equation 4. The experimental advantage (E) of micro-patterning a membrane is calculated with equation 6.

$$P_{patterned}^{exp} = J_{patterned}^{exp} \Delta x \tag{4}$$

$$\left\langle P_{flat}^{exp} \right\rangle = \frac{P_{flat,1}^{exp} + \ldots + P_{flat,n}^{exp}}{n} \tag{5}$$

$$E = \frac{P_{patterned}^{exp} - \left\langle P_{flat}^{exp} \right\rangle}{\left\langle P_{flat}^{exp} \right\rangle} \times 100\% \tag{6}$$

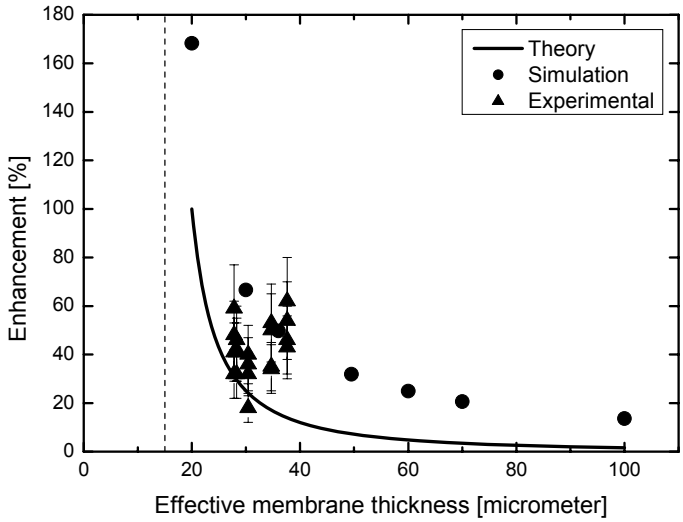

Figure 5. Enhancement of gas permeation through micro-patterned membranes compared to flat membranes: (—) analytical calculations, (●) simulations and (▲) experimental results. The dashed line is the minimum effective thickness for the geometry which is studied.

In figure 5 the flux enhancement is plotted versus the effective membrane thickness. The enhancement as calculated from simulations with a constant diffusion coefficient (●) is significantly stronger than for the analytical calculations (—). This is the sole effect of gas diffusing laterally through the micro-patterned membrane. The flux enhancement at high effective membrane thicknesses becomes less due to the fact that the height of the ridges is

small compared to the total thickness of the membrane. Membrane A in figure 3, e.g., will benefit less from the micro-pattern compared to membrane B. The theoretical minimum effective thickness for this geometry is 15 µm. At this thickness, all material is just enough to fill the mold valleys and no continuous film will be formed.

The experimental data (▲) was obtained from gas permeation measurements with different gases (N_2, He, O_2 and CO_2; measured in that order). Five thicknesses using four gases each were measured, resulting in 20 experimental points. Per point, the results of a series of flat membranes are compared to the results of a micro-patterned membrane. The error is large due to the fact that the reproducibility for different membranes was limited (standard deviation of 13%). The membrane thicknesses were measured from SEM pictures, which do not take local variations into account. Nevertheless, the experimental values still show that the advantage of micro-patterning membranes is significant. The theoretical and modeling trends are the same for all gases and concentrations. Due to the fact that only single gases were measured experimentally, concentration polarization is non-existent here.

Table 1. Raw gas permeability data per individual micro-patterned membrane and averaged for all flat membranes.

Membrane	Δx [µm]	$J^{exp}\,\Delta x$ (N_2) [Barrer]	$J^{exp}\,\Delta x$ (He) [Barrer]	$J^{exp}\,\Delta x$ (O_2) [Barrer]	$J^{exp}\,\Delta x$ (CO_2) [Barrer]
Micro-patterned 1	27.8	22.8	53.2	43.8	265.9
Micro-patterned 2	28.8	20.8	47.4	47.0	266.1
Micro-patterned 3	30.4	18.8	49.0	46.2	223.0
Micro-patterned 4	34.7	19.2	48.1	49.6	288.4
Micro-patterned 5	37.6	20.4	52.4	50.7	304.4
Flat (average)	10.5 – 39.6	14.8 ± 1.8	36.0 ± 4.6	33.0 ± 4.3	188.4 ± 23.0

The raw permeability data for calculating the experimental advantage is given in table 1. The average selectivity of helium, oxygen and carbon dioxide over nitrogen are: He/N_2 = 2.50 ± 0.18, O_2/N_2 = 2.34 ± 0.31, CO_2/N_2 = 13.37 ± 2.13. These selectivities were found for both flat and micro-patterned membranes. The measured selectivity O_2/N_2 corresponds to similar block copolymers in literature (2.3 at 308 K for TPE 416 [7] and 2.8 at 303K for Kraton™ 1101 [8]). Other gas selectivities could not be found for this (type of) block copolymer.

3.3.3 Tensile stress

Tensile stress measurements were performed on flat and micro-patterned membranes to determine the mechanical strength. The micro-patterned membranes were measured both parallel (longitudinal) and perpendicular (transverse) to the line pattern. By micro-patterning with lines, the material becomes mechanically anisotropic: applying longitudinal strain yields higher tensile stresses than applying transverse strain. Straining a micro-patterned membrane on a 45° angle theoretically gives an average value between the longitudinal and transverse stress ($\sigma_{parallel}$ and $\sigma_{perpendicular}$, respectively). This relationship can be compared to fiber-reinforced materials with the fibers on an angle θ (equation 7) [9].

$$\sigma(\theta) = \sigma_{parallel} \cos^2(\theta) + \sigma_{perpendicular} \sin^2(\theta) \quad (7)$$

Table 2. Results of tensile stress measurements on flat and micro-patterned membranes in different straining directions.

Straining direction	Average σ at 5% strain [MPa]
Flat: all directions	0.98 ± 0.16
Micro-patterned: longitudinal	0.71 ± 0.08
Micro-patterned: 45° angle	0.61 ± 0.06
Micro-patterned: transverse	0.57 ± 0.04

Table 2 shows the average measured tensile stresses and their standard deviations per situation. When comparing flat membranes to micro-patterned membranes under longitudinal strain, one can conclude that micro-patterning results in a loss of stress of 28%. Theoretically it was expected to be 0%. At this moment we do not understand the reason for the loss of stress. A few possible explanations are discussed. The difference could originate from local variations in the thickness of the film. As the thickness is determined by SEM (a local technique), it is difficult to rule out variations. Another possibility could be differences in clamping the membranes into the set-up. The contact with the clamps on a micro-scale is different for a micro-patterned membrane compared to a flat membrane.

When applying transverse strain, the tensile stress is much lower than the stress for flat membranes (42% loss). A loss is expected as it is caused by a difference in stress-distribution. The stress during transverse strain is mostly located in the thin continuous film and not through the top part of the ridges.

The tensile stress for ridges under a 45° angle was also measured. According to equation 7 the theoretical stress at 45° should be in the middle between longitudinal and transverse straining (0.64 MPa). As seen from table 2, the value is close to this theoretical value.
These losses in mechanical strength are comparable to the losses of a film that has been reduced in thickness to reach the same increase in flux. Due to its anisotropy, however, the line pattern does not yield the optimal structure when mechanical strength is concerned. The most promising micro-pattern would probably be one with a continuous matrix like a honeycomb well pattern.

Figure 6. Schematic representation of the cross-section of a micro-patterned membrane (left) and a composite membrane (right) with the same dimensions.

3.3.4 Micro-patterning compared to composite membranes

When the pattern faces the permeate side, a micro-patterned membrane can also be seen as a continuous layer with a built-in (permeable) mechanical support. To verify if the micro-patterning is a good alternative for composite membranes, diffusive flux simulations are compared for both membranes (figure 6). All dimensions are similar to the ones in figure 2. The continuous layer has been varied from 5 to 85 µm.

Table 3. Calculations from simulations of the diffusive flux enhancement of a micro-patterned compared to a composite membrane.

Thickness continuous layer [µm]	Enhancement [%]
5	38.2
15	31.1
21	24.0
34.5	16.2
45	14.7
55	12.0
85	8.2

A comparison of calculated diffusive fluxes through micro-patterned and composite membranes shows an enhancement for the micro-patterned membranes (table 3). For a 5 µm thick continuous layer, the flux of a completely permeable membrane is almost 40% higher. The calculation of the enhancement is similar to equation 3.

Figure 7 shows the diffusive flux paths through both types of membranes. A rather simplified approach for calculating the effective diffusion length (l_{eff}) in a composite membrane is described by equation 8 [10]. This is a corrected version of the equation first published by Strathmann et al. [11, 12]. It assumes a linear diffusion path from the furthest point to the pore (l_{max}). The other parameters in the equation are: the porosity of the support layer (ε), the thickness of the selective layer (l_0) and the pore radius of the support layer (r). In this particular case the pore is the space between two ridges.

$$l_{eff} = \varepsilon l_0 + (1-\varepsilon)\frac{l_{\max} + l_0}{2} = \varepsilon l_0 + (1-\varepsilon)\frac{1}{2}\left[\sqrt{\left(r^2\,\frac{(1-\varepsilon)^2}{\varepsilon^2} + {l_0}^2\right)} + l_0\right] \qquad (8)$$

Finite element simulations (figure 7) show that the assumption of a linear diffusion path is incorrect. The diffusive flux streamline from the furthest point to the pore in the composite membrane is strongly curved. This indicates that the decrease in diffusive flux for the composite membrane is even more for the simulations than in the theory proposed in literature. The comparison of effective diffusion lengths (l_{eff}) calculated from equation 8 and from the simulations supports this statement: a membrane with a 5 µm thick continuous layer has a simulated diffusion path of 17.2 µm compared to 8.2 µm using equation 8. These results underline the importance of the lateral diffusion through the ridges. Therefore a micro-patterned membrane can (to some extent) be regarded as a composite membrane with a permeable support.

3.4 Conclusions

Micro-patterning one side of a flat membrane provides variations in thickness. Creating variations in diffusion paths through a dense gas permeation membrane has proven to increase overall gas permeation.

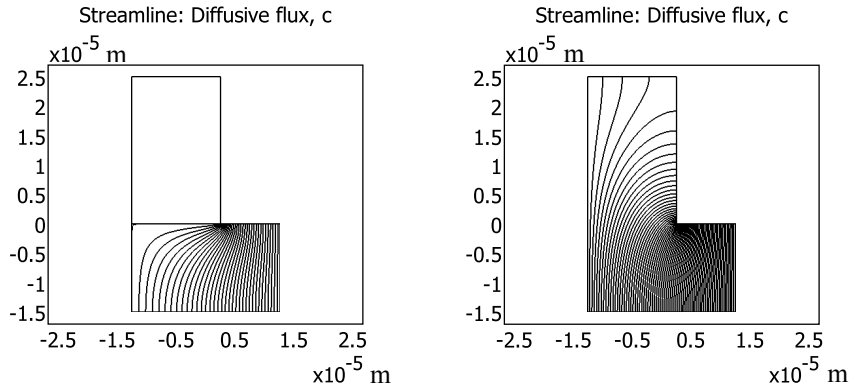

Figure 7. Diffusive flux streamlines of (left) a composite membrane with a very low permeable support layer (here on top) and (right) a completely permeable micro-patterned membrane. Gas concentration is high at the bottom and low on top.

Experimental gas permeability results of patterned membranes were compared to non-patterned membranes with the same effective thicknesses. Four different gases (nitrogen, helium, oxygen and carbon dioxide) were used. Under the same conditions, the patterned membrane showed an increase in gas permeability. Analytical calculations predicted an increase in flux for the micro-patterned membranes. The lateral flux was included in finite element simulations, which resulted in an even stronger enhancement. The experimental values fluctuated between these two calculations. In all cases, the enhancement becomes larger for thinner membranes. Selectivity values did not depend on the pattern of the membrane.

Thinner membranes have the disadvantage of becoming mechanically weaker. Micro-patterning limits the loss in mechanical strength by creating a geometry that is comparable to a composite membrane. Fluxes are enhanced significantly compared to the conventional composite membrane build-up if the support layer is of the same material as the separating layer. Due to its mechanical anisotropy the line pattern investigated in this paper is not the optimal structure in terms of membrane strength.

Although the experiments were performed with only one polymer and one pattern, micro-patterning is a general principle which is valid for all diffusion driven processes.

3.5 References

1. Ulbricht, M. *Polymer* **2006**, *47*, 2217-2262.
2. Gronda, A. M.; Buechel, S.; Cussler, E. L. *Journal of Membrane Science* **2000**, *165*, 177-187.
3. Nijdam, W.; de Jong, J.; van Rijn, C. J. M.; Visser, T.; Versteeg, L.; Kapantaidakis, G.; Koops, G. H.; Wessling, M. *Journal of Membrane Science* **2005**, *256*, 209-215.
4. Vogelaar, L.; Lammertink, R. G. H.; Barsema, J. N.; Nijdam, W.; Bolhuis-Versteeg, L. A. M.; van Rijn, C. J. M.; Wessling, M. *Small* **2005**, *1*, 645-655.
5. Bos, A. PhD thesis, University of Twente, 1996.
6. George, S. C.; Thomas, S. *Progress in Polymer Science* **2001**, *26*, 985-1017.
7. Yang, J. M.; Chian, C. P. C.; Hsu, K. Y. *Journal of Membrane Science* **1999**, *153*, 175-182.
8. Hsiue, G. H.; Yang, J. S. *Polymers for Advanced Technologies* **1996**, *7*, 686-692.
9. Ashbee, K. H. G. *Fundamental principles of fiber reinforced composites*; 1st ed.; Technomic Publishing Company, Inc.: Lancaster, 1989.
10. Peinemann, K.-V. XXI EMS summer school "Polymeric and inorganic membrane materials and membrane formation (including fuel cell membranes)", Geesthacht, Germany, 2004.
11. Strathmann, H.; Bell, C. M.; Gudernatsch, W.; Kimmerle, K. *Chemie Ingenieur Technik* **1988**, *60*, 590-603.
12. Strathmann, H.; Bell, C. M.; Kerres, J. *Desalination* **1990**, *77*, 259-278.

Chapter 4

Cassie-Baxter to Wenzel wetting transition: experiments

Surface hydrophobicity is partly determined by surface chemistry and can be extremely amplified by surface roughness. Liquid droplets suspended on rough surfaces can stay suspended and display very large contact angles and small contact angle hysteresis (Cassie-Baxter state). When suitable conditions do not persist, a transition to a lower energy state occurs (Wenzel state): the liquid is in contact with the whole surface below the drop leading to smaller contact angles and increased hysteresis. In this chapter, the transition on micro-patterned superhydrophobic polymer surfaces has been followed experimentally and numerically. Detailed analysis of the movement of the liquid during this transition reveals the wetting front velocity dependence on the geometry and surface properties. Considering a square array of square micro-pillars, a larger gap size between the pillars increases the front velocity, whereas an increase in pillar height and intrinsic material hydrophobicity leads to a decrease in front velocity. Also, signs of two different regimes are present: a zipping and a non-zipping regime. The movement of the liquid-gas interface is investigated in detail for the zipping regime. Two- and three-dimensional analysis is performed to investigate the complexness of the curvature during the different stages of the zipping motion.

The research for chapter 4 and 5 was performed in collaboration with the Physics of Fluids group. It has been published in the following three articles:

- M. Sbragaglia, A.M. Peters, C. Pirat, B.M. Borkent, R.G.H. Lammertink, M. Wessling and D. Lohse, Spontaneous breakdown of superhydrophobicity, Physical Review Letters, 99 (2007) 156001.
- C. Pirat, M. Sbragaglia, A.M. Peters, B.M. Borkent, R.G.H. Lammertink, M. Wessling and D. Lohse, Multiple time scale dynamics in the breakdown of superhydrophobicity, Europhysics Letters, 81 (2008) 66002.
- A.M. Peters, C. Pirat, M. Sbragaglia, B.M. Borkent, M. Wessling, D. Lohse and R.G.H. Lammertink, Cassie-Baxter to Wenzel state wetting transition: universal scaling of the front velocity, submitted to Langmuir (2008).

This chapter contains a selection of those articles, focusing on the experimental work.

4.1 Introduction

The interaction between water and a hydrophobic material has been of considerable interest during the past decade. In particular, much effort has been devoted to mimic nature's superhydrophobic properties [1-4]. This water repelling feature, also called the Lotus effect, is attributed to the material's intrinsic hydrophobicity and its surface roughness [5,6]. Liquid droplets can bead off with very low hydrodynamic resistance [7-11]. Such materials are useful for a wide series of applications ranging from anti-fog and anti-corrosion coatings to microfluidics [12-14].

To resemble the natural roughness of a superhydrophobic lotus leaf, micro-pillars are often used. In general, a drop of water on a rough or micro-patterned hydrophobic surface can have two states of contact (figure 1): suspended on a composite surface of material and air pockets (Cassie-Baxter state [15]) or in complete contact with the rough surface (Wenzel state [16]). For these two states the macroscopic contact angle and the contact angle hysteresis are different with respect to the flat hydrophobic surface. In the Cassie-Baxter state the apparent contact angle is the largest as the drop base is partly in contact with air. Due to the small solid-liquid contact area the hysteresis is very small and a liquid drop can roll off easily. In the Wenzel state the apparent contact angle is determined by the roughness of the material and the hysteresis is larger as the liquid is in complete contact with the solid surface.

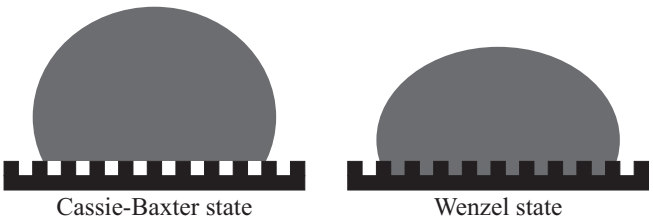

Figure 1. Illustration of a water drop on a regular micro-pattern in the Cassie-Baxter state (left) and the Wenzel state (right).

Although the Cassie-Baxter state is often seen as the state with the most advantages, the transition from the Cassie-Baxter state to the Wenzel state is in some situations highly desirable. An example is provided in the field of heterogeneous catalysis, where superhydrophobicity is an unwanted effect as it reduces the contact area of the liquid with the rough porous catalyst [17]. Understanding the mechanisms triggering the transition and charac-

terizing its dynamical properties is crucial. The triggering mechanisms for the transition are still debated in literature [18-20]. Theoretical analysis [18,21,22] has shown that the state with a smaller contact angle corresponds to a lower energy level. The presence of energy barriers between the two states may prevent a spontaneous transition and triggering is needed to induce the transition from the higher energy state to the lower energy state [9,10,20,23,24]. This can be achieved, for example, by pressing on the drop [9,10] or by using volumetric forces such as gravity [18-20]. Under certain conditions, local infiltrations due to coincidental excitement are seen. This does not necessarily mean that the liquid is able to spread to wet the whole surface between the micro-pattern. Whether the Wenzel state is reached depends on several parameters.

From experimental research based on micro-patterned surfaces, many design criteria have been proposed to control these two wetted states [25-31]. Geometry and surface properties can be tuned to either keep a liquid in the suspended state or wet the complete surface. Only recently, part of the dynamics of the wetting transition (from Cassie-Baxter to Wenzel) is described by observing the liquid-gas interface as it moves downwards along the pillars [23]. This approach describes the initial step of the wetting transition: the first contact of the liquid with the base of the micro-patterned surface between four pillars. In this chapter, the movement and velocity of the process following this initial step is investigated: the liquid-gas interface moves fast in lateral direction to fill the volume below the drop. The influence of several geometrical parameters and material properties on the liquid front velocity during this second step of the wetting transition is investigated. For different degrees of superhydrophobicity (reflected in the contact angle θ) the wetting front has been followed experimentally on various micro-patterns with different gap sizes a and pillar heights h.

4.2 Experimental

4.2.1 Micro-patterned surfaces

To observe the wetting transition, a regular square array of micrometer-sized square pillars is chosen. Fabrication of highly precise and controllable micro-patterned surfaces is possible through the micro-molding technique in this case followed by an evaporation or curing step (details in paragraph 2.5.3). Figure 2 shows a scanning electron microscopy (SEM) picture of a typical micro-patterned polymer film with square pillars in a square array. The geometrical parameters of the pattern are: pillar height h, pillar width w, gap size between the pillars a and wavelength $d = a + w$.

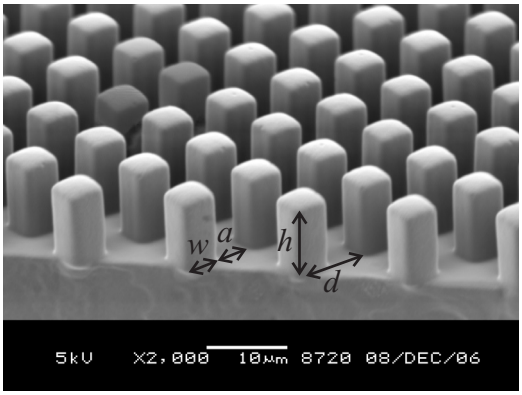

Figure 2. SEM picture of a micro-patterned polymer (Kraton^{TM} D-1102CS) film with pillar height h = 10 µm, gap size a = 5 µm, pillar width w = 5 µm and wavelength $d = a + w$ = 10 µm.

4.2.2 Molds

Molds were prepared in the cleanroom by standard photolithography and deep reactive ion etching on silicon wafers. Each mold contains fields (20 x 20 mm) filled with 5 µm wide square holes (w) in a regular square array with gap sizes between the holes (a) varying from 2 to 26 µm. Two mold types are defined in table 1: mold type 1 was used as is for replicating Kraton^{TM} films and mold type 2 was hydrophobized for an easy release of thin PDMS films.

The depth of the mold (equal to height h of the pillars) was also varied. Four copies of mold type 1 were etched to different depths: 4.4, 10, 14 and 15.6 µm. The final depths of two copies of mold type 2 were 4.7 and 8 µm. The result is a variety of gap sizes and pillar heights. The geometrical sizes were taken from scanning electron microscope pictures (5 kV, JSM 5600LV, JEOL) of the polymer films, not from the molds. Prior to imaging, the films were broken in liquid nitrogen and sputtered with a 30 nm gold layer (SCD 040, Balzers Union).

All molds of type 2 were coated with a hydrophobic FOTS coating (1H,1H,2H,2H-perfluorooctyltrichlorosilane, Fluka Chemicals). The coating procedure was as follows: a silicon wafer was placed in a large covered petridish with a drop of FOTS next to the wafer. The petridish was placed in an oven for 2 hours at 120 °C to evaporate the FOTS. It was cooled down to room temperature and then placed in an oven for 1 hour at 100 °C. The wafers were washed with isopropanol (analysis grade, Merck), MilliQ water and again isopropanol and dried under a flow of nitrogen.

Table 1. Gap sizes between the holes in the six different fields on mold types 1 and 2.

Field	Gap size *a* [µm]	
	Mold type 1 (Kraton)	Mold type 2 (PDMS)
1	2	16
2	5	18
3	8	20
4	11	22
5	14	24
6	17	26

4.2.3 Polymer film preparation

All materials were used as received. Two types of polymers were used for casting micro-patterned films: Kraton^{TM} D-1102CS (a linear styrene-butadiene-styrene block copolymer with 29.5 wt% styrene, Kraton Polymers) and PDMS (polydimethylsiloxane, RTV 615 rubber component A and curing agent B, GE Bayer Silicones).

The Kraton^{TM} was dissolved in toluene (analysis grade, Merck) to make a 30 wt% solution, which was stirred overnight. The solution was cast on an untreated mold (type 1) with a thickness of 200-300 µm. The toluene was allowed to evaporate overnight before releasing the micro-patterned film with ethanol (analysis grade, Merck). Films were dried and stored in a 30 °C vacuum oven until use.

To obtain a PDMS mixture, component A was mixed with curing agent B (10:1 w/w) and degassed before use. The liquid was cast on a hydrophobized mold (type 2) with a thickness of 100-300 µm and cured in an oven for 3 hours at 60 °C.

Each micro-patterned field was cut out and placed with its flat side on a 170 µm thick microscope slide before use.

4.2.4 Optical microscopy and high-speed imaging

Observations of the wetting transition are performed from the bottom through the patterned translucent film with an inverted optical microscope (Axiovert 40 CFL, Carl Zeiss BV). Proper illumination is obtained with a fiber lamp (ILP-1, Olympus). A high-speed charged coupled device camera (APX-RS, Photron Limited) is used for imaging. The large scale dynamics is captured with a 10x magnifying objective at 5-10 kfps. Smaller details are resolved at 50 kfps with an oil immersion Plan-Apochromat 100x objective (numerical aperture *NA* = 1.4) allowing for a thin image plane of 1 µm. Focusing in different planes is

achieved with a piezoelectric objective-lens positioning system with reproducibility below 100 nm (MIPOS 500, Piezosystem Jena GmbH).

4.2.5 Drop deposition

Water droplets are softly deposited on the micro-patterned surface with a syringe pump (PHD 2000, Harvard Apparatus GmbH) from the outlet of a vertical tube with an outer diameter of 1.6 mm at a very low flow rate (5 µl/min). The outlet is set at a height of 2 mm above the surface. A typical droplet grows slowly and reaches the dry surface within a minute after which the flow is stopped. A stable drop with a contact area ~ 1 mm^2 in the Cassie-Baxter state is observed.

In initial experiments the complete drop-base is placed on the array of pillars. Unfortunately, in this way the initiation time as well as the initial imbibition location is unpredictable. To control the initiation point and time of the transition, in later experiments the water drop is placed at the edge of the patterned area (figure 3). Initial spreading now occurs at the flat surface. For moderate values of the height, this procedure leads to similar front velocities as those obtained after a spontaneous imbibition by placing the drop completely on the pillars (compare the velocities for h = 10 µm in paragraph 4.3.2 with figure 7). This strategy allows us to collect data, also for those micro-patterns where no spontaneous imbibition could be observed with the initial method as the time until transition was longer than the evaporation time of the drop.

4.2.6 Post-processing

Sub-micrometer resolution of the wetting front is achieved with the help of a home-made image post-processing technique. First, a movie with region of interest (20 x 20 µm) is decomposed in an image sequence (VirtualDub 1.6.3, Avery Lee). For each image, the initial 117 x 117 pixels window undergoes a 10x oversampling up to 1170 x 1170 pixels. Next, a FFT bandpass filter consisting of a twofold two-dimensional (2D) Gaussian filtering in the Fourier space is applied. The low-pass component acts as a small structure smoothener, whereas the high-pass one corrects large scale illumination inhomogeneities and increases contour contrast. Finally, a proper adaptive intensity threshold is applied and the front position is detected. Attention should be paid to the fact that this method is sensitive to illumination variations through the image sequence, and may result from time to time in a slight shift of the detected front position. Moreover, shadowing caused by pillars yields an imprecise selection of the front position in the vicinity of the pillars, although the main part is accurately detected within 100 nm.

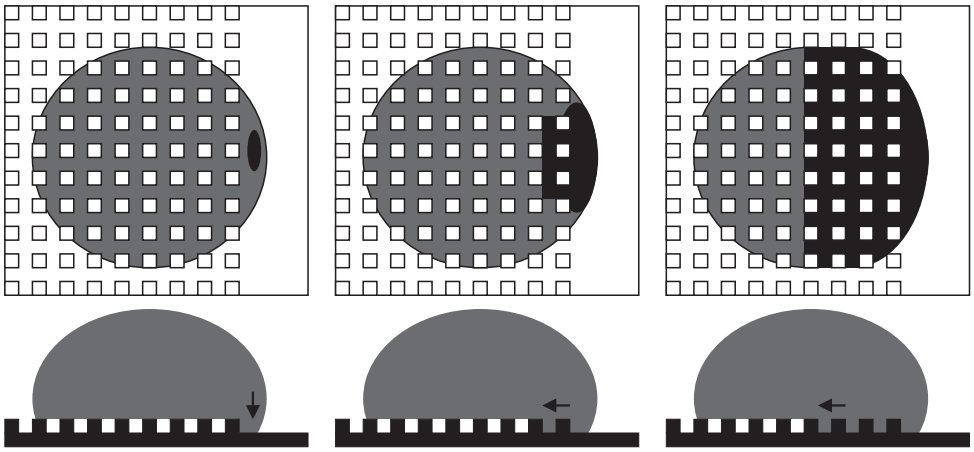

Figure 3. Illustration of the bottom and side views of a drop hanging over the edge of an array of pillars (not to scale). Left: the base of the drop touches the flat surface. Middle: the first row is filled. Right: the liquid is moving in between the pillars from the third to the fourth row.

4.2.7 Contact angle measurements

Contact angles of flat and micro-patterned films are measured with an optical contact angle measuring instrument (OCA 20, Dataphysics) by suspending a 6 µl water drop on the surface with a speed of 2 µl/s. After deposition, the drop is allowed to stabilize for 10 seconds prior to measuring.

4.2.8 Imaging with particles

For illustrative purposes, particle imaging is performed on one of the micro-patterned surfaces (Kraton^{TM}, a = 11 µm, h = 10 µm). A water droplet containing fluorescent polystyrene particles with a diameter of 0.3 µm (R300 red fluorescing microspheres, Duke Scientific Corporation) was followed during a spontaneous Cassie-Baxter to Wenzel state transition. The surface is illuminated by a dual-head Nd:YLF laser (527 nm, Pegasus-PIV, New Wave Research) through an inverted optical microscope (Axiovert 40 CFL, Carl Zeiss BV) with 63x magnifying objective. The frame rate of the high-speed APX-RS camera (Photron Limited) was set at 50,000 frames per second.

4.2.9 Numerical simulations

For the numerical simulations presented here, a 3D lattice Boltzmann [32-34] model for single-component multiphase flows is used. Its details are discussed in [35,36]. The geometrical aspect ratios of the micro-pattern can be adapted in order to match those typically

studied in the experiments [37] and wall interactions with wetting properties are introduced as explained elsewhere [35,36]. The initial conditions consist of a liquid reservoir on the top of the pillars and a wetted volume between four pillars characterized by a flat front perturbed with an advanced liquid precursor, just as experimentally observed at the onset of the transition in the initial measurements. In this way the liquid precursor induces a lateral motion that is continuously driven by capillary forces.

In all these mesoscale models, it is impossible to match all the physical parameters and at the same time preserve a feasible computation [38]. Typically, the width of the interface is too large and the liquid-gas density difference is unphysically small with respect to physical reality. As already noticed elsewhere [39,40], this may affect the speed of the interface. If directly proportional to the density difference it will move too fast in the simulations compared to experiments. This must be taken into account by renormalizing the time scale if one wants to reconstruct a correct pathway as a function of time [39,40].

4.3 Results and discussion

4.3.1 Contact angles and triggering

The static contact angle θ for water on a flat Kraton^{TM} film is 100° and on a flat PDMS film 120°. The contact angles for patterned Kraton^{TM} / PDMS films, respectively, with geometry a = 5 / 16 µm and h = 8 / 8 µm are: 160° / 157° (Cassie-Baxter state) and 142° / 137° (Wenzel state). The transition from the Cassie-Baxter state to the Wenzel state was captured macroscopically during a contact angle measurement (figure 4).

No intentional triggering was used for this transition. In this case the time between initial contact of the drop with the surface and the moment of transition is just over 4 s. As the time of delay is not equal for all measurements with constant drop sizes, a small study was performed to determine the cause of this time delay. Variations in temperature and pressure were ruled out. Another possibility could be the decay of material properties due to water vapor or UV radiation. Unfortunately no correlation can be found with any of these parameters. The process seems random under the existing working conditions (normal lab).

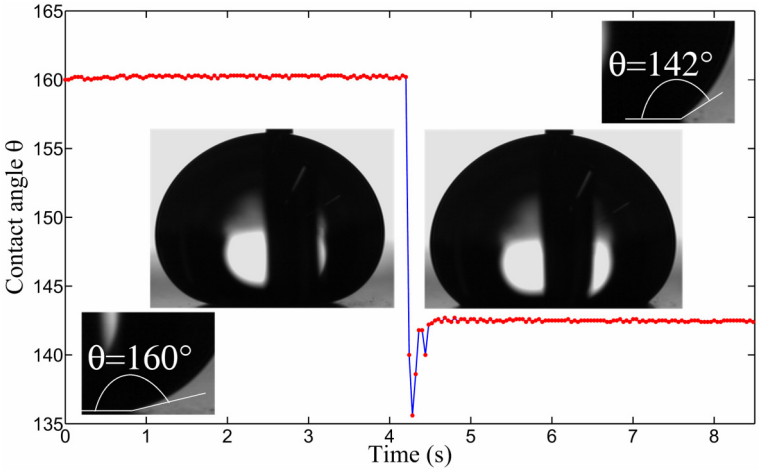

Figure 4. Contact angle measurement with a drop of water on a micro-patterned film made from Kraton™. The contact angle rapidly changes during the transition from the (meta)stable Cassie-Baxter state (left) to the Wenzel state (right).

4.3.2 Front velocity during transition

In figure 5 the time evolution of the filling process is shown. In this particular experiment the drop base is positioned completely on the micro-pattern. After the liquid initiates the transition at a certain point, lateral spreading develops, which sensitively depends on the geometrical parameters of the micro-patterned surface. For the larger gap size a = 11 µm (with pillar height h = 10 µm) a round shape of the wetted area is observed (figure 5c), while for a smaller gap size a = 5 µm the propagating fronts reflect the structure of the underlying square lattice, leading to a square-shaped wetted area (figure 5b). At even smaller a = 2 µm no transition to the Wenzel state is observed.

In order to reveal the physics of the wetting mechanism, numerical simulations were performed (for details see paragraph 4.2.9). Wetting properties are introduced via surface tensions [35,36], i.e. the wetting angles are comparable with those in the experiments. Geometrical structures are reproduced with the same aspect ratio as in the experiments. Similarly, for a = 11 µm circular wetted areas are observed (figure 5e), whereas for a = 5 µm square-shaped wetted areas appear (figure 5d).

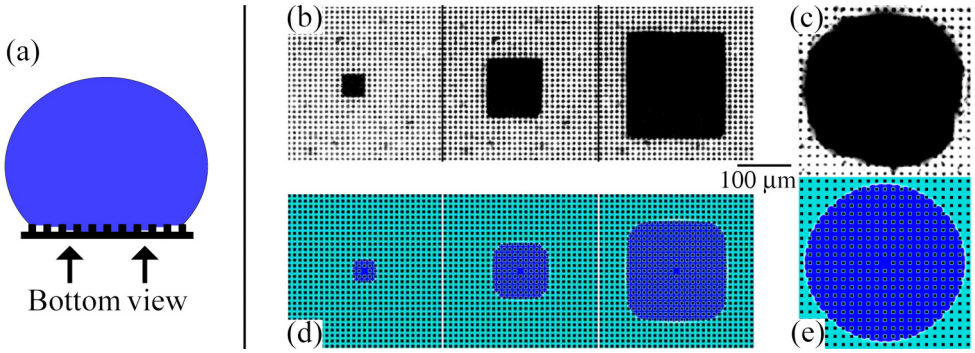

Figure 5. Bottom views of the front evolution of the transition as sketched in (a). In (b) three snapshots for the case with a = 5 µm and h = 10 µm are shown, leading to a square-shaped wetted area. In (c) it is a = 11 µm, resulting in a circular wetted area, (d) and (e) show the results of the corresponding numerical simulations with the lattice Boltzmann method with a = 5 and 11 µm, respectively. The imbibition point has been centered in the figure, but is not located in the center of the droplets base. The numerical simulations were performed by Mauro Sbragaglia.

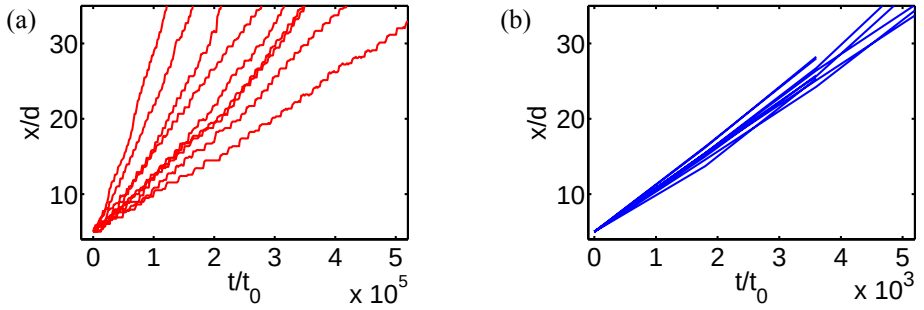

Figure 6. Wetting front evolution for two micro-patterned Kraton™ surfaces with pillar height h = 10 µm, but different gap size: a = 5 µm (a) and a = 11 µm (b). In both cases nine different experiments were carried out with the same sample. The position of the front x has been normalized with respect to the pattern wavelength $d = a + w$ and time has been made dimensionless with $t_0 = \eta\, h / \sigma_{lg} \sim 10^{-7}$ s.

To determine the influence of the geometry on the velocity of the front propagation, the position of the liquid front is followed in time. The front velocity v_{front} is defined as the distance x that the front travels from the first imbibition point in the outward direction divided by the time t it takes. For Kraton™, it drastically depends on the gap size a (figure 6): for a = 11 µm a mean velocity $v_{front} \sim 700$ mm/s is measured, two orders of magnitude faster than for the case with a = 5 µm, where $v_{front} \sim 7 – 30$ mm/s. Moreover, in the latter case the

front propagates in a stepwise manner (row by row filling, figure 6a) and front velocities show a remarkable variation ('dispersion').

For even smaller *a* experiments show that the transition does not occur at all. This dependence on geometry is further investigated by varying *a* as well as *h*. The influence of the material properties is determined by comparing Kraton™ with PDMS. The averaged front velocities are plotted in figure 7 (457 experiments in total). The data show that all three control parameters (*a*, *h* and *θ*) influence the front velocity significantly. As the gap size increases the velocity increases. For the same material and gap size the velocity decreases with increasing pillar height. For a given geometry the velocity is reduced as the material displays a larger contact angle (PDMS is more hydrophobic than Kraton™).

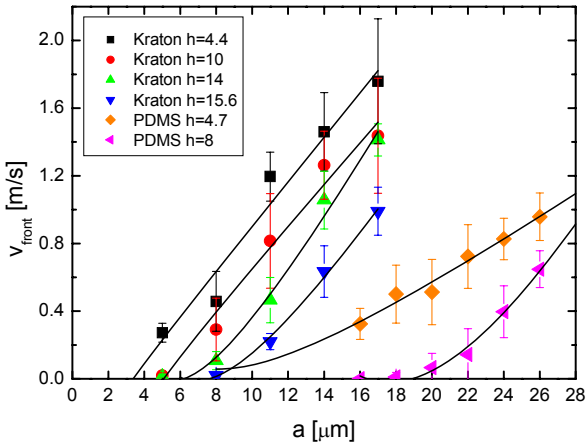

Figure 7. Front velocity v_{front} versus gap size *a* for Kraton™ ($\theta \approx 100°$) and PDMS ($\theta \approx 120°$) at different heights *h* (see legend). The lines are experimental fits.

4.3.3 Zipping motion

As described in paragraph 4.3.2, in some cases a stepwise propagation is prominently revealed. This motion has been described as the zipping mechanism [41-43]. This leads to a slowing down of the main front velocity and the emergence of dynamics with different time scales: the filling of a single row and the advancing towards the next row. Figure 8a shows details of the wetting dynamics for the case of the square-shaped wetted area in figure 5b (a = 5 μm). The main front is advancing from top to bottom and is slowing down while wetting occurs in a zipping manner (left to right). The time scale of the front moving

towards a new row can be determined from figure 6a, namely typically $t = d / v_{front} \sim 0.3 – 1.4$ ms, with d as the wavelength ($a + w$). The time scale for filling of the once entered row itself is one or two orders of magnitude faster, ~ 0.01 ms (figure 8c).

Under the same conditions, the zipping wetting behavior is reproduced numerically (figure 8b). When repeating the simulations for a gap size a = 2 µm, no lateral spreading occurs and the Cassie-Baxter state remains stable, just as observed experimentally.

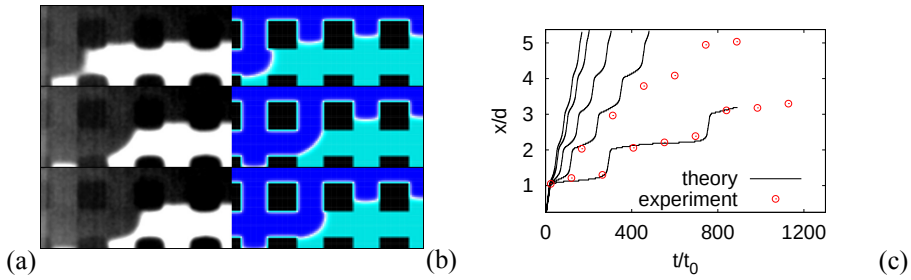

Figure 8. Lateral zipping mechanism (left to right) for small gap sizes. (a) Snapshots of the zipping mechanism recorded in an experiment with Kraton™ (a = 5 µm, h = 10 µm) with the front propagation from top to bottom. (b) Numerical results under the same conditions. (c) Numerical results for the front propagation (lines) in the lateral zipping process. From top to bottom we show the following cases: cos θ / cos $\theta_c \sim 0.868$, 0.890, 0.927, 0.945 and 0.971 (see paragraph 5.2.1 for an explanation of the critical contact angle). The geometrical aspect ratio for the simulations is chosen to be the same as in the experiment, which typical outcomes are also reported (circles). The numerical simulations were performed by Mauro Sbragaglia.

As mentioned, there are many typical features of the zipping regime: slow dynamics, stepwise filling leading to a square pattern and large dispersion in front velocity measurements on the same sample. To determine what characterizes this kind of dynamics, the experiments have been closely examined. Figure 9a shows the main front positions as a function of time in a typical experiment in the zipping regime. When the filled area is still small a transition to higher velocity occurs (also observed in the numerical simulations, but not shown). After this shift the front velocity is found to be v_{front} = 2.3 mm/s. Since v_{front} is almost constant and at the same time the square-shaped pattern remains, one may wonder how the zipping process adjusts. Figure 9b shows the probability distribution of the zipping velocity v_z involved to fill a row (perpendicular to the main front direction), processed over approximately 500 frames throughout the filling process. Interestingly, it shows a distribution with a significant dispersion. The large dispersion can be attributed to surface inhomogeneities resulting in a surface energy lowering (caused by defects or impurities).

Beyond the observed dispersion of the zipping velocity, it is worthwhile noticing that rows do not fill one by one continuously. A schematic picture of this is provided in the inset of figure 9c. When the filled square is still small (inset number 1), a sideway row fills at time t_2, and only then the next row starts to fill at time t_3 after a latency time ($t_l = t_3 - t_2 > 0$). The latency is decreasing with increasing square size until it finally vanishes at a square side length of about 270 µm (for this particular case). At this point in time, a different scenario is observed (inset number 2). The new row is already started at time t_2' before the former one has been completed. Completion of the first row happens at time t_3'. In this case, the latency time is expressed as $t_l = t_2' - t_3' < 0$. As a consequence, the filled area no longer be seen as a perfect rectangle although the macroscopic square-like shape remains, considering that the filled surface gets larger in four directions (see figure 5b). Moreover, the side length corresponding to $t_l = 0$ can simply be calculated from velocities by equation 1, which is in good agreement with the length extrapolated in figure 9c.

$$\frac{v_z^{\max}}{v_{front}} * d = \frac{62\,mm/s}{2.3\,mm/s} * 10\,\mu m \approx 270\,\mu m \qquad (1)$$

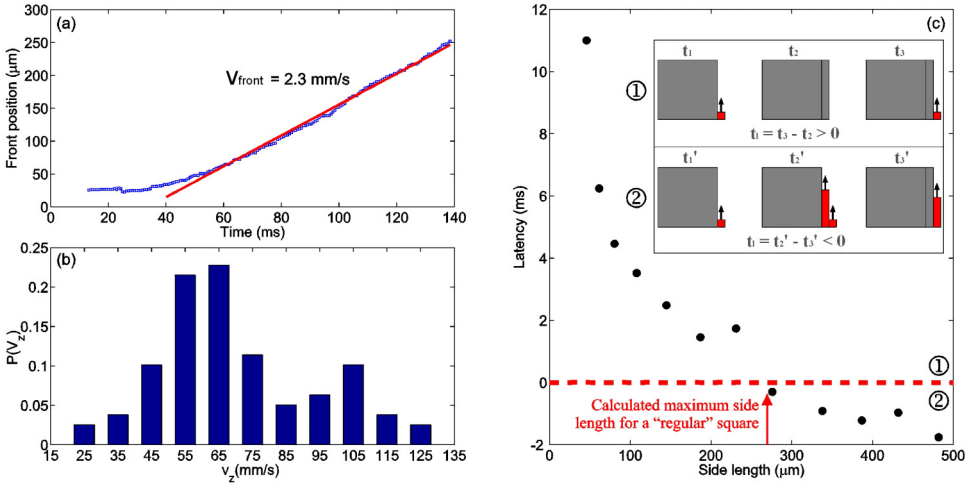

Figure 9. (a) Temporal evolution of the front position. Values have been averaged over the four sides of the square-shaped pattern, starting from its center. (b) Probability distribution of the zipping velocity v_z. (c) Measured latency as a function of side length (dots). Insets 1 and 2 sketch how positive and negative latencies have been calculated, respectively. The dashed line shows $t_l = 0$, which leads to a side length of 270 µm for a perfect rectangle at the intercept with the dots. This analysis was done by Christophe Pirat.

Details of the front advancing in between the posts are shown in figure 10a. The dynamics of the interface are captured in a plane close to the middle of the pillars. Based on the objective specifications, it is estimated to be at $z = 4 \pm 1$ µm from the base. The dynamics are processed from an experimental record chosen especially for its low v_z / v_{front} ratio to better reveal main and zipping front progressions at once. When averaged over the size of the observed area of 20 x 20 µm, the main front velocity (bottom to top) is v_{front} = 1.9 mm/s and the zipping velocity (left to right) is v_z = 10 mm/s.

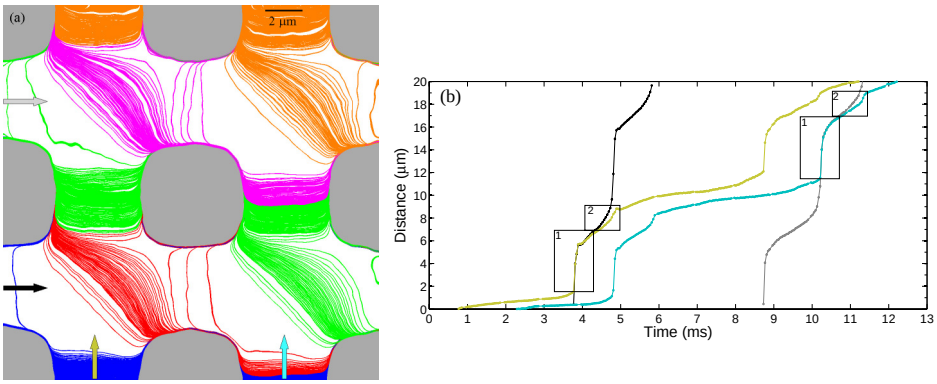

Figure 10. (a) Details of the zipping process in the experiment. Liquid-gas interface positions obtained every 20 µs are simultaneously drawn. The filling begins at the bottom left corner. The main front responsible for the macroscopic square shape is from bottom to top. The zipping front in a row to be filled is from left to right. Color changes after an interface has detached from a pillar (in chronological order: blue, red, green, pink and orange). (b) Interface position as a function of time along the four straight lines suggested by the arrows in (a). Curve and arrow colors match. Labeled rectangles correspond to different steps in the dynamics (see text). This analysis was done by Christophe Pirat.

The figure enables a comprehensive picture of the complex dynamics in the 2D plane: position and velocity variation of the interface are easily accessible. Unfortunately, the contact angle at the pillar walls is not described accurately. The walls seem to be hydrophilic instead of hydrophobic. As explained in paragraph 4.2.6, this problem is due to shadowing effects. The front and zipping interface positions as a function of time are quantitatively tracked in figure 10b along the straight lines passing through the middle of the four rows shown in figure 10a. First, the two perpendicular liquid-gas interfaces (defined as main and zipping front) spread between the pillars and reach the edge almost simultaneously. Next, they merge fast and the resulting interface straightens. Rectangles labeled 1 drawn in figure 10b highlight this stage. The main and zipping fronts are superimposed, indicating that

the interface at an intersection is almost symmetric. The merged front continues and adapts a lower velocity while an asymmetry develops: v_z increases more than v_{front} (rectangles labeled 2).

When the interface has reached the opposite post, it splits into two fronts that progress in the main and zipping direction, respectively, with drastically different velocities. The passage between the two pillars is made within 4 ms for the main front (black and grey line), whereas it is almost two orders of magnitude less for the zipping front (yellow and blue line).

4.3.4 Three-dimensional motion

So far the interface has been described in one plane, but since the filling is a 3D process, it is required that several planes should be analyzed simultaneously. Unfortunately this cannot be achieved experimentally. Therefore, numerical simulations have been carried out to better reveal the interface structure as well as the dynamics of the zipping mechanism.

Figure 11 is a frame of the resulting movie in which the liquid fills the volume between eight micro-pillars from top to bottom and from right to left. Only the liquid-gas interface (contoured area) in between the pillars is shown. The viewer is looking through the liquid as it pushes away the gas below the interface. The pillars are made transparent to visualize the three-phase contact line.

Figure 11. The curvature of the liquid-gas interface is visualized by numerical results performed in 3D. Liquid from the reservoir above pushes away the gas (below the contoured area) from top to bottom and right to left. The front pillars are made transparent. This numerical simulation was performed by Mauro Sbragaglia.

To be able to quantify the velocity of the liquid the planar view is still necessary. Figure 12 reports the movement of the interface for two wetting properties, $\cos\theta / \cos\theta_c = 0.868$ (a and b) and $\cos\theta / \cos\theta_c = 0.927$ (c and d), and at two different heights, $z / h = 0.3$ (a and c) and $z / h = 0.5$ (b and d). Zipping is advancing from left to right in these figures.

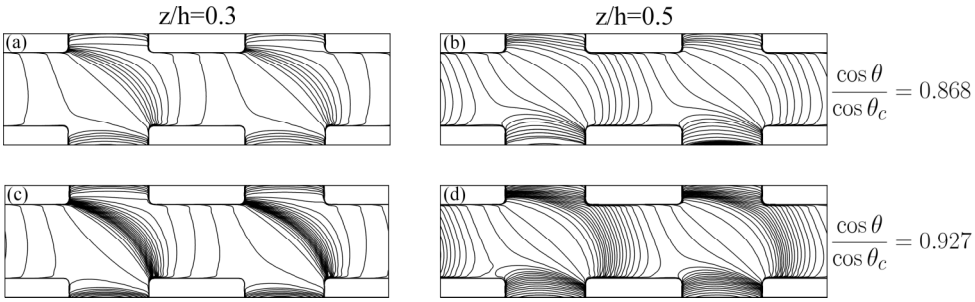

Figure 12. Numerical simulations reveal the details of the zipping mechanism. Two values of the wetting properties are used with respect to the critical contact angle given in equation 5 in chapter 5: $\cos\theta / \cos\theta_c = 0.868$ (a and b) and $\cos\theta / \cos\theta_c = 0.927$ (c and d). The interface position is tracked as a function of time (from left to right) as a given height z from the base of the pillars ($z / h = 0.3$ (a and c) and $z / h = 0.5$ (b and d)) and all plots are equispaced with the same numerical time lag. The numerical simulations were performed by Mauro Sbragaglia.

Comparing figures 12a and b (the same wetting properties, but at different heights) reveals a different behavior of the interface at different heights. When approaching the critical point (explanation in paragraph 5.2.1) the zipping is experiencing a slowing down followed by a rapid merging process (c and d). Capillary forces induce a complex curvature of the interface. An insight of this is provided by figure 11 and the cuts at different heights in figure 12. In particular, quantitative agreement is found with the experiments, assuming a height less than $h / 2$ ($z / h = 0.3$ in figure 12c).

The main steps of the zipping process are sketched in figure 13 and should be superimposed to the above figures. Starting with the case $z / h = 0.3$, the successive steps are described as numbered in figure 13:

1. Capillary forces draw the liquid between two pillars. At the red point in the corner of pillar A the main front interface merges with the zipping interface.
2. The liquid bridge suspended on the four pillars collapses at pillar A, producing a local top-to-bottom force. The dynamics is dominated by surface tension effects that tend to reduce the strongly curved surface of the merged interface, by drawing liquid from the top. Wall effects are negligible in this extremely fast process

(within 20 µs in the experiment): it is almost independent of the wetting properties (compare for example case b and d in figure 12).

3. Upon reaching the diagonal line a strong capillary force causes the interface to curve concave in the z-direction, while the interface is still pinned on the edges of pillars B and C (convex in the x-y plane). This creates a saddle-shaped interface with the liquid close to the top of the pillars ahead of the liquid close to the base. Viscous dissipation dominates, making the front much slower (time scale is ~ 1 ms in the experiment) compared to step 2.
4. The interface reaches pillar D and splits into two parts after which the filling progresses. The dynamics details are influenced by wall interactions that cause a slowing-down for the propagation. This is strongly pronounced especially when the wetting properties approach the critical point.

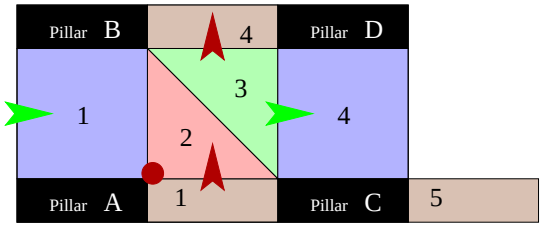

Figure 13. Sketch of the different steps in the zipping process. The numbers indicate areas with different front velocities (described in the text). The zipping front is again from left to right (green arrows), perpendicular to the main front (red arrows). This sketch was made by Christophe Pirat.

One has to remember that liquid is present in area 5, causing the interface that bridges over pillars C and D to be more curved than the one over pillars B and D (the portion beyond these pillars is not filled). This induces a faster filling in the zipping direction (green arrows in figure 13) than in the main front direction (red arrows). The front velocity between pillars C and D is progressively increased while the interface along pillar C is deformed by the existence of liquid in area 5 (figure 12d). It can be assumed that this effect is mainly at the base of the macroscopic square front and that the zipping velocity is quite sensitive to slight variations of the shape of the pillars top.

4.3.5 Particle imaging experiment

The results presented in figures 10, 11 and 12 reveal the complex structure of the zipping process, from both experimental and numerical point of view. First, the liquid interface merges fast with its neighbor, after which it experiences a passage along two pillar walls. Also, the profiles at different heights show curved liquid fronts. A micro-particle imaging experiment contributes to these findings by showing that the liquid mainly moves downwards while wetting. Figure 14a and b show two consecutive frames (n and n+1) of a movie with particles moving with the liquid that is wetting the micro-patterned film. In the time between frame n and n+1 (2 ms) the liquid has advanced towards the next row of pillars. This experiment is a nice example of a measurement in the zipping regime as it takes 36 ms before the front advances into the next row. Figure 14c is generated by subtracting frame (a) from frame (b) and displays the difference between the two frames. The first row is black, indicating that the particles located there did not move. Instead, additional particles are appearing from the out-of-focus liquid reservoir above the micro-pattern.

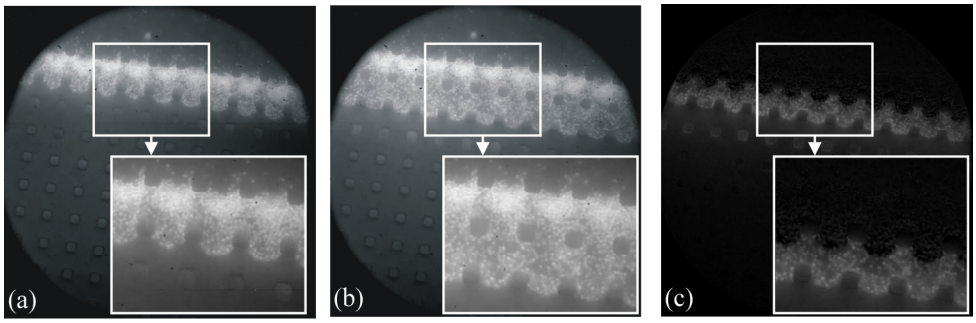

Figure 14. (a and b) Two stills with blow-ups from a particle imaging movie (two consecutive frames). (c) The difference between frames (a) and (b). The movie was made by Christophe Pirat.

4.4 Conclusions

This chapter describes the details of the spreading dynamics during the Cassie-Baxter state to the Wenzel state transition on a micro-patterned surface. This wetting transition is investigated experimentally and numerically by positioning a drop of water on a square array of square pillars. After initial imbibition of the liquid between four micro-pillars, a fast propagation of liquid in all four directions occurs.

The wetted area can show two distinct shapes as the liquid front propagates and fills up the rows between the pillars: square and more circular. The square shape occurs at low

gap sizes and preserves the shape of the micro-pattern array. In this regime a clear zipping mechanism is observed. Although the wetted area expands with a constant front velocity v_{front}, the zipping velocity v_z involved in filling up one row perpendicular to the main front direction undergoes a noticeable dispersion. This reveals the strong sensitivity of the dynamics to local wetting properties without prejudging the cause (roughness variation, geometrical imperfections, material inhomogeneity, dust deposits, etc). With increasing gap sizes this large dispersion disappears, the velocity increases and the liquid front fills up more than one row at a time (latency time t_l < 0 ms), resulting in a more circular wetted area.

Interested in the overall velocity of the liquid in general and the zipping dynamics in particular, the liquid front is followed in detail during the wetting transition. The geometry of the micro-pattern plays a large role in the overall front velocity of the wetting liquid. For a fixed pillar size and shape, the velocity increases with increasing gap size a and decreasing pillar height h. The liquid-solid interaction also plays a crucial role as the velocity increases dramatically with decreasing contact angle θ. For each series of parameters there was a critical point below which initial imbibition could take place, but spreading did not. Therefore no full transition could take place.

The dynamical details of the zipping interface in the x – y plane at different heights z demonstrate the complexity of the invasion process. The experimental observations are in very good agreement with numerical predictions for z / h = 0.3. Moreover, the numerical results shown for z / h = 0.5 give a deeper insight of the complex 3D stretching experienced by the liquid-gas interface.

Such a detailed description of the dynamics of the liquid and the velocities involved in the wetting transition process can be useful in tuning a liquid flow on the micro-scale. The velocity can be tuned in different directions or the whole wetting front can be stopped by means of geometry and material choice.

4.5 References

1. Quere, D. *Reports on Progress in Physics* **2005**, *68*, 2495-2532.
2. Feng, X.; Jiang, L. *Advanced Materials* **2006**, *18*, 3063-3078.
3. Li, X. M.; Reinhoudt, D.; Crego-Calama, M. *Chemical Society Reviews* **2007**, *36*, 1350-1368.
4. Li, X. M.; Reinhoudt, D.; Crego-Calama, M. *Chemical Society Reviews* **2007**, *36*, 1529-1529.

5. Barthlott, W.; Neinhuis, C. *Planta* **1997**, *202*, 1-8.
6. Neinhuis, C.; Barthlott, W. *Annals of Botany* **1997**, *79*, 667-677.
7. de Gennes, P.-G.; Brochard-Wyart, F.; Quere, D. *Capillarity and wetting phenomena: Drops, bubbles, pearls, waves*; 1st ed.; Springer Science & Business Media, Inc.: New York, 2003.
8. Quere, D. *Nature Materials* **2002**, *1*, 14-15.
9. Bico, J.; Marzolin, C.; Quere, D. *Europhysics Letters* **1999**, *47*, 220-226.
10. Bico, J.; Marzolin, C.; Quere, D. *Europhysics Letters* **1999**, *47*, 743-744.
11. Lafuma, A.; Quere, D. *Nature Materials* **2003**, *2*, 457-460.
12. Lauga, E.; Brenner, M. P.; Stone, H. A. In *Handbook of Experimental Fluid Dynamics*; Foss, J., Tropea, C., Yarin, A., Eds.; Springer: New-York, 2007.
13. Squires, T. M.; Quake, S. R. *Reviews of Modern Physics* **2005**, *77*, 977-1026.
14. Otten, A.; Herminghaus, S. *Langmuir* **2004**, *20*, 2405-2408.
15. Cassie, A. B. D.; Baxter, S. *Transactions of the Faraday society* **1944**, *40*, 546-551.
16. Wenzel, R. N. *Industrial & Engineering Chemistry* **1936**, *28*, 988-994.
17. Feng, L.; Li, S. H.; Li, Y. S.; Li, H. J.; Zhang, L. J.; Zhai, J.; Song, Y. L.; Liu, B. Q.; Jiang, L.; Zhu, D. B. *Advanced Materials* **2002**, *14*, 1857-1860.
18. Patankar, N. A. *Langmuir* **2003**, *19*, 1249-1253.
19. He, B.; Patankar, N. A.; Lee, J. *Langmuir* **2003**, *19*, 4999-5003.
20. Patankar, N. A. *Langmuir* **2004**, *20*, 7097-7102.
21. Marmur, A. *Langmuir* **2003**, *19*, 8343-8348.
22. Marmur, A. *Langmuir* **2004**, *20*, 3517-3519.
23. Moulinet, S.; Bartolo, D. *European Physical Journal E* **2007**, *24*, 251-260.
24. Kusumaatmaja, H.; Yeomans, J. M. *Bulletin of the polish academy of sciences: technical sciences* **2007**, *55*, 203-210.
25. Bico, J.; Thiele, U.; Quere, D. *Colloids and Surfaces A: Physicochemical and Engineering Aspects* **2002**, *206*, 41-46.
26. Li, W.; Amirfazli, A. *Advances in Colloid and Interface Science* **2007**, *132*, 51-68.
27. Barbieri, L.; Wagner, E.; Hoffmann, P. *Langmuir* **2007**, *23*, 1723-1734.
28. McHale, G.; Shirtcliffe, N. J.; Aqil, S.; Perry, C. C.; Newton, M. I. *Physical Review Letters* **2004**, *93*, 036102.
29. Yu, Y.; Zhao, Z. H.; Zheng, Q. S. *Langmuir* **2007**, *23*, 8212-8216.
30. Ishino, C.; Reyssat, M.; Reyssat, E.; Okumura, K.; Quere, D. *Europhysics Letters* **2007**, *79*, 56005.

31. Oner, D.; McCarthy, T. J. *Langmuir* **2000**, *16*, 7777-7782.
32. Benzi, R.; Succi, S.; Vergassola, M. *Physics Reports* **1992**, *222*, 145-197.
33. Succi, S. *The Lattice Boltzmann Equation*; Oxford University Press: Oxford, 2001.
34. Wolfe-Gladrow, D. *Lattice gas cellular automata and lattice Boltzmann model*; Springer Verlag: Berlin, 2000.
35. Benzi, R.; Biferale, L.; Sbragaglia, M.; Succi, S.; Toschi, F. *Physical Review E* **2006**, *74*, 021509.
36. Sbragaglia, M.; Benzi, R.; Biferale, L.; Succi, S.; Toschi, F. *Physical Review Letters* **2006**, *97*, 204503.
37. Dupuis, A.; Yeomans, J. M. *Langmuir* **2005**, *21*, 2624-2629.
38. Anderson, D. M.; McFadden, G. B.; Wheeler, A. A. *Annual Review of Fluid Mechanics* **1998**, *30*, 139-165.
39. Briant, A. J.; Wagner, A. J.; Yeomans, J. M. *Physical Review E* **2004**, *69*, 031602.
40. Kusumaatmaja, H.; Leopoldes, J.; Dupuis, A.; Yeomans, J. M. *Europhysics Letters* **2006**, *73*, 740-746.
41. Courbin, L.; Denieul, E.; Dressaire, E.; Roper, M.; Ajdari, A.; Stone, H. A. *Nature Materials* **2007**, *6*, 661-664.
42. Cubaud, T.; Fermigier, M. *Europhysics Letters* **2001**, *55*, 239-245.
43. Cubaud, T.; Fermigier, M. *Journal of Colloid and Interface Science* **2004**, *269*, 171-177.

Chapter 5

Cassie-Baxter to Wenzel wetting transition: theory

In the previous chapter the dynamics of liquid front was studied experimentally and numerically during the transition from the Cassie-Baxter state to the Wenzel state on polymeric micro-patterned surfaces. Two regimes were discovered: the zipping and the non-zipping regime. In this chapter, an attempt is made to theoretically describe the dynamics of this front. The energies involved in a small displacement of the liquid front in between two pillars are balanced leading to a description of the critical point for this specific geometry and an explanation of the divergence in the zipping regime. The energy balance is furthermore used to predict the liquid front velocity v_{front}. To achieve this, a universal scaling argument for the front velocities is necessary. Several scaling arguments for both the zipping and the non-zipping regime are proposed and tested against the experimental results to determine their universality. In the end, a universal scaling argument provides design criteria to control the liquid velocity locally by means of micro-patterning any material and will save experimental time.

The research for chapter 4 and 5 was performed in collaboration with the Physics of Fluids group. It has been published in the following three articles:

- M. Sbragaglia, A.M. Peters, C. Pirat, B.M. Borkent, R.G.H. Lammertink, M. Wessling and D. Lohse, Spontaneous breakdown of superhydrophobicity, Physical Review Letters, 99 (2007) 156001.
- C. Pirat, M. Sbragaglia, A.M. Peters, B.M. Borkent, R.G.H. Lammertink, M. Wessling and D. Lohse, Multiple time scale dynamics in the breakdown of superhydrophobicity, Europhysics Letters, 81 (2008) 66002.
- A.M. Peters, C. Pirat, M. Sbragaglia, B.M. Borkent, M. Wessling, D. Lohse and R.G.H. Lammertink, Cassie-Baxter to Wenzel state wetting transition: universal scaling of the front velocity, submitted to Langmuir (2008).

This chapter contains a selection of those articles, focusing on the theory behind the experiments described in chapter 4.

5.1 Introduction

The liquid dynamics during a Cassie-Baxter state to Wenzel state transition on a micro-pattern is described experimentally and numerically down to the sub-micrometer level in the previous chapter. The choice of geometrical (gap size *a* and pillar height *h*) and surface energy (intrinsic contact angle θ) parameters determines the velocity of the liquid front and can be used to tune the liquid flow precisely.

During the last decade a multitude of papers and book chapters have been published on the phenomenological approach to explain this wetting transition [1-7]. The interfacial energies of an advancing liquid are taken as a starting point to obtain design criteria for the possibility of a transition from the Cassie-Baxter state to the Wenzel state. This is generally expressed in terms of a critical contact angle θ_c (equation 1) [5]

$$\cos\theta_c = \frac{\varphi_s - 1}{r - \varphi_s} \tag{1}$$

with φ_s the fraction of liquid in contact with solid and *r* the roughness factor. A sketch of the energetically favorable superhydrophobic state on either side of this critical point is presented in figure 1. The contact angle for the flat surface θ is plotted against the apparent contact angle θ^*. Only the hydrophobic the side of the diagram is shown. The apparent contact angle represents either the contact angle for the Wenzel state (equation 2) or the Cassie-Baxter state (equation 3).

$$\cos\theta^* = r\cos\theta \tag{2}$$

$$\cos\theta^* = \varphi_s \cos\theta + \varphi_s - 1 \tag{3}$$

The dotted line represents a metastable regime for the Cassie-Baxter state [5].

In this chapter the dynamics of the liquid front observed in chapter 4 are discussed theoretically from a similar energy balance. The experimental data points of the front velocity for various micro-patterns and materials are rescaled. Multiple scaling routes for both regimes are investigated in order to have a universal scaling argument that can predict the front velocity of the spreading liquid under different experimental conditions.

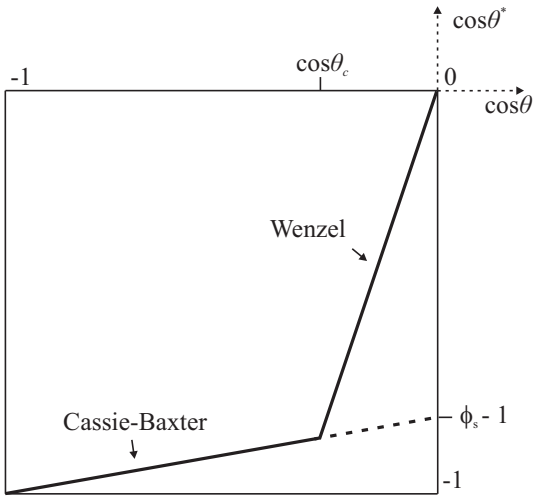

Figure 1. Sketch of the conditions under which the two superhydrophobic states are more favorable (adapted from [8]). For 90° < θ < θ_c the apparent contact angle θ^* should be given by the Wenzel model [9]. If θ_c < θ < 180° it is described by the Cassie-Baxter model [10]. The dotted line represents the metastable situation where the Cassie-Baxter state prevails despite the higher energy.

5.2 Theory behind the experiments

5.2.1 Energy balance between two pillars

The energy of a droplet in equilibrium on a substrate is monotonically increasing with the effective contact angle [6,11]. As a result, when the effective contact angle in the Cassie-Baxter state is higher than the one in the Wenzel state, a droplet in the Cassie-Baxter state would always collapse towards the Wenzel state. However, intermediate states with a higher energy can be encountered [6,11]. These energy barriers have to be overcome and therefore work has to be done in order to induce the transition [1,2,6,11]. The transition itself is a two-stage process: imbibition of the liquid between four pillars and lateral spreading between two pillars. The first stage is not examined in this thesis as the initial imbibition was random for the chosen experimental conditions (paragraph 4.3.1). The focus is on the second stage for which an energy balance for liquid propagation is written down below.

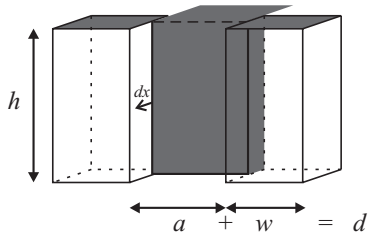

Figure 2. Illustration of a liquid front moving a small distance *dx* between two micro-pillars with height *h*, width *w* and gap size *a*. The contours of the advancing (dark grey) liquid-gas interface are highlighted: the thick black lines represent the wall contact and the dashed line the liquid-gas interface.

In the dynamics of liquid moving in between two pillars, both the free surface and wall interactions play a role (figure 2). A small advancing displacement $dx << a$ of the liquid-gas interface in between the pillars leads to a gain in surface energy due to the reduction of liquid-gas interface ($\sigma_{lg}\, a\, dx$) on the top of the pillars. Simultaneously, there is an energy loss to wet a small portion of the hydrophobic wall ($\sigma_{lg}\, (2h+a)\, dx \cos\theta$, with $\cos\theta < 0$). The overall energy change is

$$dE_s = \sigma_{lg} a dx + \sigma_{lg}\left(2h + a\right) dx \cos\theta \tag{4}$$

with σ_{lg} the surface tension of the liquid-gas interface. The limit $dE_s \rightarrow 0$ characterizes a critical point for the wetting properties. This critical point can be defined in different ways. In this chapter both the critical contact angle θ_c and the critical gap size a_c are used. For square pillars in a square array the equation is

$$\cos\theta_c = -1 + \frac{2h}{2h + a} \tag{5}$$

Note that in this equation there is no reference to the width *w* of the pillars because we describe the horizontal filling, different from a simultaneous vertical filling [6,7,11]. With this critical value, the energy gain (equation 4) can be rewritten as

$$dE_s = \sigma_{lg} a dx \left(1 - \frac{\cos\theta}{\cos\theta_c}\right) \tag{6}$$

where for $\cos\theta < \cos\theta_c$ with $\theta > 90^\circ$ no favorable propagation is expected, while in the other case, when $\cos\theta_c < \cos\theta < 0$, the propagation is energetically favored. For the two analyzed cases a = 5 and 11 µm we obtain θ_c = 101.54° and 110.78°, respectively. As it is easier for comparison to express the critical point in a geometrical parameter as the gap size a, equation 5 can be rewritten as

$$a_c = \frac{2h}{\cos\theta + 1} - 2h \tag{7}$$

For gap sizes between the pillars $a > a_c$ (with all other parameters fixed), front propagation after initial propagation is energetically favored, whereas for $a < a_c$ any front will stop.
The values for the critical gap size a_c for the different patterns described in chapter 4 are calculated using equation 7 and displayed in table 1. These critical gap sizes, below which the propagation to the Wenzel state is energetically not possible, can also be estimated from the experimental data (gap size at zero front velocity) by fitting each data set of figure 7 in chapter 4.

Table 1. Critical gap size calculated for different materials and pillar heights from equation 7 (theory) and from the data in figure 7 in chapter 4 (experimental fit).

Material	Pillar height (h) [µm]	Critical gap (a_c) (equation 7) [µm]	Critical gap (a_c) (experimental fit) [µm]
Kraton	4.4	1.9	3.4
	10	4.2	5.1
	14	5.9	6.2
	15.6	6.6	6.2
PDMS	4.7	9.4	8.2
	8	16	18.9

The critical slowing down of the liquid front at small gap sizes (figure 6 in chapter 4) can also be understood theoretically. A relevant time scale τ has to be identified and its fluctuations with respect to the geometry quantified. For that, the energy cost in terms of dissipation is estimated and compared with the change in surface energy of equation 6. With the small dimensions under consideration, flows can be regarded as laminar and viscous dissipation is dominating as compared to flow inertia. A simple estimate for the rate of viscous

dissipation per unit volume ε in a liquid with dynamical viscosity η is equation 8 [12] with $\dot{\gamma}$ as a characteristic shear rate.

$$\varepsilon \approx \eta \dot{\gamma}^2 \quad \text{with} \quad \dot{\gamma} \sim 1/\tau \tag{8}$$

If integrated over a small volume $dV = a\, h\, dx$ and time lag τ, the viscous contribution for the energy is obtained as

$$dE_d \approx \varepsilon \tau dV = \frac{\eta a h dx}{\tau} \tag{9}$$

Balancing dE_s in equation 6 with dE_d, we deduce the time scale

$$\tau = \frac{t_0}{\left(1 - \frac{\cos\theta}{\cos\theta_c}\right)} = \frac{\eta h}{\sigma_{lg}\left(1 + \cos\theta\left(\frac{2h + a}{a}\right)\right)} \tag{10}$$

with $t_0 = \eta\, h / \sigma_{lg} \sim 10^{-7}$ s for typical values of η, σ_{lg} and h = 10 µm and cos θ_c substituted by equation 5. Equation 10 reveals the origin of the critical slowing down of the front propagation, its dispersion, and the appearance of zipping. If $\theta \sim \theta_c$, the time scale of front propagation diverges as

$$\tau = \frac{1}{\left|\theta - \theta_c\right|} \tag{11}$$

Around this critical point, a small uncontrollable variation (imperfections of the micropattern, dust deposit) in the local wetting angle translates into a huge dispersion in the time scales, which is consistent with the experimental observation shown in figure 6a in chapter 4.

When the energy balance is favorable a flat front is allowed to proceed. Entering a new row perpendicular to the direction of the front can take up to milliseconds, whereas the row itself is filled on a faster time scale (zipping). In this way a square-shaped propagating wetting pattern emerges (see figure 5b in chapter 4, where $\theta \sim 100°$ and $\theta_c \sim 101.54°$). When approaching the other limit cos θ / cos θ_c << 1 (more alike figure 5c in chapter 4, where $\theta \sim$

100° and θ_c ~ 110.78°) the dynamics becomes more and more determined by the time scale t_0 itself (figure 6b in chapter 4) and the propagation through the pillars is expected to be smooth. In this limit, it is the pure pulling mechanism of surface tension in equation 6 that dominates the spreading dynamics and it is prevalent over the wall effects [13]. For this reason, the geometrical properties of the lattice do not emerge and the front assumes an almost circular shape.

5.3 Scaling theory and discussion

5.3.1 Scaling of data: unitary cell approach

To be able to predict the front velocity on other materials or geometries, the experimental data points (figure 7 in chapter 4) need to be rescaled to obtain one universal curve. Based on the knowledge that there are two different regimes (zipping and non-zipping), the presence of multiple scaling arguments is expected, each valid for their own regime.

To obtain a global front velocity, an argument valid for the unit cell of the micro-pattern can be defined. The unit cell is characterized by the sum of the volume between two pillars (volume A in figure 3) and the volume beyond the pillars (volume B). In order to derive scaling arguments with this unitary cell approach the energy equations above have to be reformulated. The difference in surface energies before and after wetting ΔE_s (equation 4) can be rewritten as

$$\Delta E_s = \sigma_{lg}\left(d^2 - w^2\right)\left(1 + \cos\theta\left(\frac{d^2 - w^2 + 4wh}{d^2 - w^2}\right)\right) \tag{12}$$

with wavelength d , pillar width w and pillar height h. This energy gain has to be balanced with the time integral of the dissipation in the unit cell that is estimated with the volume integral of the velocity shear rate, estimated as v / l

$$\Delta E_d \approx \int dV \eta \frac{v}{l} = h\left(d^2 - w^2\right)\eta \frac{v}{l} \tag{13}$$

with ΔE_d the energy for viscous dissipation, $h(d^2 - w^2)$ the volume of the unit cell, v a characteristic velocity and l a characteristic length scale. The definition of l is crucial to understand the way the front velocity scales as a function of geometry and material properties [14]. Chapter 4 shows that a complex 3D filling dynamics including strong spatial anisot-

ropies is present. It is expected that the shear rate is dominated by the vertical direction ($l \approx h$) when the gap size a is much larger than the pillar height h. In the other limit ($a << h$) the shear rate is gap-dominated ($l \approx a$). Due to the presence of the critical point it is difficult to do experiments with gap sizes much smaller than the pillar height. The gap is usually larger than or comparable to the pillar height and therefore $l \approx h$ is introduced in equation 13. Balancing equations 12 and 13 with $l \approx h$ leads to the front velocity as a function of geometry and wetting properties, which can be written as the dimensionless capillary number Ca.

$$Ca = \frac{\eta v}{\sigma_{lg}} \approx \left(1 + \cos\theta \left(\frac{d^2 - w^2 + 4wh}{d^2 - w^2} \right) \right) \tag{14}$$

This averaged capillary number is a measure of the averaged viscous forces per unit length (ηv) against the capillary forces per unit length (σ_{lg}). This scaling argument is not generally valid though. A simple estimate of the viscous integral as in equation 13 does not take local variations in velocity into account. In the zipping regime ($a \approx a_c$), the overall front velocity v_{front} can actually include two time scales: τ_1 and τ_2 with $\tau_1 << \tau_2$ (paragraph 4.3.3). τ_1 Equals the time needed to propagate in between two pillars and τ_2 equals the time needed to fill up the next row (figure 3). This difference in time scales results from the slowing down of the overall front propagation near the critical point. Previously, only τ_1 was derived by matching surface energy with viscous dissipation between the pillars of subcell A (τ in equation 10).

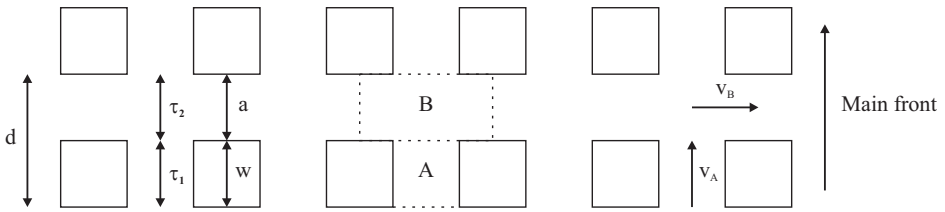

Figure 3. Illustration of the top view of twelve pillars with wavelength d (gap size a + pillar width w), timescales τ_1 and τ_2 and velocities v_A and v_B. The dotted lines mark the unit cell with subcells A and B.

5.3.2 Scaling of data: two subcell approach

To generate valid scaling arguments for different regimes, the unit cell can be treated as two subcells (figure 3): one between the pillar walls (A) and one beyond the pillars (B). In each cell a characteristic front velocity is assumed (v_A and v_B with v_B perpendicular to v_A).

Reformulating the surface energy gain and balancing that with the relative energy dissipation separately for subcell A and subcell B leads to

$$awh\eta\frac{v_A}{h}=\sigma_{lg}aw\left(1+\cos\theta\left(\frac{2h+a}{a}\right)\right) \tag{15}$$

$$adh\eta\frac{v_B}{h}=\sigma_{lg}ad\left(1+\cos\theta\left(\frac{2wh+da}{da}\right)\right) \tag{16}$$

Rewriting these equations results in a capillary number for each subcell:

$$Ca_A=\frac{\eta v_A}{\sigma_{lg}}=\left(1+\cos\theta\left(\frac{2h+a}{a}\right)\right) \tag{17}$$

$$Ca_B=\frac{\eta v_B}{\sigma_{lg}}=\left(1+\cos\theta\left(\frac{2wh+da}{da}\right)\right) \tag{18}$$

It can be shown that $Ca_A \le Ca_B$ ($v_A \le v_B$) is generally valid for a hydrophobic surface ($\cos\theta < 0$) since

$$\frac{2h+a}{a}\ge\frac{2wh+da}{da} \quad \text{as} \quad d\ge w \quad \text{because} \quad d=a+w \tag{19}$$

The conclusion is that filling up subcell B is never slower than filling up subcell A. In the zipping regime this difference in filling velocity between the two subcells is clearly observed. Volume B is filled much faster than volume A. Near the critical point the front between the pillars almost stops when the next row is filled. In this limiting case ($\cos\theta = \cos\theta_c$) the capillary numbers become

$$Ca_A=\left(1+\left(-\frac{a}{2h+a}\right)\left(\frac{2h+a}{a}\right)\right)=0 \tag{20}$$

$$Ca_B=\left(1+\left(-\frac{a}{2h+a}\right)\left(\frac{2wh+da}{da}\right)\right)=\left(1-\left(\frac{2wh+da}{2wh+da+2ha}\right)\right)>0 \tag{21}$$

The mechanism of advancing is therefore determined by a movement in subcell A.
By treating the two subcells separately, scaling arguments in the limiting regimes (zipping and non-zipping) can be identified. The front velocity is evaluated in a unidirectional way: the filling is followed along a line between two rows of micro-pillars in the main front direction (figure 3). The front velocity is thus defined in terms of distance that the front travels to fill up volume A and B, divided by the time it needs for that

$$v_{front} = \frac{d}{\tau_1 + \tau_2} \sim \frac{d}{\tau_A + \tau_B} \tag{22}$$

with τ_A the time scale corresponding to velocity v_A ($\tau_1 = \tau_A$) and τ_B to velocity v_B ($\tau_2 \sim \tau_B$).
From here on we separate the two limiting regimes. In the zipping regime ($a \approx a_c$) time scale τ_A is much larger than time scale τ_B due to its divergence as stated before. The overall front velocity is therefore dominated by time scale τ_A. This time scale can be described as $\tau_A = w / v_A$ and can be combined with equation 15 for subcell A. The resulting equation for the front velocity in the zipping regime is therefore

$$v_{zipping} \sim \frac{d}{\tau_A + \tau_B} \approx \frac{d}{\tau_A} = \frac{\sigma_{lg}}{\eta}\frac{d}{w}\left(1 + \cos\theta\left(\frac{2h + a}{a}\right)\right) \tag{23}$$

This scaling argument can be rewritten in dimensionless terms as

$$Ca_{zipping} \sim \frac{d}{w}\left(1 + \cos\theta\left(\frac{2h + a}{a}\right)\right) \tag{24}$$

In the non-zipping regime a is much larger than a_c and the large scale wetting pattern is more circular. This imposes that velocities v_A and v_B are almost comparable, which gives

$$\frac{w}{\tau_A} \approx \frac{a}{\tau_B} \tag{25}$$

When the same steps are followed as for the zipping regime, the overall non-zipping velocity is

$$v_{non-zipping} \sim \frac{d}{\tau_A + \tau_B} \approx \frac{d}{\tau_A + \frac{a}{w} \cdot \tau_A} = \frac{\sigma_{lg}}{\eta}\left(1 + \cos\theta\left(\frac{2h + a}{a}\right)\right) \quad (26)$$

and as a dimensionless scaling argument

$$Ca_{non-zipping} \sim \left(1 + \cos\theta\left(\frac{2h + a}{a}\right)\right) \quad (27)$$

Equations 24 and 27 express the core of the scaling results, predicting a scaling behavior for the capillary number as a function of the geometry (*h* and *a*) and wetting properties (*θ*). From both scaling proposals we observe that an increase in *a* (for fixed *h* and *θ*) produces an increase in capillary number *Ca* (increased velocity). An increase in *h* (for fixed *a* and *θ*) produces a decrease in *Ca*. These observations match the trends in the experimental data (figure 7 in chapter 4). To assess the accuracy of equations 24 and 27 the scaling arguments are applied to the experimental data. In figure 4a the rescaling for the zipping regime (equation 24) is displayed. An excellent degree of collapse is observed for small gap sizes, where the zipping mechanism is expected to dominate. For larger gap sizes (lower left corner of figure 4a), where the filling is expected to be less influenced by the zipping mechanism, the proposed scaling argument still provides a good collapse of data. Rescaling according to the non-zipping equation (equation 27) did not result in collapse of data (figure 4b).

At larger gap sizes, the experiments give the impression that the wetting is governed by a non-zipping motion. At first, the wetted area seems to be circular on a large scale (figure 5a), but enhancing the contrast shows that a step-like contour is present at the liquid front (figure 5b). From figures 4 and 5 we can conclude that the front velocity for all these experimental values is dominated by the zipping motion. Apparently, the gap size needs to be even further away from the critical gap size to reach the non-zipping regime. It is difficult to follow the liquid front on micro-patterns with much larger gap sizes experimentally as the velocity is too large to capture the front in detail.

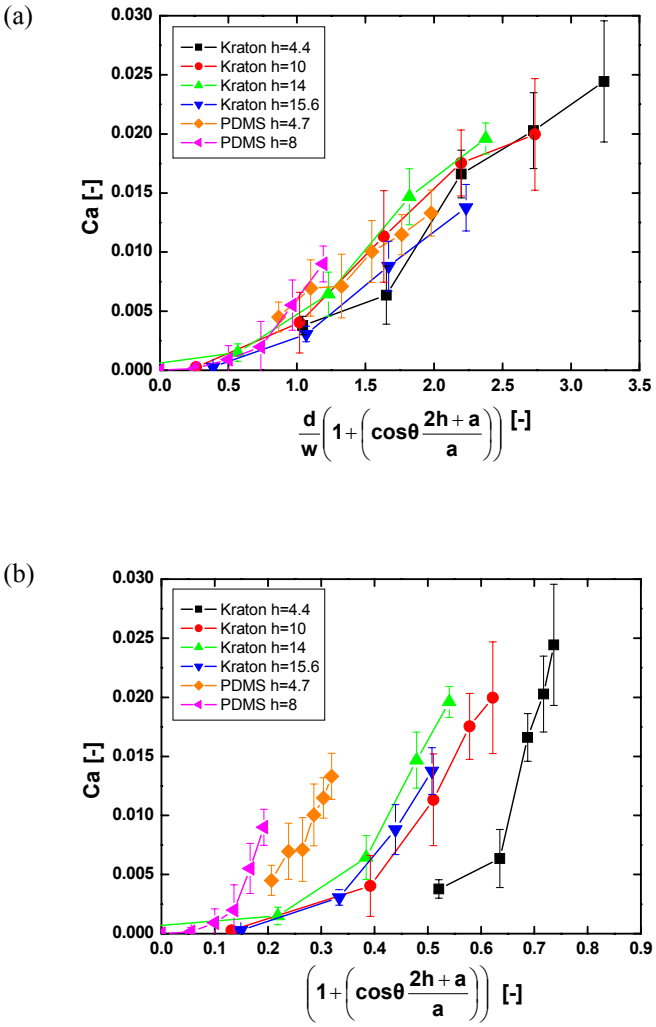

Figure 4. Dimensionless front velocity *Ca* versus the scaling factor, which should give a universal curve in the zipping regime according to (a) equation 24 or (b) equation 27 (same data as in figure 7, chapter 4). Lines are for guidance only.

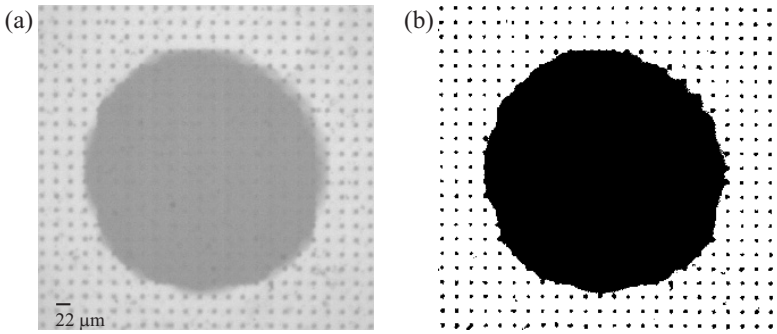

Figure 5. (a) Original image of one frame during the wetting transition on a micro-patterned Kraton™ surface with *d* = 22 µm and *h* = 10 µm. (b) The same image with enhanced contrast.

5.3.3 Varying the characteristic length scale

Apart from balancing capillary effects with viscous dissipation within the subcells, the other crucial assumption made in deriving the scaling arguments is the definition of the characteristic length scale *l* related to the shear rate. It is instructive to compare the previously proposed scaling equations (24 and 27) to the equations found when a horizontal length scale (e.g. *w*) is used for *l* instead of a vertical one (*h*) in the term *v* / *l* of equation 13. If done so and if the same arguments for the two regimes as before are used, one arrives at the following equation for the zipping regime

$$Ca_{zipping} \sim \frac{d}{h}\left(1+\cos\theta\left(\frac{2h+a}{a}\right)\right) \tag{28}$$

and for the non-zipping regime

$$Ca_{non-zipping} \sim \frac{w}{h}\left(1+\cos\theta\left(\frac{2h+a}{a}\right)\right) \tag{29}$$

When these scaling arguments are applied to the experimental data, neither one provides a master curve comparable to figure 4a (figure 6).

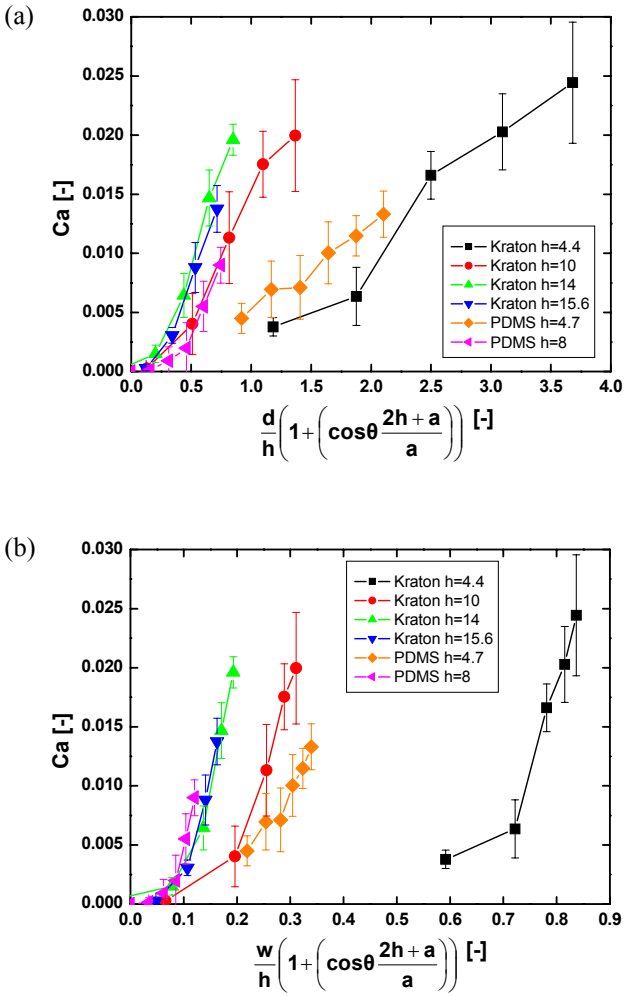

Figure 6. Dimensionless front velocity *Ca* versus the scaling factor, which should give a universal curve in the zipping regime according to (a) equation 28 and (b) equation 29 (same data as in figure 7, chapter 4).

5.4 Conclusions

A universal scaling argument was developed for the experimentally measured liquid front velocity during the wetting transition of the Cassie-Baxter state to the Wenzel state. To explore the dynamics of this transition, several superhydrophobic micro-patterned polymeric surfaces were studied. The geometry (pillar height and gap size) and material properties (hydrophobicity) of these surfaces with square micro-pillars in a square array were varied extensively. The velocity of the wetting front was measured. In the experiments a critical point was observed, below which no transition occurs. By balancing energies involved in the wetting process, a theoretical equation is derived for the critical point, containing all varied parameters. The results match the experimental observations.

Several theoretical approaches to obtain a universal scaling argument for all data points have been examined. The argument derived from a balance of surface energies and viscous dissipation energy using a unitary cell approach is not generally valid when local variations in the velocity are present. This is the case in the zipping regime. Reformulating the energy balance via a two subcell approach leads to generally valid equations for the zipping and the non-zipping regime. The experimental front velocities collapse perfectly when the scaling argument for the zipping regime is used, derived with the height of the pillar as a characteristic length scale for the shear rate (equation 24). There is no universal curve present when the scaling argument for the non-zipping regime is used. The conclusion is therefore that all measured front velocities are governed by a zipping liquid motion.

These scaling arguments provide design criteria to tune the liquid velocity precisely on a micro-scale level without having to perform many experiments. Future work can be devoted to exploring its practical use in the field of microfluidics, in particular by experimenting with other geometries and arrays of decreasing gap sizes.

5.5 References

1. Bico, J.; Marzolin, C.; Quere, D. *Europhysics Letters* **1999**, *47*, 220-226.
2. Bico, J.; Marzolin, C.; Quere, D. *Europhysics Letters* **1999**, *47*, 743-744.
3. Bico, J.; Tordeux, C.; Quere, D. *Europhysics Letters* **2001**, *55*, 214-220.
4. Bico, J.; Thiele, U.; Quere, D. *Colloids and Surfaces A: Physicochemical and Engineering Aspects* **2002**, *206*, 41-46.
5. Lafuma, A.; Quere, D. *Nature Materials* **2003**, *2*, 457-460.
6. He, B.; Patankar, N. A.; Lee, J. *Langmuir* **2003**, *19*, 4999-5003.

7. de Gennes, P.-G.; Brochard-Wyart, F.; Quere, D. *Capillarity and wetting phenomena: Drops, bubbles, pearls, waves*; 1st ed.; Springer Science & Business Media, Inc.: New York, 2003.
8. Quere, D.; Lafuma, A.; Bico, J. *Nanotechnology* **2003**, *14*, 1109-1112.
9. Wenzel, R. N. *Industrial & Engineering Chemistry* **1936**, *28*, 988-994.
10. Cassie, A. B. D.; Baxter, S. *Transactions of the Faraday society* **1944**, *40*, 546-551.
11. Patankar, N. A. *Langmuir* **2003**, *19*, 1249-1253.
12. Landau, L. D.; Lifshitz, E. M. *Fluid mechanics*; 2nd ed.; Pergamon: London, 1959.
13. Cubaud, T.; Fermigier, M. *Europhysics Letters* **2001**, *55*, 239-245.
14. Ishino, C.; Reyssat, M.; Reyssat, E.; Okumura, K.; Quere, D. *Europhysics Letters* **2007**, *79*, 56005.

Chapter 6

Slip experiments with dense and porous micro-patterned films

Superhydrophobicity can lead to significant advantages in hydrodynamical applications as flowing liquid in the Cassie-Baxter state generates slip. Micro-grooves on the bottom of a polymeric micro-channel show local slip lengths up to 3 μm. Micro-patterned dense (PDMS) and porous (PVDF) surfaces are prepared via the casting technique. Velocity profiles of water flowing along these surfaces are investigated by micro-particle image velocimetry. The observed slip coefficients support the possibility of reducing concentration polarization in a membrane process.

The research for this chapter was performed in collaboration with Peichun Amy Tsai of the Physics of Fluids group. This chapter will also be published as a paper:

- P. Tsai, A.M. Peters, C. Pirat, R.G.H. Lammertink, M. Wessling and D. Lohse, Quantifying effective slip length over micropatterned hydrophobic surfaces, in progress.

6.1 Introduction

Interfaces of a system are usually of particular interest, as transport processes can slow down or accelerate immensely at those interfaces. Common examples in engineering are heat transfer, charge build-up and mass transfer (e.g. concentration polarization). In the field of fluid dynamics the importance of the boundaries is no exception. The behavior of liquid at a solid surface has been a topic of interest for almost two centuries since the concept of a slip boundary condition was first proposed by Claude Navier in 1823 [1]. The proposed boundary condition (equation 1) assumes that the tangential component of the fluid velocity u at a solid surface is proportional to the shear rate at that surface $\eta\, \partial u / \partial z$ via the proportionality factor β.

$$\eta \frac{\partial u}{\partial z} = \beta u \tag{1}$$

On the macroscopic scale, the steady state velocity profile between two parallel plates, in a rectangular channel or in a pipe driven by a pressure gradient is described with a parabolic equation (figure 1a). For flow in a cylindrical pipe it is known as the Poiseuille equation [2]. Locally, at the walls, three types of boundary conditions can be distinguished: (b) no-slip, where a layer of stagnant liquid is present at the solid-liquid boundary ($u_{x,0}$ = 0), (c) partial slip and (d) full slip. The amount of slip can be quantified by the slip length b (equation 2) [3-8] or δ [9-11]. This value is defined as the depth below the liquid-solid boundary when the profile is extrapolated to zero velocity. Another way of expressing the amount of slip is calculating the slip velocity at the wall $u_{x,0}$ [3].

$$u_{x,0} = b \frac{\partial u_x}{\partial z} \tag{2}$$

Traditionally, slip occurs in three different contexts [12]: gas flows, non-Newtonian fluids and contact line motion. The last decades many studies have been performed with Newtonian fluids. Focus has been on surface roughness [7,11], flow along a gas interface (nano- or micro-patterned surfaces) [3,4,8,9,13-15], nanobubbles on smooth surfaces [16] and charged surfaces [17].

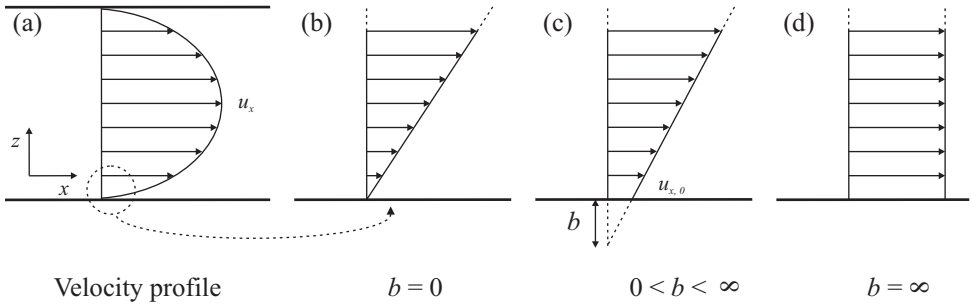

Figure 1. (a) Illustration of a cross-section of a channel with a parabolic velocity profile and two no-slip boundaries. (b-d) Velocity profile at the wall with no-slip (b = 0), partial slip (finite b) and full slip (infinite b) conditions, respectively.

Advancing technologies, such as surface force apparatus and (high-speed) imaging techniques, have made it possible to investigate both surface structure and dynamics at these very small length scales [12,18,19]. Overall slip can be determined by: (1) applying a constant pressure drop and measuring the flow rate [10] or vice versa [3,4], (2) imposing the steady or oscillatory motion and measuring the resistive force [11,15,20-22], (3) measuring the sedimentation speed under gravity [23] or (4) calculating the streaming potential of an electrolyte solution in a capillary [24]. All these techniques do not recover the slip boundary condition (equation 1) directly, but observe the effect on other macroscopic parameters when slip is assumed to be present. Local measurement techniques, which can directly estimate slip, are: (1) (micro-)particle image velocimetry, correlating positions of small particles moving with the flow [4,6,7], (2) near-field laser velocimetry using fluorescence recovery of small particles near a surface [25] and (3) fluorescence cross-correlation, where the fluorescence intensity fluctuations in two volumes separated by a short distance is correlated [26].

Many of these papers investigate slip conditions in microfluidic systems as large surface to volume ratios make boundary conditions especially important. To increase slip, smooth surfaces (e.g. silicon or PDMS) are often made rough by micro-patterning or by depositing carbon nanotube or black silicon forests. To our knowledge, little research has been performed on roughness by porosity. It has been claimed that slip decreases the concentration boundary layer thickness at a porous membrane surface, possibly leading to an increase in overall mass transfer [27-29]. However, the slip at standard porous membrane surfaces is often not large enough to influence the concentration polarization layer [28]. In

this chapter the influence of air-filled porosity and patterning on boundary flow conditions are studied experimentally.

6.2 Experimental

6.2.1 Mold preparation

The surfaces used in the slip experiments described in this chapter are either flat walled micro-channels or micro-channels with a patterned bottom surface (micro-grooves). Molds were prepared in the cleanroom by standard photolithography and deep reactive ion etching on silicon wafers. Each mold contains three fields with each a 50 µm high and 320 µm wide ridge with 20 µm deep grooves on the top. The width of each groove and corresponding line between the grooves is 8, 16 or 32 µm. At either side of the ridge a pool is made to connect the final channel with the tubing. For comparison, a mold with a flat 50 µm high ridge is also designed. Figure 2 gives top and cross-sectional illustrations of a micro-patterned mold with its dimensions.

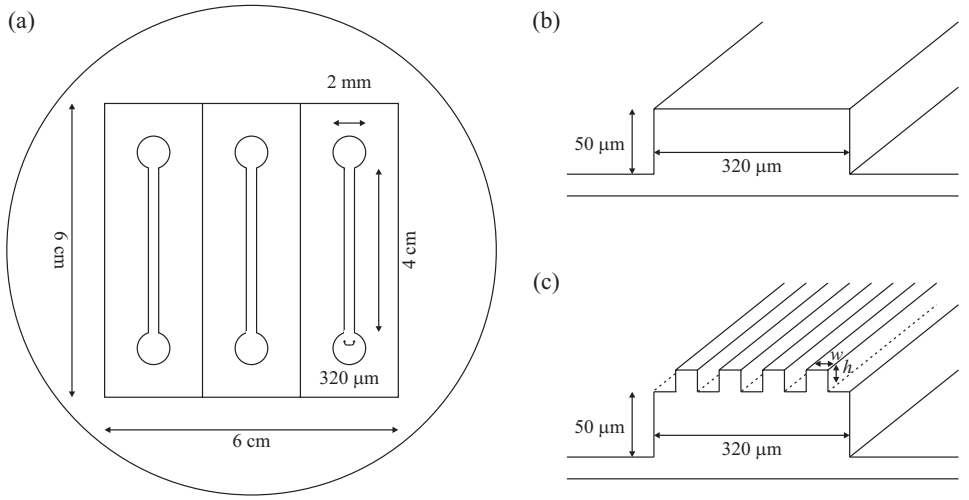

Figure 2. (a) Top view of a mold with three fields with each either a flat or a micro-patterned ridge and entrance / exit areas. (b) Cross-sectional view of a flat ridge with a height of 50 µm and a width of 320 µm. (c) Cross-sectional view of a micro-patterned ridge with micro-pattern dimensions h = 20 µm and w = 8, 16 or 32 µm.

6.2.2 Polymer film and stack preparation

All materials were used as received. Two types of polymer were used: PDMS (polydimethylsiloxane, RTV 615 rubber component A and curing agent B, GE Bayer Silicones) and PVDF (polyvinylidene fluoride, Hylar 460, Ausimont).

To obtain dense PDMS films, the rubber component A was mixed with the curing agent B (10:1 w/w) and degassed before use. The mixture was poured onto the mold (~ 1 mm) and cured in an oven for 3 hours at 80 °C.

Porous PVDF films were prepared via the phase inversion technique [30,31] to create microporosity at the surface. The recipe for microporous PVDF membranes was taken from literature [32]. A solution of 20 wt% PVDF in NMP (1-methyl-2-pyrrolidinone, 99% extra pure, Acros) was prepared by mixing with a mechanical stirrer for 12 hours at 70 °C. The viscous solution was cast on a mold with a thickness of 250 µm and immediately submerged in a 50:50 wt% water / NMP bath for 30 – 60 minutes. If the coagulation bath is lightly agitated the membrane releases itself from the mold after a few minutes. To remove most of the NMP from the membrane, it was submerged in water and ethanol (proanalysis grade, Merck) subsequently for 30 – 60 minutes each. The film was then taped to a piece of paper to prevent from curling-up and left to dry in the fume hood (1 hour) before placing it in a 30 °C vacuum oven overnight.

After film preparation each field was cut and holes were made for liquid entrance / exit. The channel was then sealed with a 170 µm thick glass microscope slide with a refractive index n_g = 1.5255 (D263 borosilicate, Louwers). To seal the PDMS film onto the glass, only the microscope slide was treated with oxygen plasma (Plasmafab 508, Electrotech). Treatment time was 30 seconds at 100 W. The PDMS itself was not treated as this makes the material, including the channel walls, more hydrophilic. Illustrations of the PDMS stacks are given in figure 3a and b.

As PVDF does not have any sticking capabilities of its own. A layer of double sided tape (~ 100 µm thick) was used to bond the PVDF to the glass (figure 3c). As thin porous films are often wavy, the tape also helps to flatten the PVDF film. A cut-out in the tape was made to keep the micro-channel accessible. It was then placed over the PVDF film on the channel side before sticking it onto the glass microscope slide. Two major drawbacks of this preparation method are (1) the PVDF film is never completely flat and (2) the channel height is increased by the thickness of the tape. Direct sealing with glue does not work as the glue is sucked into the pores and channel.

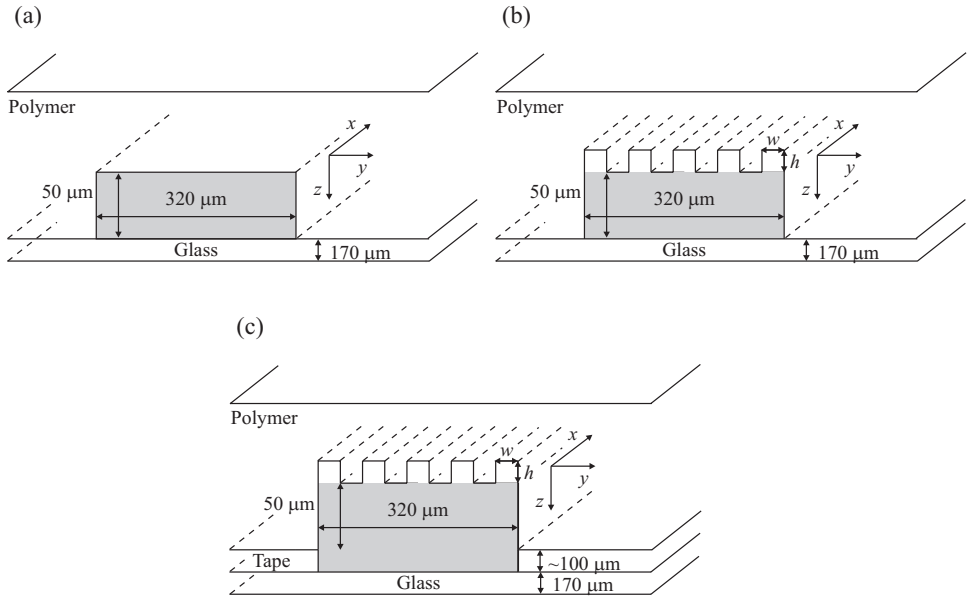

Figure 3. Illustration of different stacks containing a polymer micro-fluidic channel. (a) Example of a channel in PDMS with flat polymer surface and its main dimensions. (b) PDMS stack with a micro-patterned channel (grooves and lines with height h = 20 µm and width w = 8, 16 or 32 µm). (c) PVDF stack with a micro-patterned channel (same mold dimensions) including a layer of sticky tape.

The last preparation step is connecting the tubing to the micro-channel. In the case of PDMS films the tubing was simply inserted in the holes and sealed off by the polymer itself, but the PVDF films were too thin to hold the tubing themselves. The tubing was therefore glued into a small block of PMMA and after drying glued into place at the entrance hole in the film. Both methods supplied a leak-free connection between the tubing and the micro-channel.

6.2.3 Experimental set-up

The polymer film/glass stack was clamped in a homemade holder, connected to the tubing (inner / outer diameter ≈ 0.5 / 1.6 mm) and positioned above the oil immersion Plan-Apochromat 100x objective (numerical aperture NA = 1.4, 1 µm thick image plane) of an inverted optical microscope (Axiovert 40 CFL, Carl Zeiss BV). The oil is halogen-free and low in fluorescence (Immersol^{TM} 518F, Zeiss). The piezoelectric objective-lens positioning system (MIPOS 500, Piezosystem Jena GmbH) allows for reproducibility below 100 nm. Due to the different refractive indexes in the stack, the distance traveled by the piezoelec-

tric system is not the distance traveled by the focal plane (equation 3). The working distance w_d for the oil immersion objective is defined as the sum of the distances traveled through the stack (l_o, l_g = 170 µm and l_w for oil, glass and water, respectively), corrected for the difference in refractive indices (n_o = 1.518 and n_w = 1.333, for oil and water at 20 °C, respectively) [33]. As the working distance is constant (w_d = 170 µm), a 1 µm change in piezo distance z_p leads to a 0.87 µm change in image distance z_i.

$$w_d = \frac{n_o}{n_w} l_w + l_g + l_o = \frac{n_o}{n_w}\left(l_w + z_i\right) + l_g + \left(l_o - z_p\right) \tag{3}$$

MilliQ water containing fluorescent polystyrene particles with a diameter of 0.3 µm (R300 red fluorescing microspheres, Duke Scientific Corporation) was pumped into the microchannel by a syringe pump (PHD 2000, Harvard Apparatus GmbH) and tubing. Typical flow rates are 0.3 – 1 µl/min. A low flow rate is necessary to maintain stable air pockets in the grooves. A dual-head Nd:YLF laser (Pegasus-PIV, New Wave Research) producing two green laser spots with wavelength 527 nm was used to illuminate the particles. The spot was diffused by a holographic 20° light shaping diffuser (Physical Optics Corporation). An external pulse delay generator (Model 565, Berkeley Nucleonics Corporation) was used to trigger the laser. The time between two pulses is determined by the flow rate, but is typically 6 – 15 ms. A high-speed charged coupled device camera (Sensicam, PCO), fit with a ½x or 1x lens adapter, was used for imaging. The measurement principle including a sketch of the set-up was described previously [34].

6.2.4 Recording and post-processing

Per measurement 200 image pairs were processed with DaVis imaging software (version 7.2.2.152, LaVision). These two frames contain the particles at the time of the two pulses. To obtain time-average velocity profiles, a homemade micro-PIV post-processing sequence was run in Matlab R2007b [34]. A steady flow is assumed and interrogation windows of 64 x 16 pixels (~ 8 x 2 µm) were chosen to achieve more spatial resolution in the direction of the flow. Consequently, approximately 10 – 20 particles were counted in each window. The windows were overlapped by 50%. To reduce errors from Brownian motion and to achieve a higher signal-to noise ratio the average correlation method [35] was used to obtain velocity profiles. To minimize the contribution of out-of-focus particle clusters, which contribute to the final result, the space-averaged intensity of each interrogation window was calculated and compared to the corresponding space-time averaged one. Interro-

gation windows with intensity values larger than 102% of the reference were removed (on average 20% of the windows).

Many researchers, e.g. [3], calculate slip from the pressure drop over the channel. In this case it was not feasible to measure the pressure drop due to experimental limitations. A combination of very low flow rates and partly water-filled grooves made it impossible to measure the pressure accurately.

6.2.5 Morphology and interfacial properties

The morphology and dimensions of the polymer films were determined from scanning electron microscope pictures (SEM, JSM 5600LV, JEOL). The films were broken in liquid nitrogen and sputtered with a 30 nm gold layer (SCD 040, Balzers Union). Pictures were taken at 5kV.

Contact angles of the flat films are measured with an optical contact angle measuring instrument (OCA 20, Dataphysics) by suspending a 6 µl water drop on the surface with a speed of 2 µl/s. After deposition, the drop is allowed to stabilize for 10 seconds prior to measuring.

6.3 Results and discussion

6.3.1 SEM: dimensions and porosity

SEM pictures of various channels in PDMS and PVDF provide insight in the dimensions of the channel and grooves and also its porosity and roughness. Figure 4 shows six pictures: flat channels (a: dense PDMS and d: porous PVDF), channels with a grooved surface (b and c: PDMS and f: PVDF) and a higher magnification of the surface porosity of PVDF (e). The dimensions of the mold are nicely replicated by the PDMS. The final dimensions of the PVDF channels and the grooves are smaller than the dimensions on the mold due to shrinkage in the phase separation and drying processes. The average values are given in table 1. Most polymer shrinkage (25 – 32 %) occurs in the lines (all directions) and in the height and length of the large channel. The widths of the channel and the grooves shrink less, which is typical for this type of pattern. The shrinkage of the grooves is physically bound by the lines on the wafer. The groove to line ratio is 1.3 : 1 for PVDF instead of the designed 1 : 1 (mold and PDMS).

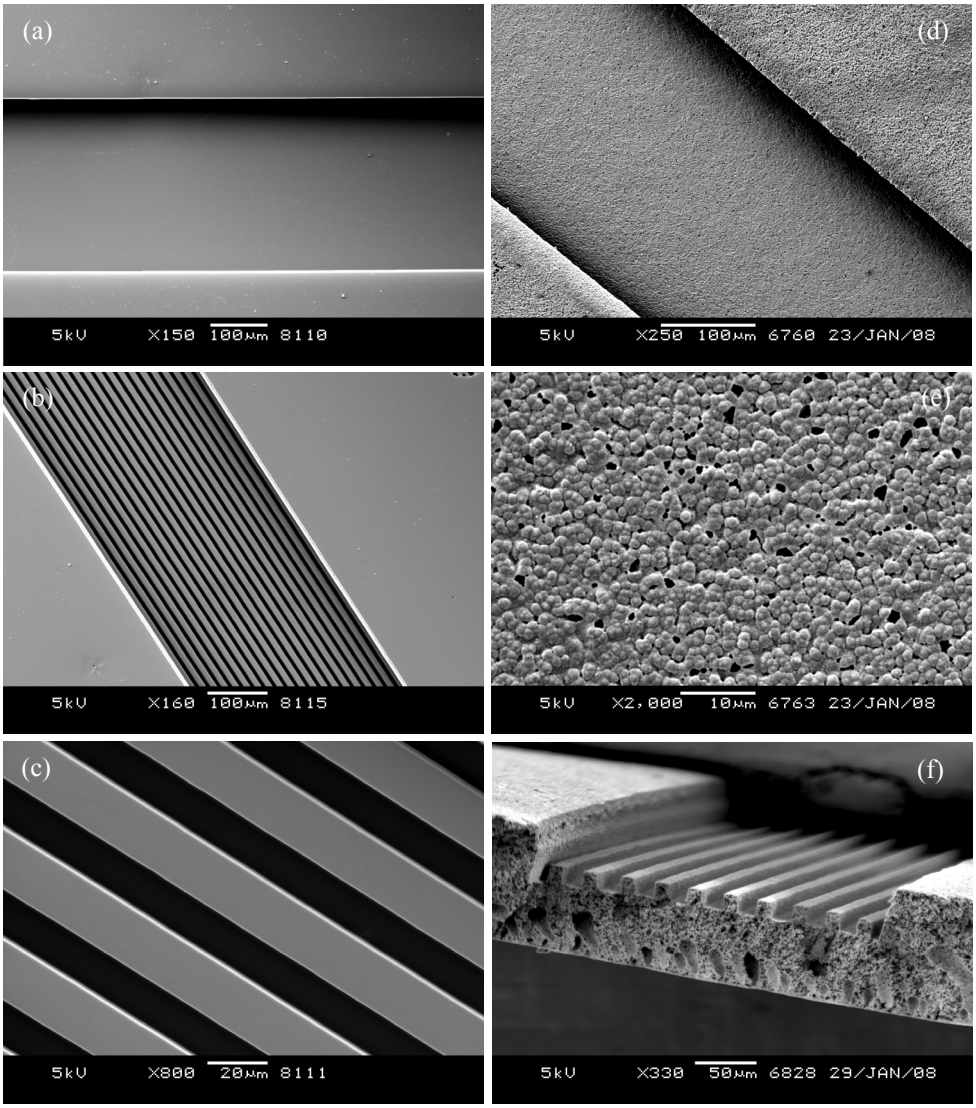

Figure 4. Six SEM images of the channels in PDMS (a-c) and PVDF (d-f). (a) Channel in PDMS with flat surface. (b) Micro-patterned channel with 8 µm wide grooves and lines in PDMS. (c) Micro-pattern with 16 µm wide grooves and lines. (d) Flat channel in microporous PVDF. (e) Zoom of the rough microporous PVDF surface. (f) Cross-section of a micro-patterned PVDF channel prepared on a mold with 16 µm grooves and lines.

Table 1. Average values of different features in the PVDF film compared to the dimensions of the mold.

Feature	Dimension of mold [µm]	Average dimension of PVDF [µm]	Shrinkage [%]
Width channel	320	270	16
Height channel	50	37	26
Length channel	40,000	30,000	25
Width groove	8 / 16 / 32	7 / 15 / 29	6 – 12
Width line	8 / 16 / 32	5.5 / 12 / 21.5	25 – 32
Height line	20	14	30

The PVDF is highly porous and inter-connected throughout the cross-section, but less on the surface. Its surface is also much rougher than the dense PDMS surface as a result of the phase separation process. Its surface pore size distribution is quite narrow with an average pore size of 1.8 µm ± 0.4 µm (determined from SEM pictures). The corners of the grooves contain a few more pores than in the center, but their shapes are not much different.

6.3.2 Contact angles

The static contact angle θ for water measured on a flat PDMS film is 120°. The average static contact angle measured on a flat, but porous PVDF surface is 127.4° ± 2.6°. The contact angle on the micro-pattern was not measured, as the width of the channel is too small.

To determine what the most stable superhydrophobic state is for the micro-patterned surface, their critical contact angles θ_c are calculated with equation 4 (for explanation see chapter 5). The fraction of liquid in contact with the solid φ_s and the roughness factor r have been written out in geometrical terms of the line pattern, with w_{line} and w_{groove} the actual line and groove widths of the micro-patterned film. Table 2 shows that θ_c is always larger than θ, which makes the Cassie-Baxter state the most stable state.

$$\cos\theta_c = \frac{\varphi_s - 1}{r - \varphi_s} = \frac{\left(\frac{w_{line}}{w_{groove} + w_{line}}\right) - 1}{\left(1 + \frac{2h}{w_{groove} + w_{line}}\right) - \left(\frac{w_{line}}{w_{groove} + w_{line}}\right)} \tag{4}$$

Table 2. Critical contact angles for the various micro-patterned surfaces calculated with equation 4.

Polymer	w_{groove} [µm]	w_{line} [µm]	h [µm]	θ_c [°]
PDMS	8	8	20	100
PDMS	16	16	20	107
PDMS	32	32	20	116
PVDF	7	5.5	14	102
PVDF	15	12	14	110
PVDF	29	21.5	14	121

6.3.3 Slip measurements

To determine the slip length of a micro-patterned surface, multiple data sets per experiment were recorded. Each data set contains information about the flow patterns at a certain z-plane (height) above the micro-pattern. The flow of the liquid was visualized with tracer particles and analyzed with micro-PIV techniques. After post-processing, two figures for each set were plotted by the Matlab program. The raw data (figure 5a) was converted into a time-averaged vector plot (figure 5b) and a graph of the time- and space-averaged velocity versus position (figure 5c). The vector plot already contains a lot of qualitative information about flow velocities (the longer and more red the vector, the faster the flow) and direction (pointing into the main flow direction). To quantify this information, the graph displays the averaged velocities in x-direction v_x for each position along the y-axis for a given height z. Flow above the grooves is faster than flow above the lines. For most measurements the v_y, the particle velocity transverse to the flow direction, is smaller than 1 µm/s, which can be regarded as negligible.

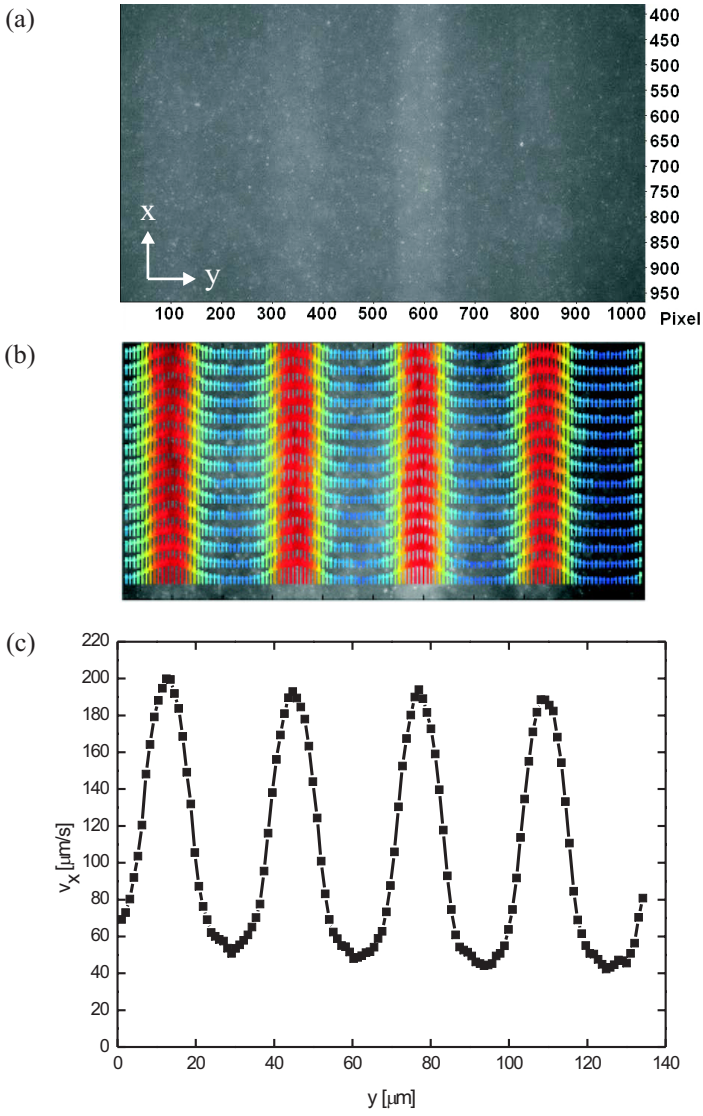

Figure 5. (a) Selected area of one frame (raw data) illustrating the particle flow over a micro-patterned PDMS surface (w = 16 µm) in a focal plane at height z = 0.88 µm above the pattern. (b) The vector plot after post-processing of the frame describes the time-averaged velocity and direction of the flow. (c) The time- and space-averaged velocities in x-direction extracted for this focal plane. Note: the grooves in this example are filled with water.

Micro-patterns with grooves and lines of several sizes were used. The line and groove widths on the mold, *w*, are 8, 16 and 32 µm (paragraph 6.2.1). These are also the dimensions on the PDMS films. In the case of PVDF the final dimensions change somewhat by the phase separation process (see table 1). Figure 6 shows the velocity profiles for a flat PDMS film (a) and two micro-patterns (b and c). The focal planes are not at the same height (z-position). The profiles are a good illustration of the change in velocity at the interface of a liquid-air and a liquid-solid contact area. There is no sharp transition, but a gradual cross-over from a high velocity to a low velocity and vice versa. This shows the influence of the no-slip boundary of the solid.

For an ideal case, in which all grooves are filled with air (complete Cassie-Baxter state), the velocity can be averaged over the whole micro-channel. This averaged value is then determined for each z-position and plotted, with the liquid-air interface taken as the reference-point (z = 0 µm). A velocity profile is obtained and the average slip length b can be determined. During the measurements performed in this research, some grooves are filled with water, while others maintain a stable liquid-air interface. If some of the grooves are filled with water, the average slip length b is no longer a representative value for Cassie-Baxter state slip. The velocity above a water-filled groove is lower than above an air-filled groove and could influence the velocity above the liquid-solid interface as well. To obtain a representative slip length in this situation, the analysis is performed locally above the center of an air-filled groove or a solid line. Separate flow velocities are determined. They are average values of the velocities at the center ± 25% of the width of the groove / line. When these velocities are plotted against their heights, flow profiles appear and the 'local' slip lengths b_{groove} and b_{line} can be determined by extrapolating the data points within 10 µm from the patterned wall with a linear fit. The velocity profiles of a micro-patterned PVDF channel with w = 16 µm are presented in figure 7. The results show that the velocity just above an air-filled groove is higher than above a line (respectively, 26 µm/s and 2 µm/s), but also quickly merge to the same profile.

Figure 6b and c show that for these PDMS films there is a decrease in maximum velocity from left to right. This is caused by a slight tilt (µm-size) of the stack. For PVDF films local height differences can also occur due to the preparation procedure of the polymer film. The shrinkage during phase separation causes waviness in the film. On a local scale, the height can be corrected by subtracting a baseline.

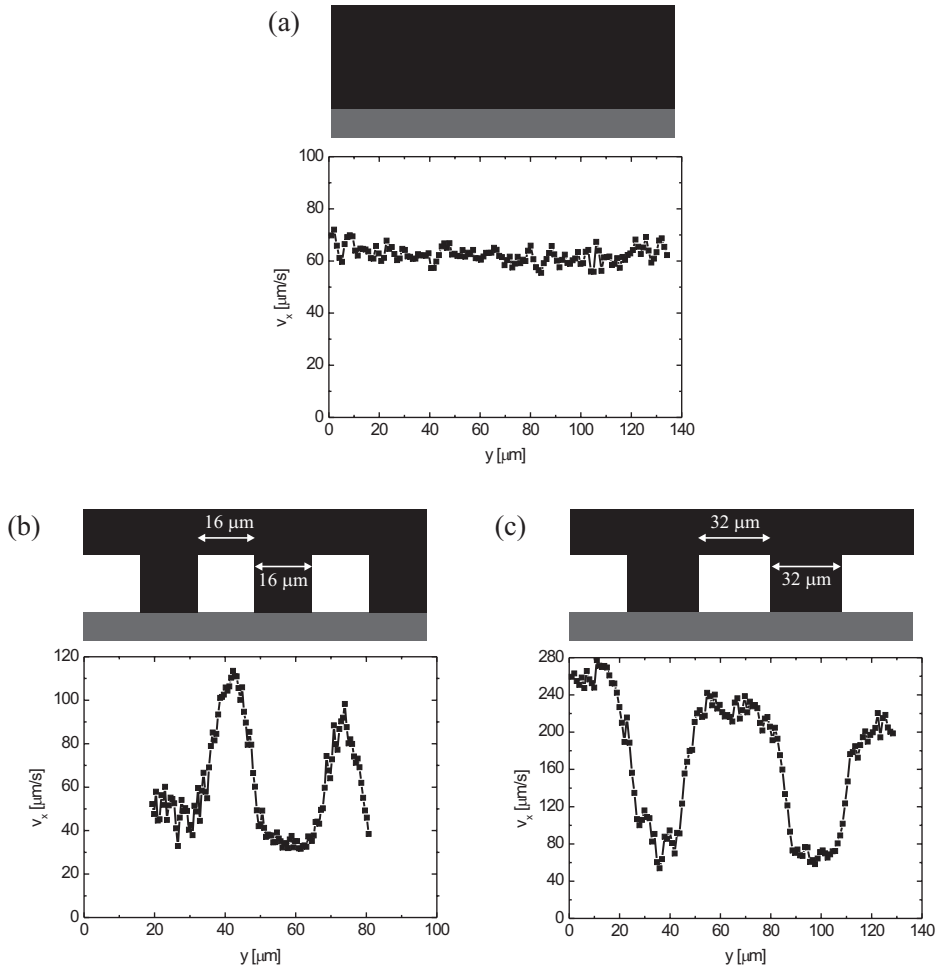

Figure 6. Velocity profiles for flow 1.3 μm above a flat PDMS surface (a) and two micro-patterned PDMS surfaces with w = 16 μm at z = 1.8 μm (b) and w = 32 μm at z = 1.8 μm (c).

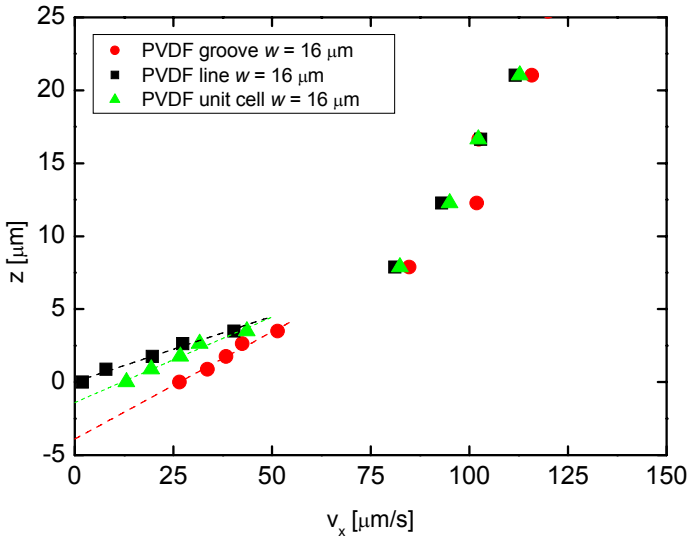

Figure 7. Zoom of the velocity profiles above an air-filled groove, a line and a unit cell of a patterned PVDF surface with w = 16 µm. The top of the micro-pattern is taken as z = 0 µm. Trendlines are included to determine the slip lengths from the cut-off points with y-axis.

To visualize the relationship between slip length and micro-pattern, the local velocity profiles above air-filled PDMS grooves of four different widths are given in figure 8a. Although the initial flow rate is constant, the flow rate in the micro-channel may differ due to slight variations in pressure drop, channel geometry and curvature of the meniscus. This does not affect the comparison of the slip lengths as Ou et al. have shown that the slip length is constant for different flow rates [3]. A zoom near the patterned surface (figure 8b) shows different slopes and an increasing slip length b_{groove} with increasing groove width w (constant groove width to line width ratio). The average results over multiple measurements are given in table 3. The increase in slip is expected as the effect of the no-slip condition at the neighboring line becomes less with wider grooves. A higher slip at the PVDF surface with w = 16 µm compared to the same PDMS surface is expected as the PVDF is more porous and rough, but also because it has a higher groove width to line width ratio (1.3 : 1). As mentioned before, these are effects created by the liquid induced phase separation process.

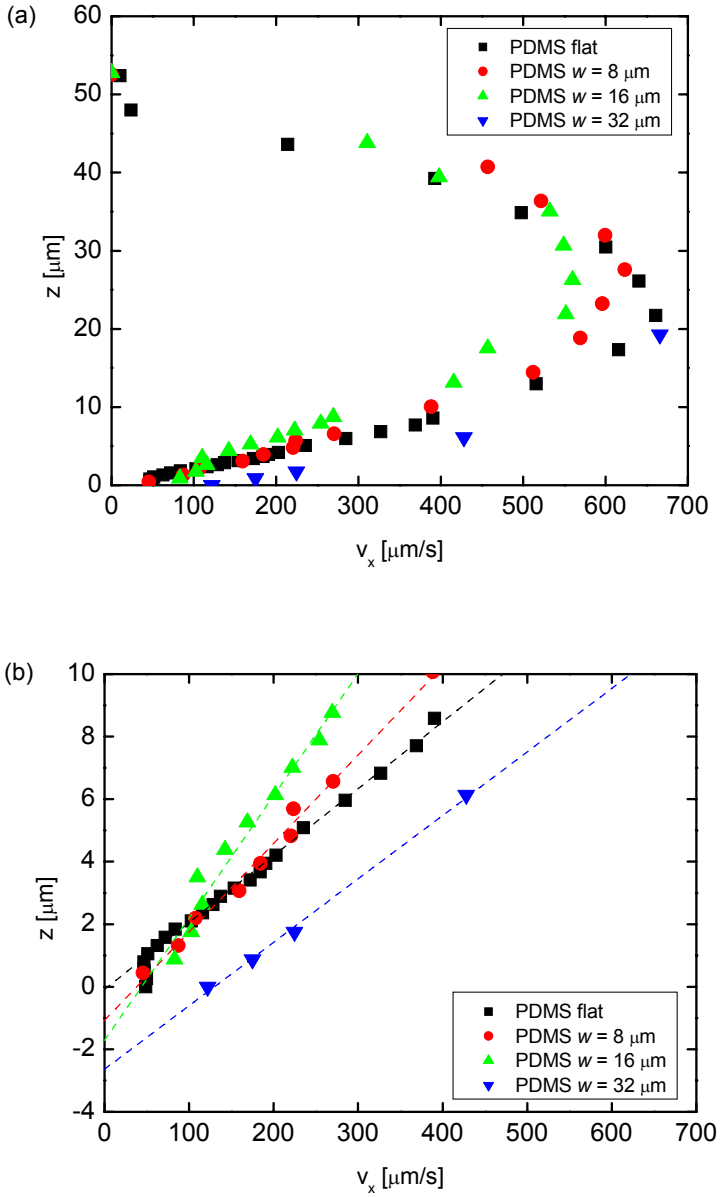

Figure 8. (a) Velocity profiles above air-filled grooves in several channels: w = 0, 8, 16 and 32 μm in PDMS. (b) Zoom of the area near the micro-patterned surface including trendlines and cut-off point with y-axis to determine the slip length b_{groove}.

At a solid surface, the flow should experience no-slip behavior, which means $v_{x,0}$ = 0 µm/s. In practice, often a significant particle velocity is determined in the first micrometer above the surface as can seen in the black data points for flat PDMS in figure 8b. Several reasons can be given for this observation. (1) Out of focus particles in other focal planes influence the intensity of the picture. This is minimized by averaging as described in paragraph 6.2.4. (2) High shear at the surface could lead to a higher acceleration of the particles and thus a higher particle velocity than the actual flow velocity [36]. (3) Smaller particles are affected by the presence of an electric double layer at the surface [6,26]. The exact reason for the change in slope is still unclear. Literature has many conflicting contributions about the interaction between water and a hydrophobic surface [37,38]. Determination of the slip length is not influenced, as the linear part of the velocity profile (up to 10 µm) is extrapolated to v_x = 0 µm/s.

Table 3. Slip lengths in PDMS and PVDF micro-channels with flat or micro-patterned surfaces. b_{groove} Is the value for the local slip length at an air-filled groove and $b_{unit\ cell}$ the average slip length of a representative unit cell (groove + line).

Polymer	*w* on mold [µm]	b_{groove} [µm]	$b_{unit\ cell}$ [µm]
PDMS	0 (flat)	0.19 ± 0.18	0.18 ± 0.15
PDMS	8	0.73 ± 0.39	0.56 ± 0.28
PDMS	16	1.40 ± 0.31	0.48 ± 0.10
PDMS	32	2.59 ± 0.05	2.71 ± 0.82
PVDF	0 (flat)	-0.04 ± 0.19	-0.03 ± 0.17
PVDF	16	2.98 ± 0.40	1.39 ± 0.48

The local slip length b_{groove} cannot directly be compared to the average slip length *b* in literature as stated above. The local slip length b_{groove} describes the maximum value that can be achieved with the micro-pattern under investigation. Most slip values in literature are determined from the average velocities above a unit cell (groove + line). If this unit cell analysis method is applied to the results, the slip lengths become smaller than b_{groove} as velocity profile will lie between the individual groove and line profiles (figure 7). The average slip lengths for these unit cells $b_{unit\ cell}$ are also given in table 3. The results of both calculation methods for the slip length above an air-filled groove are plotted in figure 9 as a summary.

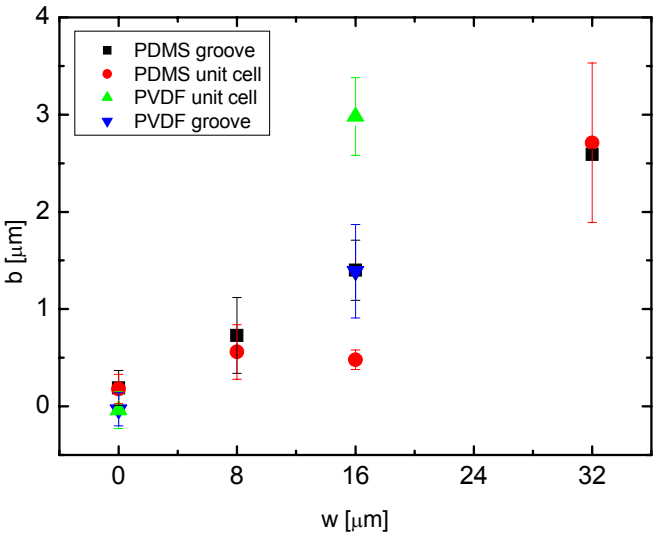

Figure 9. Slip lengths calculated via the groove and unit cell method for all (micro-patterned) PDMS and PVDF surfaces against the groove width on the mold *w*.

A small concern for comparison with literature values should be pointed out. The slip length of the air-filled groove under investigation could be influenced by neighboring water-filled grooves. The extent of the influence is difficult to quantify, but is expected to be low. Although a one-to-one comparison is perhaps not possible, a small overview of literature values for (micro-patterned) hydrophobic surfaces is given to indicate the order of magnitude and trend with varying periodicity. In 2004, Stone et al. concluded that "except for special circumstances requiring care and clever design, the no-slip boundary conditions remains an excellent approximation for flows at scales above tens of nanometers" [18]. In one of those early publications with a 'clever design' [9], flow over a smooth surface was simulated and compared to flow over a nano-pattern for both the Wenzel state and the Cassie-Baxter state. The slip length for the simulations with a smooth surface is 10 – 25 nm. For flow in the Wenzel state the slip is 10 times smaller and in the Cassie-Baxter state 2.5 times larger.

Since then many more publications have appeared for slip investigations both on the nano- and micro-scale [39]. Slip along carbon nanotube forests has been reported. For flow in the Cassie-Baxter state slip lengths up to 1.5 μm, increasing with roughness, were found [7]. For a carbon nanotube forest coated with a Teflon® layer a slip length of 20 μm was found [11]. Again it was reported the slip length vanishes when the liquid is in the Wenzel state

[7]. Experimental studies with micro-patterned surface report an apparent slip length of 5 – 7.5 μm for grooves with w = 30 μm [4] and slip lengths exceeding 20 μm for 80 μm wide grooves next to 20 μm wide ridges [3]. Scaling laws predict that the slip length for an optimized pattern can reach 100 μm [14]. This is of course only possible if the groove width is not so large that the flow enters the Wenzel state.

The research described in this chapter can best be compared to the studies of Ou et al. [4]. The slip lengths for air-filled PDMS grooves with similar dimensions show the same trends, but do not exceed 3 μm for w = 32 μm. A porous PVDF film could create more slip. As mentioned before, the combination of the Cassie-Baxter state and the Wenzel state flow in one experiment perhaps decreases the slip length compared to complete Cassie-Baxter flow.

6.3.4 Effect of slip on concentration polarization

As stated in the introduction, slip at a membrane surface could theoretically decrease concentration polarization. An analytical solution for a velocity profile including a slip contribution and a suction velocity at the porous wall has been proposed [28]. The publication shows that a small increase of the slip coefficient φ (determined by pore size, permeability and the height of the channel) can lead to a large decrease in concentration polarization near the membrane wall. To determine if the amount of slip observed in the measurements performed with grooved (porous) surfaces is enough to affect concentration polarization, the velocity profiles of figure 8a were compared with the analytical solution.

The equations for the velocity in the flow direction $u(x, \lambda)$ (equation 5) and the velocity normal to the flow $v(\lambda)$ (equation 6) are:

$$u(x,\lambda) = \left(u_0 - \frac{v_w x}{H}\right)\left(f_0' + Re_w f_1'\right) \tag{5}$$

$$v(\lambda) = v_w\left(f_0 + Re_w f_1\right) \tag{6}$$

with u_0 the inlet velocity, v_w the suction velocity at the porous wall, x the distance along the flow-axis, H the height of the channel, Re_w the Reynolds number at the porous wall and f_0 and f_1 functions depending on the slip coefficient φ and the dimensionless coordinate in the z-direction $\lambda = z / H$.

The analytical solution is fit to the experimental velocity profiles in figure 8a to obtain values for the slip coefficient φ. The suction velocity v_w is set at 0 as no mass was transported

through the membrane experimentally. This simplifies equation 5 to equation 7 and the normal velocity to $v(\lambda) = 0$. The φ values obtained from the fits are given in table 5.

$$u(x,\lambda) = u_0 f_0' = u_0\left(-3\frac{2(1+\varphi)}{(1+4\varphi)}\lambda^2 + 2\frac{3(1+2\varphi)}{(1+4\varphi)}\lambda\right) \quad (7)$$

Table 5. Calculated slip coefficients φ from fits of the analytical solution (equation 7) to the velocity profiles in figure 8a.

Polymer	*w* on mold [µm]	φ [-]
PDMS	0 (flat)	-0.0006
PDMS	8	0.008
PDMS	16	0.014
PDMS	32	0.058
PVDF	0 (flat)	-0.006
PVDF	16	0.043

These examples show that a micro-pattern and porosity can increase the slip coefficient significantly. The result is a decrease of the concentration polarization layer thickness. According to this theory [28], a slip coefficient $\varphi = 0.05$ reduces the boundary layer thickness by a factor 2.

6.4 Conclusions

The slip lengths of flow along dense and porous polymeric surfaces (PDMS and PVDF, respectively) were measured with the micro-PIV technique. Flat films were compared with micro-patterned films with different line-patterns. Slip along the micro-grooves increases with larger groove widths *w*, even with a constant ratio of groove width versus line width. The increase in slip is expected as the effect of the no-slip condition at the neighboring line becomes less with wider grooves. The largest slip length observed above the liquid-air interface was ~ 3 µm for a porous PVDF film with $w = 16$ µm. Porous micro-patterned PVDF surfaces show higher slip lengths than dense PDMS surfaces due to the roughness and higher groove width to line width ratio caused by shrinkage from the phase separation process.

Literature publications claim that slip can improve membrane transport by minimizing concentration polarization at the surface. To verify this, a couple of experimental velocity profiles were compared to the analytical derivation for the velocity profile along a permeable surface. The amount of slip obtained experimentally in this chapter (without permeation) was found to be sufficient to decrease the concentration polarization layer thickness in membrane processes significantly. Future work has to determine if a similar slip length can be obtained when mass transport through the membrane is present.

6.5 References

1. Navier, C. L. M. H. In *Memoires de l'Academie des Sciences de l'Institut de France*, 1827; Vol. 6.
2. Poiseuille, J. L. M. *Comptes rendus de l'Académie des sciences* **1841**, *12*, 112-115.
3. Ou, J.; Perot, B.; Rothstein, J. P. *Physics of Fluids* **2004**, *16*, 4635-4643.
4. Ou, J.; Rothstein, J. P. *Physics of Fluids* **2005**, *17*.
5. Eijkel, J. *Lab on a Chip* **2007**, *7*, 299-301.
6. Joseph, P.; Tabeling, P. *Physical Review E* **2005**, *71*.
7. Joseph, P.; Cottin-Bizonne, C.; Benoit, J. M.; Ybert, C.; Journet, C.; Tabeling, P.; Bocquet, L. *Physical Review Letters* **2006**, *97*.
8. Roach, P.; McHale, G.; Evans, C. R.; Shirtcliffe, N. J.; Newton, M. I. *Langmuir* **2007**, *23*, 9823-9830.
9. Cottin-Bizonne, C.; Barrat, J. L.; Bocquet, L.; Charlaix, E. *Nature Materials* **2003**, *2*, 237-240.
10. Choi, C. H.; Westin, K. J. A.; Breuer, K. S. *Physics of Fluids* **2003**, *15*, 2897-2902.
11. Choi, C. H.; Kim, C. J. *Physical Review Letters* **2006**, *96*.
12. Lauga, E.; Brenner, M. P.; Stone, H. A. In *Handbook of Experimental Fluid Dynamics*; Foss, J., Tropea, C., Yarin, A., Eds.; Springer: New-York, 2007.
13. Lauga, E.; Stone, H. A. *Journal of Fluid Mechanics* **2003**, *489*, 55-77.
14. Ybert, C.; Barentin, C.; Cottin-Bizonne, C.; Joseph, P.; Bocquet, L. *Physics of Fluids* **2007**, *19*.
15. Truesdell, R.; Mammoli, A.; Vorobieff, P.; van Swol, F.; Brinker, C. J. *Physical Review Letters* **2006**, *97*.
16. Tretheway, D. C.; Meinhart, C. D. *Physics of Fluids* **2004**, *16*, 1509-1515.
17. Joly, L.; Ybert, C.; Trizac, E.; Bocquet, L. *Journal of Chemical Physics* **2006**, *125*.

18. Stone, H. A.; Stroock, A. D.; Ajdari, A. *Annual Review of Fluid Mechanics* **2004**, *36*, 381-411.
19. Neto, C.; Evans, D. R.; Bonaccurso, E.; Butt, H. J.; Craig, V. S. J. *Reports on Progress in Physics* **2005**, *68*, 2859-2897.
20. Persson, B. N. J.; Mugele, F. *Journal of Physics-Condensed Matter* **2004**, *16*, R295-R355.
21. Bocquet, L.; Tabeling, P.; Manneville, S. *Physical Review Letters* **2006**, *97*.
22. Choi, C. H.; Kim, C. J. *Physical Review Letters* **2006**, *97*.
23. Boehnke, U. C.; Remmler, T.; Motschmann, H.; Wurlitzer, S.; Hauwede, J.; Fischer, T. M. *Journal of Colloid and Interface Science* **1999**, *211*, 243-251.
24. Churaev, N. V.; Ralston, J.; Sergeeva, I. P.; Sobolev, V. D. *Advances in Colloid and Interface Science* **2002**, *96*, 265-278.
25. Hervet, H.; Leger, L. *Comptes Rendus Physique* **2003**, *4*, 241-249.
26. Lumma, D.; Best, A.; Gansen, A.; Feuillebois, F.; Radler, J. O.; Vinogradova, O. I. *Physical Review E* **2003**, *67*.
27. Beavers, G. S.; Joseph, D. D. *Journal of Fluid Mechanics* **1967**, *30*, 197-207.
28. Chellam, S.; Wiesner, M. R.; Dawson, C. *Journal of Engineering Mathematics* **1992**, *26*, 481-492.
29. Ajdari, A.; Bocquet, L. *Physical Review Letters* **2006**, *96*.
30. Vogelaar, L.; Barsema, J. N.; van Rijn, C. J. M.; Nijdam, W.; Wessling, M. *Advanced Materials* **2003**, *15*, 1385-+.
31. Vogelaar, L.; Lammertink, R. G. H.; Barsema, J. N.; Nijdam, W.; Bolhuis-Versteeg, L. A. M.; van Rijn, C. J. M.; Wessling, M. *Small* **2005**, *1*, 645-655.
32. Peng, M.; Li, H. B.; Wu, L. J.; Zheng, Q.; Chen, Y.; Gu, W. F. *Journal of Applied Polymer Science* **2005**, *98*, 1358-1363.
33. Meinhart, C. D.; Wereley, S. T. *Measurement Science & Technology* **2003**, *14*, 1047-1053.
34. Pirat, C.; Naso, A.; van der Wouden, E. J.; Gardeniers, J. G. E.; Lohse, D.; van den Berg, A. *Lab on a Chip* **2008**, *8*, 945-949.
35. Meinhart, C. D.; Wereley, S. T.; Santiago, J. G. *Journal of Fluids Engineering-Transactions of the Asme* **2000**, *122*, 285-289.
36. Westerweel, J. *Experiments in Fluids* **2008**, *44*, 831-842.
37. Poynor, A.; Hong, L.; Robinson, I. K.; Granick, S.; Zhang, Z.; Fenter, P. A. *Physical Review Letters* **2006**, *97*.

38. Ocko, B. M.; Dhinojwala, A.; Daillant, J. *Physical Review Letters* **2008**, *101*, 039601.

39. Voronov, R. S.; Papavassiliou, D. V.; Lee, L. L. *Industrial & Engineering Chemistry Research* **2008**, *47*, 2455-2477.

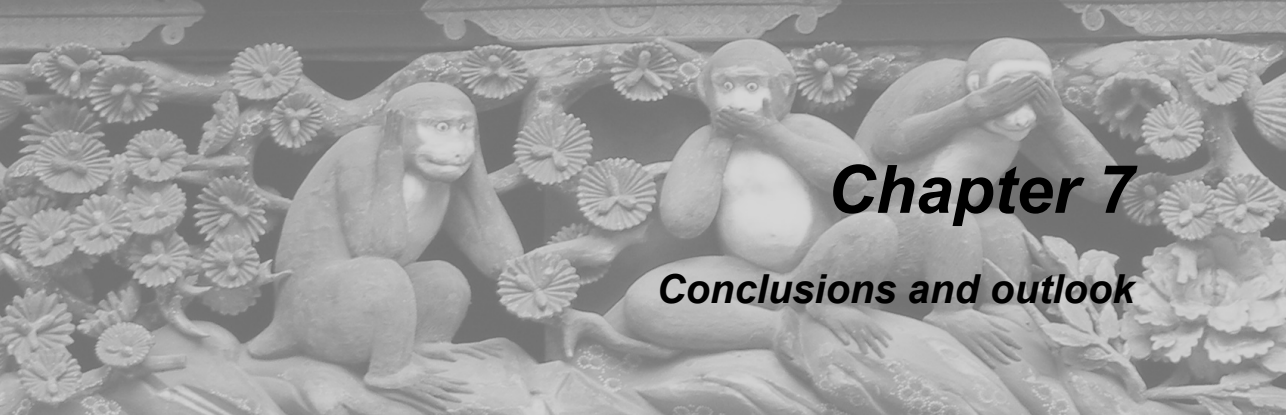

Chapter 7

Conclusions and outlook

To conclude this thesis, the research question, which was posed in the introduction, is answered through combining the most important findings of the previous chapters. The outlook provides examples for future research and ideas for practical applications of micropatterns in membrane technology and other areas.

7.1 Conclusions

The main question posed in the introduction of this thesis is:

How can mass transport through a polymeric membrane benefit from surface micro-patterning?

As described in chapter 2, several publications have addressed this topic. Increasing the surface area with means of a pattern has proven to be an effective measure to increase flux in pervaporation and gas permeation processes. Any additional flux increase is often attributed to the change in local flow patterns at the surface, also called micro-turbulence. This thesis has given another explanation for flux enhancement in diffusion driven processes and has shown that the possibilities are not limited to these examples.

Gas permeation experiments with micro-patterned, dense membranes (chapter 3) lead to the belief that surface area increase is not the only positive result in diffusion controlled transport processes. The shape of the polymeric film also creates additional lateral diffusion through the membrane. Increased transport through same polymer mass is realized by locally decreasing the thickness of the membrane and creating additional surface area, while maintaining the selectivity and mechanical strength of the film. Simple analytical calculation and 2D finite element simulations confirm the increase in flux, although the experimental values do not reach their theoretical maximum. A micro-patterned membrane is somewhat comparable to a composite membrane, with the difference that the 'support layer' is permeable and can contribute to gas permeation as well. Initial simulations show that micro-patterned membranes have a potential advantage over composite membranes because of this additional permeable volume.

Liquid in contact with a micro-patterned surface shows very different wetting behavior than in contact with a flat surface. Hydrophobic materials with a micro-pattern can even repel water so much that the liquid is partly suspended on an air layer (the superhydrophobic Cassie-Baxter state). Most of the times this state is metastable and a transition will take place to the Wenzel state, where the liquid wets the complete micro-patterned surface. The dynamical behavior of this transition has been the main topic of chapters 4 and 5. After initial imbibition between the micro-pillars from the liquid reservoir on top of the pattern, the liquid spreads (fast) in lateral direction. The propagation of the wetting front through a square array of square micro-pillars depends largely on the geometry (pillar height h and gap size between pillars a) and material properties (intrinsic material contact angle θ). The

front velocity v_{front} increases with larger gap sizes, lower pillars and lower intrinsic contact angle. If the polymeric film is patterned with a gap size smaller than its critical gap size a_c, propagation does not occur, i.e. the Cassie-Baxter state is stable. For the square pillars in a square array the critical gap size can be calculated from an energy balance (equation 1).

$$a_c = \frac{2h}{\cos\theta + 1} - 2h \tag{1}$$

Two different velocities were distinguished: one for filling a single row (zipping velocity v_z) and one for the propagation from one row to the next row (main front velocity v_{front}). Slow front propagation occurs for gap sizes close to the critical gap size. During the slow propagation the zipping motion is clearly visible. The liquid first fills up an empty row perpendicular to the main front direction before propagating towards the next row. The zipping velocity can be orders of magnitude faster than the main front velocity resulting in a square wetted area. The main front velocity undergoes dispersion at gap sizes close to the critical point, pointing out that it is sensitive to local wetting properties. These influences are less pronounced at larger gap sizes (i.e. further from the critical point). With these geometries the liquid front wets multiple rows at once (faster main front velocity), leading to a more circular wetted area. All these observations were also seen in the results of lattice Boltzmann simulations. The wetted area changes with geometry and the zipping motion is observed. Additionally, the movement in the third dimension (height) can be visualized. The complex interface curvature indicated by 2D analysis is confirmed by the simulations.

To be able to predict the wetting front velocity for any combination of h, a and θ, a universal scaling argument is derived (chapter 5). The argument that rescales all measurements to a single curve is derived via the two subcell approach including assumptions valid in the zipping regime (equation 2). The two subcells are defined as the volume between two pillar walls and the volume beyond the pillars (A and B in figure 1, respectively), which together form the unit cell of this geometry. The velocity of the main front v_{front} is expressed by the capillary number Ca. In the scaling argument the width of the pillar w (with wavelength $d = a + w$) is also of great importance as the hydrophobic pillar surface resists wetting.

$$Ca_{zipping} = \frac{\eta v_{front}}{\sigma_{lg}} \sim \frac{d}{w}\left(1 + \cos\theta\left(\frac{2h + a}{a}\right)\right) \tag{2}$$

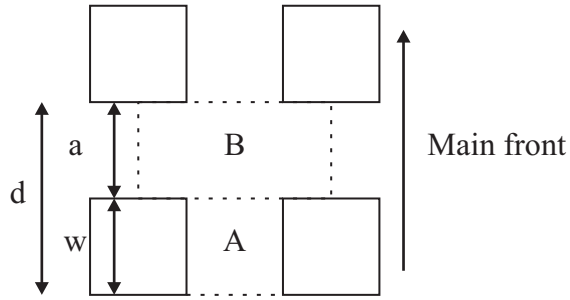

Figure 1. Illustration of the top view of four pillars with wavelength *d* (gap size *a* + pillar width *w*). The dotted lines mark the unit cell with subcells A and B.

Hydrodynamics and membranes always have had a strong connection, but research was mainly performed on a larger scale (bulk flow profiles). The fluid behavior on the micro-scale at a solid surface can influence membrane processes severely. In chapter 6, the flow dynamics along a superhydrophobic surface, causing a composite liquid-air / liquid-solid interface and by that a slip flow, has been connected to transport behavior of pervaporation membranes. Experiments have proven that a slip flow is present along polymeric micro-patterned surfaces, either dense or porous. Further comparison with an analytical solution shows that the amount of slip generated by the micro-pattern is theoretically large enough to significantly decrease the thickness of the concentration polarization layer at the membrane surface. Tuning the flow by surface properties can therefore result in an improvement of transport.
As an overall conclusion the answer to the posed question can be:

A carefully chosen micro-pattern can enhance membrane transport for processes like gas permeation and pervaporation by changing flow dynamics in and along the membrane.

7.2 Outlook

This thesis has shown that micro-patterning is a general principle, which can be of practical use in membrane technology. The results of this research should not be limited to improving industrial applications. Micro-patterns could be implemented in daily life as functional surfaces for packaging, (sports)textiles and medical equipment. Some applications are given in this paragraph along with some proposals to answer the questions that resulted from this research, but were not investigated.

7.2.1 Micro-patterns and diffusion

The results from the gas permeation and pervaporation experiments suggest that several other membrane processes could also benefit from the micro-patterning technique. All diffusion driven processes can use the altered diffusion paths through the membrane caused by a micro-pattern to enhance transport. If a large scale production line for micro-patterns can be developed, a micro-patterned membrane can perhaps even compete with a composite membrane prepared via a two-step production method. Finite element simulations give positive output for this concept, but it has not been verified experimentally.

Micro-patterned polymeric films could be applied in breathable clothing. Important aspects that micro-patterned polymers could provide are fast water vapor transport, super-rejection of water in the liquid form, an enlarged surface area at the air side to remove the vapor and the mechanical strength and flexibility to wear the clothes multiple times. The same arguments are relevant to (semi)permeable food packaging materials.

7.2.2 Micro-patterns and hydrodynamics

The fact that micro-patterns can also change hydrodynamics in adjacent phases opens up another world of possibilities. For membrane applications minimization of concentration polarization is the most interesting. Research in the field of electrodialysis has already proven micro-patterning to be effective and this thesis indicates that also pervaporation can benefit from this technique. However, the pervaporation experiments to directly prove enhanced transport with micro-patterned membranes have not been performed yet. Ultrafiltration experiments with hollow fiber and tubular membranes have proven that slip enhances the permeate flux significantly [1].

Nowadays, the right clothing seems crucially important to obtain record-breaking performances in various sports. Athletes and swimmers wear tight fitting suits with drag reducing areas and carefully chosen fabrics to make them faster. The Speedo swimming suits used in the 2008 Olympic Games in Beijing contain rough patches as found on sharks [2]. Slip conditions at the suit surface have helped swimmers to obtain faster results than ever before. Another way to utilize the slip-condition is to reshape the surface of (food) packaging materials. Initial laboratory tests have proven that yoghurt will slide off a tilted micro-patterned surface faster and with fewer residues compared to a flat surface of the same polymer (polypropylene). Pouring fluids from micro-patterned cartons and cups will result in cleaner spouts and less product retained in the package.

In maritime research, various modifications to boat hulls have resulted in drag reduction by slip generation to save energy. Large air-cavities have been developed to create a layer of

air between the hull and the water [3]. Another invention is a double-walled hull collecting (exhaust) gas, which is released as micro-bubbles through the outer wall to decrease drag [4-6]. A porous micro-patterned boat hull could perhaps increase the air-water interface area even more.

Gas-liquid contactors can benefit from superhydrophobic properties of a micro-patterned surface as well. Liquid in the Cassie-Baxter state will have a huge liquid-gas interface, especially when the material is also porous. A kind of porous polymer forest (similar to the carbon nanotube / black silicon forests) would be most optimal to create strong non-wetting conditions for a large exchange interface and a small liquid-solid contact area for slip generation.

7.2.3 Micro-patterns and stability

As stated in the previous paragraph, stability of the Cassie-Baxter state is a major issue for all superhydrophobic applications. Design parameters for the Cassie-Baxter to Wenzel transition have been investigated extensively, but only a few articles describe the stability of this superhydrophobic state. In certain bioanalytical applications, such as cell sorting and bioassays, long-term stability of the Cassie-Baxter state is very important. The first publication on this topic reported stabilities up to 1 month [7]. This issue is also very important for applications in the textile industry. The durability of superhydrophobic cellulose based materials for clothing was tested by washing the material [8]. The self-cleaning effect was stable up to 20 washes. In this thesis, stability issues have been a problem as well. In some slip measurements, the water could easily transition to the Wenzel state. The effect of this mixed Cassie-Baxter and Wenzel state flow should be investigated further to fully understand the impact on long term application. Future work could also investigate the possibility of a gas pressure on the back side of a micro-patterned surface to maintain a stable Cassie-Baxter flow.

Stability of the Cassie-Baxter state is not always desired, though. Lack of stability has been used as a tool to fundamentally investigate the physics behind the transition to the Wenzel state, but can perhaps also be applied in practice. Control of flow velocity and direction can be achieved with micro-patterned surfaces. A possible application could be liquid transport for medical diagnostics. After applying a drop of blood on a micro-patterned surface, the pattern can guide a small volume of the drop in different directions and with different velocities. By applying arrays of micro-pillars with in- or decreasing gap sizes liquid flows can even be sped up or slowed down, respectively.

7.2.4 Micro-patterns and other liquids

In chapter 2, a remark was made on the terminology in wetting research. It was discussed that the preposition hydro- (water) should be changed into hygro- (liquid) when speaking about the wettability of a surface. Most researchers only report the (super)hydrophobic nature of a solid surface, which tells you about the wetting with water, not about the interaction with other liquids. In future, wettability and slip research should be extrapolated to liquids other than water to generate more practical applications for micro-patterned surfaces. This further research is important as most organic liquids, frequently used in industrial processes, have lower surface tensions than water and therefore will not be repelled as easily. Superoleophobic surfaces are extremely rare, but can be designed by applying a micro-pattern [9]. Cell-culturing researchers are also becoming increasingly interested as a micro-pattern could affect the adherence, growth direction and sorting of cells [7]. These are a few reasons not to "stick" to (pure) water.

To conclude this thesis, one can state that the micro-patterning technique gives us a versatile tool to tune and control the dynamics of gases, liquids and solutes on the micro-scale for various applications.

7.3 References

1. Yeh, H. M.; Cheng, T. W. *Journal of Membrane Science* **1999**, *154*, 41-51.
2. Speedo *GB2411816* **2004**.
3. Matveev, K. *Speed at sea* **2003**, *February*, 13-16.
4. Truong, V.-T. “Drag Reduction Technologies,” DSTO Aeronautical and Maritime Research Laboratory, 2001.
5. Latorre, R.; Miller, A.; Philips, R. *Ocean Engineering* **2003**, *30*, 2297-2309.
6. Philips, R. B. **2005**, *US6932012*.
7. Wang, Y.; Bachman, M.; Sims, C. E.; Li, G. P.; Allbritton, N. L. *Analytical Chemistry* **2007**, *79*, 7104-7109.
8. Li, S. H.; Zhang, S. B.; Wang, X. H. *Langmuir* **2008**, *24*, 5585-5590.
9. Tuteja, A.; Choi, W.; Ma, M. L.; Mabry, J. M.; Mazzella, S. A.; Rutledge, G. C.; McKinley, G. H.; Cohen, R. E. *Science* **2007**, *318*, 1618-1622.

Appendix: nomenclature

Roman symbols

Symbol	Description	Chapter
a	Gap size between pillars [m]	4, 5, 7
a_c	Critical gap size [m]	5, 7
A	Permeability constant [depends on *X*]	2
b	Slip length [m]	6
b_{groove}	Slip length above a groove [m]	6
b_{line}	Slip length above a line [m]	6
$b_{unit\ cell}$	Slip length of a unit cell [m]	6
Bo	Bond number [-]	2
c_f	Solute concentration in feed [mol/m^3]	2
c_m	Solute concentration at the membrane surface [mol/m^3]	2
c_p	Solute concentration in permeate [mol/m^3]	2
c_0	Initial gas concentration [mol/m^3]	3
Δc	Concentration difference over the membrane [kg/m^3]	3
Ca	Capillary number [-]	5
Ca_A	Capillary number subcell A [-]	5
Ca_B	Capillary number subcell B [-]	5
$Ca_{zipping}$	Capillary number in zipping regime [-]	5, 7
$Ca_{non-zipping}$	Capillary number in non-zipping regime [-]	5
d	Drop diameter [m]	2
	Wavelength [m]	4, 5, 7
D	Diffusion coefficient [m^2/s]	3
D_i	Diffusion coefficient of solute *i* [m^2/s]	2

Symbol	Description	Chapter
E	Experimental advantage of a micro-patterned membrane over a flat membrane [%]	3
E_0	Membrane's intrinsic enrichment [-]	2
dE_d	Energy gain of viscous dissipation for small displacement *dx* [Pa m^3 = N m]	5
ΔE_d	Difference in energies of viscous dissipation before and after the transition [Pa m^3 = N m]	5
dE_s	Surface energy gain for small displacement *dx* [Pa m^3 = N m]	5
ΔE_s	Difference in surface energies before and after the transition [Pa m^3 = N m]	5
Fr	Froude number [-]	2
f_0	Zeroth order function [-]	6
f_1	Fraction material 1 [-]	2
	First order function [-]	6
f_2	Fraction material 2 [-]	2
g	Gravity constant [m/s^2]	2
h	Pillar height [m]	3, 5, 7
	Height of ridge / groove on mold [m]	6
H	Micro-channel height [m]	6
J	Flux through a membrane [depends on *X*]	2
J_v	Volume flux through a membrane [m^3/m^2 s]	2
$J_{patterned}^{exp}$	Experimental flux through a micro-patterned membrane [GPU = gas permeation unit, 10^{-6} cm^3(STP) cm^{-2} s^{-1} $cmHg^{-1}$]	3
J_{flat}^{theory}	Theoretical flux through a flat membrane	3

Symbol	Description	Chapter
	[GPU = gas permeation unit, 10^{-6} cm^3(STP) cm^{-2} s^{-1} $cmHg^{-1}$]	
$J_{patterned}^{theory}$	Theoretical flux through a micro-patterned membrane [GPU = gas permeation unit, 10^{-6} cm^3(STP) cm^{-2} s^{-1} $cmHg^{-1}$]	3
l	Characteristic length scale [m]	5
l_{eff}	Effective diffusion length through the selective layer of a composite membrane [m]	3
l_g	Real distance traveled in gas [m]	6
$l_{\max}$	Maximal linear diffusion path length through the selective layer to a pore [m]	3
l_o	Real distance traveled in oil [m]	6
l_w	Real distance traveled in water [m]	6
l_0	Thickness of the selective layer of a composite membrane [m]	3
n	Number of values to average [-]	3
n_o	Refractive index of oil [-]	6
n_g	Refractive index of gas [-]	6
n_w	Refractive index of water [-]	6
Oh	Ohnesorge number [-]	2
$P_{flat,n}^{exp}$	Experimental permeability of the n^{th} flat membrane [Barrer, 10^{-10} cm^3(STP) cm cm^{-2} s^{-1} $cmHg^{-1}$]	3
$P_{patterned}^{exp}$	Experimental permeability of a micro-patterned membrane [Barrer, 10^{-10} cm^3(STP) cm cm^{-2} s^{-1} $cmHg^{-1}$]	3
$\left\langle P_{flat}^{exp} \right\rangle$	Average experimental permeability of all flat membranes [Barrer, 10^{-10} cm^3(STP) cm cm^{-2} s^{-1} $cmHg^{-1}$]	3

Symbol	Description	Chapter
r	Roughness factor [-]	2, 5, 6
	Pore radius of the support layer of a composite membrane [m]	3
R	Membrane retention [-]	2
R_a	Roughness amplitude [m]	2
R_w	Roughness wavelength [m]	2
Re	Reynolds number [-]	2
Re_w	Reynolds number at porous wall [-]	6
t	Time [s]	4
t_0	Time from balance of forces [s]	4
t_1	Time when zipping in 1st row starts (domain 1) [s]	4
t_1'	Time when zipping in 1st row starts (domain 2) [s]	4
t_2	Time when zipping in 1st row ends (domain 1) [s]	4
t_2'	Time when zipping in 2nd row starts (domain 2) [s]	4
t_3	Time when zipping in 2nd row starts (domain 1) [s]	4
t_3'	Time when zipping in 1st row ends (domain 2) [s]	4
t_l	Latency time = time between end 1st row and start 2nd row [s]	4
T	Theoretical advantage of a micro-patterned membrane over a flat membrane [%]	3
u	Fluid velocity [m/s]	6
$u(x,\lambda)$	Velocity in flow direction [m/s]	6
u_x	Fluid velocity in x-direction [m/s]	6
$u_{x,0}$	Slip velocity at the wall [m/s]	6
u_0	Inlet velocity [m/s]	6

Symbol	Description	Chapter
v	Characteristic velocity [m/s]	5
$v(\lambda)$	Velocity normal to flow [m/s]	5
v_A	Velocity between two pillars [m/s]	5
v_B	Zipping velocity [m/s]	5
v_{front}	Front velocity [m/s]	4, 5, 7
$v_{non-zipping}$	Front velocity in non-zipping regime [m/s]	5
v_w	Suction velocity at porous wall [m/s]	6
v_x	Time- and space-averaged velocity in x-direction [m/s]	6
v_z	Zipping velocity [m/s]	4
$v_z^{\max}$	Maximal zipping velocity [m/s]	4
$v_{zipping}$	Front velocity in zipping regime [m/s]	5
v_0	Impact velocity [m/s]	2
dV	Small volume [m^3]	5
w	Pillar width [m]	4, 5, 7
	Width of ridge / groove on mold [m]	6
w_d	Working distance objective [m]	6
w_{groove}	Width of groove on polymer film [m]	6
w_{line}	Width of line on polymer film [m]	6
We	Weber number [-]	2
x	Membrane thickness [m]	2
	Distance front has traveled from initiation point [m]	4
	Distance in x-direction (flow-direction) [m]	6
x_A	Concentration A in feed [mol/m^3]	2
x_B	Concentration B in feed [mol/m^3]	2
dx	Small advancing displacement of liquid front [m]	5

Symbol	Description	Chapter
Δx	Effective membrane thickness [m]	3
X	Stands for concentration, temperature or pressure [mol/m^3, K or Pa]	2
y	Distance in y-direction (perpendicular to flow) [m]	6
y_A	Concentration A in permeate [mol/m^3]	2
y_B	Concentration B in permeate [mol/m^3]	2
z	Height from pillar base [m]	4
	Distance in z-direction (channel height) [m]	6
z_i	Change in image distance [m]	6
z_p	Change in piezo distance [m]	6

Greek symbols

Symbol	Description	Chapter
α	Membrane selectivity [-]	2
$\alpha_{A/B}$	Separation factor of component A [-]	2
β	Proportionality factor [Pa s/m = N s/m^3]	6
γ_{gs}	Gas – solid interfacial tension [Pa m = N/m]	2
γ_{ls}	Liquid – solid interfacial tension [Pa m = N/m]	2
γ_{lg}	Liquid – gas interfacial tension [Pa m = N/m]	2
$\dot{\gamma}$	Characteristic shear rate [1/s^2]	5
δ	Boundary layer thickness [m]	2
	Slip length [m]	6
ε	Porosity of the support layer in a composite membrane [-]	3
	Rate of viscous dissipation per unit volume [Pa/s = N/m^2 s]	5
η	Dynamic viscosity [Pa s = N s/m^2]	4, 5-7

Symbol	Description	Chapter
φ	Slip coefficient [-]	6
φ_s	Fraction of liquid in contact with the solid [-]	2, 5, 6
θ	Static / intrinsic contact angle [°]	2, 4-7
	Angle [°]	3
θ_{adv}	Advancing contact angle [°]	2
θ_c	Critical contact angle [°]	4, 5
θ_{rec}	Receding contact angle [°]	2
θ_1	Contact angle material 1 [°]	2
θ_2	Contact angle material 2 [°]	2
θ^*	Apparent contact angle [°]	2, 5
λ	Dimensionless coordinate in y-direction [-]	6
μ	Dynamic viscosity of liquid [Pa s = kg/m s]	2
ρ	Density of liquid [kg/m^3]	2
σ	Tensile stress = force over the cross-sectional area	3
	[Pa = N/m^2]	
$\sigma(\theta)$	Tensile stress with fibers (ridges) on an angle θ [Pa = N/m^2]	3
σ_{lg}	Surface tension of the liquid-gas interface [Pa m = N/m]	2, 4-7
$\sigma_{parallel}$	Tensile stress parallel to the fibers (ridges) [Pa = N/m^2]	3
$\sigma_{perpendicular}$	Tensile stress perpendicular to the fibers (ridges) [Pa = N/m^2]	3
τ	Time lag [s]	5
τ_1	Propagation time between two pillars [s]	5
τ_2	Time to fill up next row (zipping time) [s]	5
τ_A	Time to fill up volume A [s]	5
τ_B	Time to fill up volume B [s]	5

Dankwoord

Aan het einde gekomen van het 4+ jarig avontuur dat promotie heet, wil ik via deze weg mijn dank uitspreken aan heel veel mensen die het een leuke periode in mijn leven hebben gemaakt. Het onderzoek ging met ups en downs, maar er zijn veel mensen die er met mij in bleven geloven en mij gestimuleerd hebben door te gaan. Daarnaast zijn de eindeloze mogelijkheden in het lab en de sociale omgeving altijd zeer prettig geweest.

Matthias Wessling, mijn promotor. Dank voor de mogelijkheden die je gegenereerd hebt om mijn onderzoek in goede banen te leiden. De flinke ommezwaai van onderwerp na 1,5 jaar is het toonbeeld van jouw rekbaarheid en visie geweest. Ook je aanzet om de samenwerking met andere groepen aan te gaan en er een multidisciplinair project van te maken heb ik zeer gewaardeerd.

Rob Lammertink, mijn dagelijkse begeleider. Je hebt me enorm gesteund met je goede ideeën en persoonlijke motivatie. Altijd stond je deur open voor een goed gesprek. Je snelle en precieze corrigeerwerk, wat zeer heeft bijgedragen aan de leesbaarheid van dit proefschrift, heb ik erg gewaardeerd. Dat je toekomstige micro-onderzoek tot macro-resultaten mag leiden.

My colleagues. It has been great to work in the Membrane Technology Group for the last 5 years. The nice social environment was created by all of you friendly people, joining the Dutch from all over the world. I have felt very at home in this international group. I would like to thank a few group members in particular. Greet Kamminga. Je bent een geweldige vrouw met een onuitputtelijk geduld. Dank voor al die keren dat je klaar stond met je kennis of een helpende hand. John Heeks. Jouw handen kunnen echt alles maken. Geweldig hoe je altijd goedlachs voor iedereen klaar staat. Bedankt voor al je hulp en wijze raad. Herman Teunis. Bedankt voor je reddingsacties bij mijn SEM perikelen. Ineke Pünt en studenten Robin Hink en Wilma de Groot. Jullie drieën hebben me geweldig geholpen in mijn onderzoek. Alhoewel veel van jullie werk niet in mijn proefschrift verschenen is (o.a. door de switch in onderwerp), heb ik van jullie veel geleerd over mijn project. My (former) roommates Laura Vogelaar, Jens Potreck, Bernke Papenburg en Sander Reijerkerk (La 1330) and Srivatsa Bettahalli and Can Aran (Me 314). Many thanks for all the good laughs and nice 1330-dinners we have had. And all the others...

Detlef Lohse. Through the intensive cooperation with the Physics of Fluids group, I have regained interest for the field of physics. Although our opinions did not always match, I have appreciated the discussions we had very much. Thank you for the opportunity to work together with your people and in your labs.

Christophe Pirat, Mauro Sbragaglia, Bram Borkent and Peichun Amy Tsai. I have really enjoyed working together with you all on the fluid dynamics research. My learning curve was steep in the years that we collaborated. Also thanks to the rest of the group for the occasional questions and occupation of the equipment.

Pap, mam en Kevin. Bedankt voor jullie eeuwige interesse in mijn rollende druppeltjes en "yoghurt experimenten". Het wetenschappelijk onderzoek is soms ondoorgrondelijk, maar jullie boden altijd een luisterend oor naast een goede kop thee.

Paul. Jij bent de meest stimulerende factor tijdens mijn studie en promotie geweest. Altijd was je er voor een gesprek op de fiets naar huis of als sparring partner voor (wetenschappelijke) discussies. Jij was en bent mijn voorbeeld, maar vooral een geweldige partner! Arigato.

And now it is time to explore the world...